

RICE UNIVERSITY

**Characterizing Water-in-Oil Emulsions with Application to  
Gas Hydrate Formation**

by

**Clint Philip Aichele**

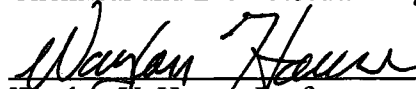
A THESIS SUBMITTED  
IN PARTIAL FULFILLMENT OF THE  
REQUIREMENTS FOR THE DEGREE

**Doctor of Philosophy**

APPROVED, THESIS COMMITTEE:



Walter G. Chapman, William W. Akers  
Professor, Chair  
Chemical and Biomolecular Engineering



Waylon V. House, Professor,  
Petroleum Engineering, Texas Tech



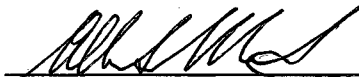
David W. Scott, Noah Harding Professor,  
Statistics



George J. Hirasaki, A.J. Hartsook Professor,  
Chemical and Biomolecular Engineering



Kenneth R. Cox, Professor,  
Chemical and Biomolecular Engineering



Alberto Montesi, Senior Research Scientist,  
Chevron ETC

HOUSTON, TEXAS  
MAY 2009

UMI Number: 3362123

### INFORMATION TO USERS

The quality of this reproduction is dependent upon the quality of the copy submitted. Broken or indistinct print, colored or poor quality illustrations and photographs, print bleed-through, substandard margins, and improper alignment can adversely affect reproduction.

In the unlikely event that the author did not send a complete manuscript and there are missing pages, these will be noted. Also, if unauthorized copyright material had to be removed, a note will indicate the deletion.



---

UMI Microform 3362123

Copyright 2009 by ProQuest LLC

All rights reserved. This microform edition is protected against unauthorized copying under Title 17, United States Code.

---

ProQuest LLC  
789 East Eisenhower Parkway  
P.O. Box 1346  
Ann Arbor, MI 48106-1346

# **ABSTRACT**

## **Characterizing Water-in-Oil Emulsions with Application to Gas Hydrate Formation**

by

**Clint P. Aichele**

This thesis implements nuclear magnetic resonance (NMR) techniques to directly measure water-in-oil emulsion properties and gas hydrate formation. This thesis introduces a novel application of the pulsed field gradient with diffusion editing (PFG-DE) NMR technique to measure drop size distributions of emulsions. The PFG-DE technique agrees with the standard pulsed field gradient (PFG) technique for a variety of emulsions. For the first time, this thesis utilizes the PFG-DE technique, coupled with the Carr-Purcell-Meiboom-Gill (CPMG) technique, to directly measure and quantify gas hydrate formation in emulsified systems. These unique data for black oil emulsions aid in developing effective flow assurance strategies.

To elucidate emulsion formation mechanisms in well defined shear fields, this thesis implements Taylor-Couette flow to form water-in-oil emulsions. A range of oil viscosities is considered by selecting two crude oils that differ in viscosity, and each crude oil is matched with a model oil of similar viscosity. For the low viscosity crude/model oil systems, the computational fluid dynamics (CFD) simulations show that the intensity of Taylor vortices increases at higher rotational speeds, and this leads to multimodal drop size distributions. For the high viscosity crude/model oil systems, the CFD simulations show that the flow field is simple shear for all rotational speeds. The high viscosity crude oil emulsions exhibited multimodality for all rotational speeds

investigated, while the corresponding model oil emulsions exhibited broad, smooth drop size distributions.

In contrast to Taylor-Couette flow, this thesis also examined emulsification in complex flow conditions with inhomogeneous shear using a six bladed Rushton turbine. This work supplies transient drop size distributions for two crude oils. This work provides emulsion formation and stability characteristics for both high and low mixing speeds, as well as comparisons to established models that predict emulsion drop size in turbulent flow.

Recent evidence suggests a relationship between water-in-oil emulsion morphology and gas hydrate blockage formation. An experimental setup to measure emulsion properties during gas hydrate formation was constructed, and the resulting NMR measurements indicate that for three of the four oils investigated, gas hydrate shells form around the water drops with thickness approximately equal to 1  $\mu\text{m}$ .

## ACKNOWLEDGMENTS

I thank God for the abundant blessings and opportunities He has given me.

I thank Chevron Corporation for full financial support of this project.

I thank my advisor, Dr. Walter Chapman, for facilitating this project and making it a reality. I have benefited from his optimism, flexibility, and encouragement throughout my thesis work.

I thank Dr. Waylon House for his generous donation of time and expertise toward this project. I enjoyed working with Waylon, and I am particularly thankful for his knowledge of NMR and all the ways he helped this project succeed.

I thank Dr. George Hirasaki for allowing me to use his NMR equipment, laboratory space, and for providing me with access to the NMR software. Without Dr. Hirasaki's gracious sharing of equipment and software, this project would not have been completed.

I thank Dick Chronister for helping me fabricate the cooling system, pressure vessel, and saturation pump. I enjoyed his stories and insights.

I thank Mark Flaum and Michael Rauschhuber for help with the NMR measurements and for enlightening discussions.

I thank Lee Rhyne and Hariprasad Subramani for their generous donation of time and resources toward this project. Their intensity and intellect continually inspire me.

I thank Alberto Montesi and Jeff Creek for initiating the project, helpful discussions, and supplying oil samples and properties.

I thank the committee members for taking time to participate in this project.

I thank Adam Bymaster for his friendship throughout this trial.

I thank my brother, Adam Aichele, for encouraging me and providing comic relief along the way.

I thank my parents, Doug and Kathryn Aichele, for their unconditional love, inspiration, and support.

Most importantly, I thank my soul mate, Melanie Aichele, for walking through this with me. For all the abundant love that she has selflessly provided, including, but not limited to, hot meals every night, flexibility, hospital care, and financial support.

Finally, thanks go to my son Sawyer, who reminds me each day of the many facets of life that are much more important than this thesis.

# TABLE OF CONTENTS

TITLE PAGE .....	i
ABSTRACT.....	ii
ACKNOWLEDGEMENTS .....	iv
TABLE OF CONTENTS .....	vi
LIST OF TABLES .....	ix
LIST OF FIGURES .....	xi
 Chapter 1: Introduction .....	 1
1.1 Motivation.....	1
1.2 Emulsions.....	2
1.3 Gas hydrates.....	7
1.4 Safety and Environment.....	9
1.5 Thesis contents.....	10
1.6 Notation.....	10
 Chapter 2: Nuclear Magnetic Resonance (NMR): Background and Techniques .....	 11
2.1 Introduction.....	11
2.2 Principles of NMR .....	11
2.3 Carr-Purcell-Meiboom-Gill (CPMG) Technique .....	15
2.4 Pulsed Field Gradient (PFG) Technique.....	18
2.5 Pulsed Field Gradient with Diffusion Editing (PFG-DE) Technique.....	22
2.6 Rapid Acquisition with Relaxation Enhancement (RARE).....	23
2.7 Conclusions.....	25
2.8 Notation.....	25
 Chapter 3: Water-in-Oil Emulsion Droplet Size Characterization Using a Pulsed Field Gradient with Diffusion Editing (PFG-DE) NMR Technique.....	 27
3.1 Introduction.....	27
3.2 Experimental Methods .....	28
3.2.1 Carr-Purcell-Meiboom-Gill (CPMG) .....	28
3.2.2 Pulsed Field Gradient (PFG) and Pulsed Field Gradient with Diffusion Editing (PFG-DE).....	29
3.2.3 Emulsion preparation .....	36
3.3 Results.....	37
3.3.1 Emulsified brine $T_2$ distribution overlaps the bulk brine $T_2$ distribution (experiment # 1, crude oil A).....	38
3.3.2 Emulsified brine $T_2$ distribution overlaps the bulk crude oil $T_2$ distribution (experiment # 2, crude oil B) .....	42
3.3.3 Bimodal drop size distribution (experiment # 3, crude oil A) .....	46
3.4 Conclusions.....	55
3.5 Notation.....	56
 Chapter 4: Analysis of Formation of Water-in-Oil Emulsions .....	 57

4.1 Introduction.....	57
4.2 Experimental methods .....	65
4.3 Computational methods .....	71
4.4 Results.....	72
4.4.1 Crude/model oil A systems.....	72
4.4.2 Crude oil C/model oil B systems .....	79
4.5 Conclusions.....	83
4.6 Notation.....	84
Chapter 5: Characterizing Water-in-Crude-Oil Emulsions Formed with a Rushton	
Turbine.....	85
5.1 Introduction.....	85
5.2 Experimental methods .....	87
5.2.1 Fluid properties .....	87
5.2.2 Emulsion preparation equipment .....	88
5.2.3 Applied shear equipment .....	89
5.2.4 NMR measurements.....	90
5.3 Results.....	92
5.3.1 Crude oil A: High mixing $Re$ with no applied shear after emulsification .....	92
5.3.2 Crude oil A: High mixing $Re$ with applied shear after emulsification .....	98
5.3.3 Crude oil A: Low mixing $Re$ with no applied shear after emulsification .....	101
5.3.4 Crude oil A: Low mixing $Re$ with applied shear after emulsification .....	103
5.3.5 Crude oil C: Low mixing $Re$ with no applied shear after emulsification .....	104
5.3.6 Crude oil C: Low mixing $Re$ with applied shear after emulsification .....	108
5.3.7 Effects of power and energy input .....	111
5.3.8 Comparison to published correlations .....	112
5.4 Conclusions.....	113
5.5 Notation.....	115
Chapter 6: Nuclear Magnetic Resonance Analysis of Gas Hydrate Formation in Water-in-	
Oil Emulsions.....	116
6.1 Introduction.....	116
6.2 Experimental methods .....	117
6.2.1 NMR techniques .....	117
6.2.2 Fluid properties .....	118
6.2.3 Sample preparation .....	118
6.3 Results and discussion .....	121
6.3.1 Water-in-crude-oil-A emulsion.....	121
6.3.2 Water-in-model-oil-A emulsion.....	131
6.3.3 Water-in-crude-oil-C emulsion.....	135
6.3.4 Water-in-model-oil-B emulsion.....	139
6.4 Conclusions.....	143
6.5 Notation.....	144
Chapter 7: Significant Contributions and Future Work.....	
7.1 Significant Contributions .....	145



7.2 Future Work .....	146
Appendix A: NMR Procedures .....	148
A.1 Centering the sample .....	148
A.2 Tuning .....	148
A.3 CPMG .....	149
A.4 PFG-DE .....	150
A.5 RARE .....	150
A.6 Hydrate measurements .....	151
References .....	152

## LIST OF TABLES

Table 3.1: Experimental NMR parameters. ....	36
Table 3.2: Density and viscosity information of the fluids used in this work. ....	37
Table 3.3: Summary of formation conditions and measurement durations for the three experiments. ....	37
Table 3.4: Summary of results for the unimodal brine-in-crude-oil emulsions. ....	46
Table 4.1: Effect of surfactant on model oil viscosity. Viscosity values are reported with units of cP. ....	66
Table 4.2: Densities of the fluids. ....	67
Table 5.1: Brine-in-crude-oil-A emulsions with 10 minutes of high mixing $Re$ and no applied shear after emulsification. ....	92
Table 5.2: Brine-in-crude-oil-A emulsions with 1 minute of high mixing $Re$ and no applied shear after emulsification. ....	95
Table 5.3: Brine-in-crude-oil-A with 10 minutes of high mixing $Re$ and applied shear after emulsification. ....	98
Table 5.4: Brine-in-crude-oil-A emulsions with 1 minute of high mixing $Re$ and applied shear after emulsification. ....	99
Table 5.5: Brine-in-crude-oil-A with 10 minutes of low mixing $Re$ and no applied shear after emulsification. ....	102
Table 5.6: Brine-in-crude-oil-A with 10 minutes of low mixing $Re$ and applied shear after emulsification. ....	103
Table 5.7: Brine-in-crude-oil-C mixing conditions with 10 minutes of low mixing $Re$ and no applied shear after emulsification. ....	105
Table 5.8: Brine-in-crude-oil-C mixing conditions with 1 minute of low mixing $Re$ and no applied shear after emulsification. ....	106
Table 5.9: Brine-in-crude-oil-C mixing conditions with the application of mild shear after 10 minutes of low mixing $Re$ . ....	108
Table 5.10: Brine-in-crude-oil-C mixing conditions with 1 minute of low mixing $Re$ and applied shear after emulsification. ....	109

Table 6.1: Experimental parameters used for the PFG-DE measurements. ....	121
Table 6.2: Comparison of experimental and predicted mean diameters for the water-in crude-oil-A emulsion. ....	130
Table 6.3: Comparison of experimental and predicted mean diameters for the water-in model-oil-A emulsion. ....	134
Table 6.4: Comparison of experimental and predicted mean diameters for the water-in crude-oil-C emulsion. In the warming cycle, the drop size distribution could not be measured due to the high noise level of the measurement.....	139
Table 6.5: Comparison of experimental and predicted mean diameters for the water-in model-oil-B emulsion. ....	143

# LIST OF FIGURES

Figure 1.1: Four common types of emulsions. Black indicates oil and blue indicates water (adapted from Schramm). <sup>1</sup>	3
Figure 1.2: Common destabilization mechanisms of water-in-oil emulsions. <sup>19</sup>	4
Figure 1.3: Illustration of surfactants at oil-water interfaces. <sup>22</sup>	5
Figure 1.4: Illustration of the Marangoni effect. <sup>8, 24</sup>	6
Figure 2.1: Illustration of spinning nuclei in the absence and presence of an external magnetic field, $B_o$ . Note that the nuclei precess around the direction of $B_o$ .	12
Figure 2.2: The CPMG pulse sequence. As time progresses, the magnetization vector in the transverse plane decays according to the transverse relaxation time ( $T_2$ ) (adapted from Peña 2006). <sup>4</sup>	15
Figure 2.3: Example of a $T_2$ distribution of a water-in-oil emulsion. Note that the oil and water are separated according to their $T_2$ distributions.	16
Figure 2.4: Pulsed field gradient (PFG) pulse sequence with stimulated echoes and pre-gradient pulses. The amplitudes of the first 10 echoes are fit by linear regression to obtain the amplitude of the first echo.	19
Figure 2.5: Pulsed field gradient with diffusion editing (PFG-DE) pulse sequence.	22
Figure 2.6: Example of the two dimensional result obtained from the PFG-DE technique.	23
Figure 2.7: Pulse sequence for the RARE technique (from Rauschhuber, 2007). <sup>65</sup>	24
Figure 2.8: Example of a typical vertical image of an emulsion produced by the RARE technique. Note the distinction between oil and water in the sample.	24
Figure 3.1: Example of parameters calculated for PFG-DE and PFG measurements. These parameters were calculated with ( $\rho = 1.0 \mu\text{m/s}$ , $D_{DP} = 2.6 \times 10^{-9} \text{m}^2/\text{s}$ , $T_{2,bulk} = 2.5 \text{ s}$ , and $\Delta/T_{2,DP} = 0.3$ ).	31
Figure 3.2: Attenuation of 60 drop sizes using one parameter set ( $\Delta = 244 \text{ ms}$ , $\delta = 49 \text{ ms}$ , $g = 2 - 47 \text{ G/cm}$ ).	33
Figure 3.3: Sensitivity of five parameter sets.	34
Figure 3.4: Drop size masks for each parameter set.	35

Figure 3.5: $T_2$ masking for five parameter sets.....	36
Figure 3.6: $T_2$ distribution of an emulsion with $\omega = 1600$ rpm for 10 minutes. Note the proximity of the emulsified brine $T_2$ distribution to the bulk brine $T_2$ distribution. .	38
Figure 3.7: Drop size distribution obtained from transverse relaxation data. Note the increase in the width of the distribution that was caused by the approach of the emulsified brine $T_2$ distribution to the bulk brine $T_2$ distribution. ....	39
Figure 3.8: Two dimensional map produced from the PFG-DE technique after application of the mask. Note the separation of the crude oil A and brine in terms of transverse relaxation. Only brine contributes to the drop size distribution.....	40
Figure 3.9: Comparison of drop size distributions obtained from the PFG-DE and PFG techniques. The drop size distribution from the PFG-DE technique given by the mean and one standard deviation on either side of the mean (45, 59, 72) $\mu\text{m}$ agrees well with the traditional PFG technique, (47, 58, 72) $\mu\text{m}$ . ....	41
Figure 3.10: Overlap of emulsion and crude oil B $T_2$ distributions.....	43
Figure 3.11: Two dimensional map of brine-in-crude-oil-B emulsion after masking. The emulsified brine and crude oil B $T_2$ distributions overlap, but the crude oil B does not contribute to the drop size distribution because the crude oil B signal attenuated significantly.....	44
Figure 3.12: Experimental and predicted attenuation for the Experiment # 2 brine-in-crude-oil-B emulsion ( $\Delta = 552$ ms, $\delta = 28$ ms, and $g = 1 - 13$ G/cm). Note that the crude oil B does not contribute to the attenuation of the signal of the emulsion, thereby facilitating the separation of the crude oil B and brine contributions.....	45
Figure 3.13: Comparison of drop size distributions obtained from the PFG-DE and PFG techniques. The drop size distribution from the PFG-DE technique, (14, 19, 24) $\mu\text{m}$ , agrees well with the traditional PFG technique (14, 21, 31) $\mu\text{m}$ . ....	46
Figure 3.14: Comparison of drop size distributions with $\omega = 2875$ rpm. The PFG-DE technique yielded a drop size distribution, (10, 15, 20) $\mu\text{m}$ , that agreed with the PFG technique, (11, 15, 19) $\mu\text{m}$ . ....	48
Figure 3.15: Comparison of drop size distributions with $\omega = 1600$ rpm. The PFG-DE technique yielded a drop size distribution, (42, 60, 78) $\mu\text{m}$ , that agreed with the PFG technique, (50, 66, 87) $\mu\text{m}$ . ....	49
Figure 3.16: Sensitivity of the two parameter sets with the noise cutoff equal to 0.02....	50
Figure 3.17: Drop size masks for each parameter set. ....	50

Figure 3.18: Two dimensional results for the first parameter set. The most sensitive drop size is indicated by the solid line while the limits of the sensitivity of the measurement are indicated by the dashed lines. Note that the population of smaller drops exists in the sensitive region. ....	51
Figure 3.19: Two dimensional results for the second parameter set. Note that the larger population of drop sizes is present in the sensitive region.....	52
Figure 3.20: Transverse relaxation masks for the two parameter sets. ....	53
Figure 3.21: Two dimensional map of the bimodal drop size distribution after masking both drop size and transverse relaxation. The brine contribution to the drop size distribution was isolated according to the separation of the $T_2$ distributions. ....	54
Figure 3.22: Comparison of unimodal drop size distributions with the bimodal drop size distribution obtained using the PFG-DE technique. ....	55
Figure 4.1: A drop existing in simple shear flow between two parallel plates (Guido and Villone 1998). <sup>71</sup> .....	58
Figure 4.2: Experimental results for the drop deformation of a single drop undergoing simple shear. The experimental results match the theory proposed by Taylor at low Capillary numbers (Guido and Villone 1998). <sup>71</sup> .....	60
Figure 4.3: Comparison of experimental data to Taylor's deformation theory. The three axes, $a$ , $b$ , and $c$ , are normalized with respect to the initial drop diameter (Guido and Villone 1997). <sup>71</sup> .....	61
Figure 4.4: Dependence of critical Capillary number on viscosity ratio (Grace 1982). <sup>78</sup>	61
Figure 4.5: Critical Capillary number as a function of viscosity ratio for simple shear flow. The hatched lines are experimental results from Grace. <sup>78</sup> The solid line is asymptotic theory for $\lambda$ going to zero by Hinch and Acrivos. <sup>79</sup> The open circles are theoretical predictions from Barthes-Biesel and Acrivos <sup>80</sup> (Rallison 1984). <sup>68</sup> .....	62
Figure 4.6: General drop breakup mechanisms that occur as a function of Capillary number and viscosity ratio (reproduced from Zhao 2007). <sup>70</sup> .....	64
Figure 4.7: Viscosity as a function of temperature for the crude and model oils. ....	66
Figure 4.8: SARA analysis for the 4 oils used in this work (provided by Dr. Jill Buckley's laboratory at New Mexico Tech, 2008). <sup>82</sup> .....	67
Figure 4.9: Equilibrium interfacial tension of the two crude oils. ....	68

Figure 4.10: Equilibrium interfacial tension of the two model oils in the presence of surfactant.....	69
Figure 4.11: Taylor-Couette flow leads to the development of secondary flow patterns referred to as Taylor vortices. <sup>84</sup> .....	70
Figure 4.12: Comparison of axial velocities for a multi-phase simulation and single phase simulation (max. velocity = 0.43 m/s). .....	72
Figure 4.13: Swirl and axial velocity profiles for the crude/model oil A systems ( $\mu_{eff} = 36$ cP, $\omega = 1600$ rpm).....	73
Figure 4.14: Swirl and axial velocity profiles for the crude/model oil A systems ( $\mu_{eff} = 36$ cP, $\omega = 3000$ rpm).....	73
Figure 4.15: Drop size distributions of the brine-in-crude-oil-A emulsions. Note the increase in multimodality with increasing inner cylinder rotational speed. ....	74
Figure 4.16: Optical microscopy of brine-in-crude-oil-A emulsion at 3000 rpm (objective = 20X). .....	75
Figure 4.17: Drop size distributions of the brine-in-model-oil-A emulsions. ....	75
Figure 4.18: Comparison between model predictions and experimental data for the brine-in-crude-oil-A emulsions. ....	77
Figure 4.19: Comparison between model predictions and experimental data for the brine-in-model-oil-A emulsions. ....	78
Figure 4.20: Swirl and axial velocity profiles for the crude oil C/model oil B systems ( $\mu_{eff} = 400$ cP, $\omega = 1600$ rpm). ....	79
Figure 4.21: Drop size distributions for brine-in-crude-oil-C emulsions. ....	80
Figure 4.22: Optical microscopy of the brine-in-crude-oil-C emulsion at 1300 rpm (objective = 20X). ....	80
Figure 4.23: Drop size distributions for brine-in-model-oil-B emulsions. ....	81
Figure 4.24: Comparison of experimental data to the Grace and Janssen models for the brine-in-crude-oil-C emulsions.....	82
Figure 4.25: Comparison of experimental data to the Grace and Janssen models for the brine-in-model-oil-B emulsions.....	82
Figure 5.1: $T_2$ distributions of pure crude oil A, crude oil C, and brine at 303.2 K. ....	88

Figure 5.2: Impeller and shaft. ....	89
Figure 5.3: Position of the impeller. ....	89
Figure 5.4: Bench top roller used to apply shear after emulsification. ....	90
Figure 5.5: PFG-DE measurement used to determine the surface relaxivity for the brine-in-crude-oil-A system. ....	92
Figure 5.6: Brine-crude-oil-A Sauter diameters with 10 minutes of high mixing $Re$ and no applied shear after emulsification. ....	94
Figure 5.7: Brine-in-crude-oil-A drop size distributions with 10 minutes of high mixing $Re$ and no applied shear after emulsification. ....	95
Figure 5.8: Brine-in-crude-oil-A Sauter diameters with 1 minute of high mixing $Re$ and no applied shear after emulsification. ....	96
Figure 5.9: Brine-in-crude-oil-A drop size distributions with 1 minute of high mixing $Re$ and no applied shear after emulsification. ....	96
Figure 5.10: Brine-in-crude-oil-A transient $T_2$ distributions with 1 minute of high mixing $Re$ and no applied shear after emulsification. ....	97
Figure 5.11: Brine-in-crude-oil-A Sauter diameters with 10 minutes of high mixing $Re$ and applied shear after emulsification. ....	98
Figure 5.12: Brine-in-crude-oil-A drop size distributions with 10 minutes of high mixing $Re$ and applied shear after emulsification. ....	99
Figure 5.13: Brine-in-crude-oil-A Sauter diameters with 1 minute of high mixing $Re$ and applied shear after emulsification. ....	100
Figure 5.14: Brine-in-crude-oil-A drop size distributions with 1 minute of high mixing $Re$ and applied shear after emulsification. ....	101
Figure 5.15: Brine-in-crude-oil-A transient $T_2$ distributions with 10 minutes of low mixing $Re$ and no applied shear after emulsification. ....	102
Figure 5.16: Brine-in-crude-oil-A emulsion 24 hours after emulsion formation with 10 minutes of low mixing $Re$ and no applied shear after emulsification. ....	103
Figure 5.17: Brine-in-crude-oil-A $T_2$ distributions with 10 minutes of low mixing $Re$ and applied shear after emulsification. ....	104



Figure 5.18: Brine-in-crude-oil-A emulsion 24 hours after formation with 10 minutes of low mixing $Re$ and applied shear after emulsion formation. ....	104
Figure 5.19: Brine-in-crude-oil-C Sauter diameters with 10 minutes of low mixing $Re$ and no applied shear after emulsification. ....	105
Figure 5.20: Brine-in-crude-oil-C drop size distributions with 10 minutes of low mixing $Re$ and no applied shear after emulsification. ....	106
Figure 5.21: Brine-in-crude-oil-C Sauter diameters with 1 minute of low mixing $Re$ and no applied shear after emulsification. ....	107
Figure 5.22: Brine-in-crude-oil-C drop size distributions with 1 minute of low mixing $Re$ and no applied shear after emulsification. ....	107
Figure 5.23: Brine-in-crude-oil-C Sauter diameters with 10 minutes of low mixing $Re$ and applied shear after emulsification. ....	108
Figure 5.24: Brine-in-crude-oil-C drop size distributions with 10 minutes of low mixing $Re$ and applied shear after emulsification. ....	109
Figure 5.25: Brine-in-crude-oil-C Sauter diameters with 1 minute of low mixing $Re$ and applied shear after emulsification. ....	110
Figure 5.26: Brine-in-crude-oil-C drop size distributions with 1 minute of low mixing $Re$ and applied shear after emulsification. ....	110
Figure 5.27: Average Sauter diameter as a function of power input. ....	111
Figure 5.28: Average Sauter diameter as a function of energy input. ....	111
Figure 5.29: Comparison of experimental Sauter mean diameters for the crude oil A emulsions with correlations by Chen and Middleman, <sup>96</sup> Wang, <sup>94</sup> and Calabrese. <sup>93</sup>	112
Figure 5.30: Comparison of mean drop sizes for brine-in-crude-oil-A emulsions formed with the Rushton turbine and Taylor-Couette flow. ....	113
Figure 6.1: Schematic of the experimental setup (not drawn to scale). ....	119
Figure 6.2: Deviation of temperature in the pressure vessel. ....	120
Figure 6.3: Temperature of the water-in-crude-oil-A emulsion. ....	122
Figure 6.4: Comparison of $T_2$ distributions of water-in-crude-oil-A emulsion during the cooling and warming stages. Note the decreased amplitude of the water distribution during the warming stage which indicates the presence of methane hydrate. ....	122

Figure 6.5: Liquid water fraction as a function of temperature for the water-in-crude-oil-A emulsion. ....	123
Figure 6.6: Control experiment without methane for a water-in-crude-oil-A emulsion. ....	124
Figure 6.7: Vertical (one-dimensional) distribution of components in the pressure vessel for the water-in-crude-oil-A emulsion before hydrate formation (277.2 K, 6.2 MPa). ....	125
Figure 6.8: Vertical (one-dimensional) distribution of components in the pressure vessel for the water-in-crude-oil-A emulsion during hydrate formation (277.3 K, 6.2 MPa). Note the decrease in intensity of the water signal, thereby indicating the presence of methane hydrate. ....	126
Figure 6.9: Illustration of the threshold model. The cooling curve is a lognormal distribution with mean diameter equal to 10 $\mu\text{m}$ . The warming curve is generated by assuming that 45% of the liquid water volume, starting with the largest drops, completely converts to hydrate. Note that the cooling and warming curves are identical at the lower end of the distribution. ....	127
Figure 6.10: Illustration of the shell model. The cooling curve is a lognormal distribution with mean diameter equal to 10 $\mu\text{m}$ . The warming curve is generated by assuming that a constant thickness hydrate shell forms on the drops to yield 45% hydrate conversion. ....	128
Figure 6.11: Comparison of the threshold and shell models to the drop size distributions of the water-in-crude-oil-A emulsion. ....	129
Figure 6.12: Sample temperature of the water-in-model-oil-A emulsion. ....	131
Figure 6.13: Liquid water fraction as a function of temperature for the water-in-model-oil-A emulsion. ....	132
Figure 6.14: Vertical (one-dimensional) distribution of components in the pressure vessel for the water-in-model-oil-A emulsion before hydrate formation (276.5 K, 6.2 MPa). ....	133
Figure 6.15: Vertical (one-dimensional) distribution of components in the pressure vessel for the water-in-model-oil-A emulsion during hydrate formation (277.0 K, 6.2 MPa). ....	133
Figure 6.16: Comparison of the threshold and shell models to the drop size distributions of the water-in-model-oil-A emulsion. ....	134
Figure 6.17: Sample temperature of the water-in-crude-oil-C emulsion. ....	135

Figure 6.18: Liquid water fraction as a function of temperature for the water-in-crude-oil-C emulsion. ....	136
Figure 6.19: Comparison of $T_2$ distributions during the cooling and warming stages. ..	137
Figure 6.20: Vertical (one-dimensional) distribution of components in the pressure vessel for the water-in-crude-oil-C emulsion before hydrate formation (277.0 K, 6.2 MPa). ....	137
Figure 6.21: Vertical (one-dimensional) distribution of components in the pressure vessel for the water-in-crude-oil-C emulsion during the warming stage (277.0 K, 6.2 MPa). ....	138
Figure 6.22: Comparison of the threshold and shell models to the drop size distributions of the water-in-crude-oil-C emulsion.....	139
Figure 6.23: Sample temperature for the water-in-model-oil-B emulsion. ....	140
Figure 6.24: Liquid water fraction as a function of temperature for the water-in-model-oil-B emulsion.....	141
Figure 6.25: Vertical (one-dimensional) distribution of components in the pressure vessel for the water-in-model-oil-B emulsion before hydrate formation (275.8 K, 6.2 MPa). ....	141
Figure 6.26: Vertical (one-dimensional) distribution of components in the pressure vessel for the water-in-model-oil-B emulsion during the warming stage (277.0 K, 6.2 MPa).....	142
Figure 6.27: Comparison of the threshold and shell models to the drop size distributions of the water-in-model-oil-B emulsion. ....	143

## **Chapter 1: Introduction**

An emulsion is a dispersion of two immiscible liquids.<sup>1</sup> Emulsions exist in many industrial sectors including the food,<sup>2</sup> pharmaceutical,<sup>3</sup> and energy industries.<sup>4-6</sup> This thesis focuses on emulsions related to the energy industry, though the generality of emulsion concepts makes the insight gained herein transferable to other applications. This thesis presents experimental and computational insight regarding emulsion formation mechanisms and gas hydrate formation phenomena in water-in-oil emulsions. This insight aids in the development of flow assurance strategies for combating problems related to emulsions and gas hydrates. This chapter introduces the motivation for the work presented in this thesis, provides background information about emulsions and gas hydrates, and outlines the contents of this thesis.

### **1.1 Motivation**

The motivation for the work contained in this thesis is twofold: (1) emulsions and (2) gas hydrate formation in emulsions. Emulsions exist in nearly every aspect of operations in the energy industry, especially during the production of crude oil.<sup>5</sup> Emulsions promote several problems in the energy industry including problems in separations and flow assurance.<sup>7</sup> The formation of concentrated emulsions, particularly crude oil emulsions, in the presence of surfactants is a complex process with several competing mechanisms.<sup>8</sup> To effectively manage emulsions in industrial settings, it is imperative to predict and have the ability to manipulate the emulsion drop size distribution.

As offshore drilling and production operations move into deeper waters, low temperatures and high pressures found in these environments predispose these systems to gas hydrate blockage formation.<sup>9</sup> The energy industry currently spends millions of dollars each year combating the formation of gas hydrate blockages during the production of crude oil and natural gas.<sup>9,10</sup> The current strategy to prevent blockages involves the addition of costly chemicals to production systems.<sup>10</sup> Recent evidence suggests the possibility of using water-in-oil emulsions as an inhibition strategy for gas hydrate blockage formation, thereby reducing operating costs.<sup>7,11-13</sup> To provide insight about this possibility, this thesis employs nuclear magnetic resonance (NMR) to investigate the formation and stability of water-in-oil emulsions with specific application to gas hydrate formation in emulsified systems

## **1.2 Emulsions**

Emulsions are dispersions of one liquid phase, referred to as the dispersed phase, in another, immiscible liquid phase, referred to as the continuous phase. According to Bancroft's rule, the continuous phase is the phase in which the surfactant is most soluble.<sup>14</sup> In addition, Ostwald showed that volume fraction also contributes to emulsion type.<sup>15</sup> If the phase fraction,  $\phi$ , of either phase is in the range,  $0.26 \leq \phi \leq 0.74$ , both water-in-oil and oil-in-water emulsions are possible. The maximum packing fraction for a face centered cubic lattice is 0.74, so exceeding this fraction will likely cause the emulsion to invert.

Emulsions typically consist of a polar liquid phase and a non-polar liquid phase.<sup>15-18</sup> The arrangement of each respective phase determines the classification of the emulsion. Figure 1.1 illustrates four types of emulsions.

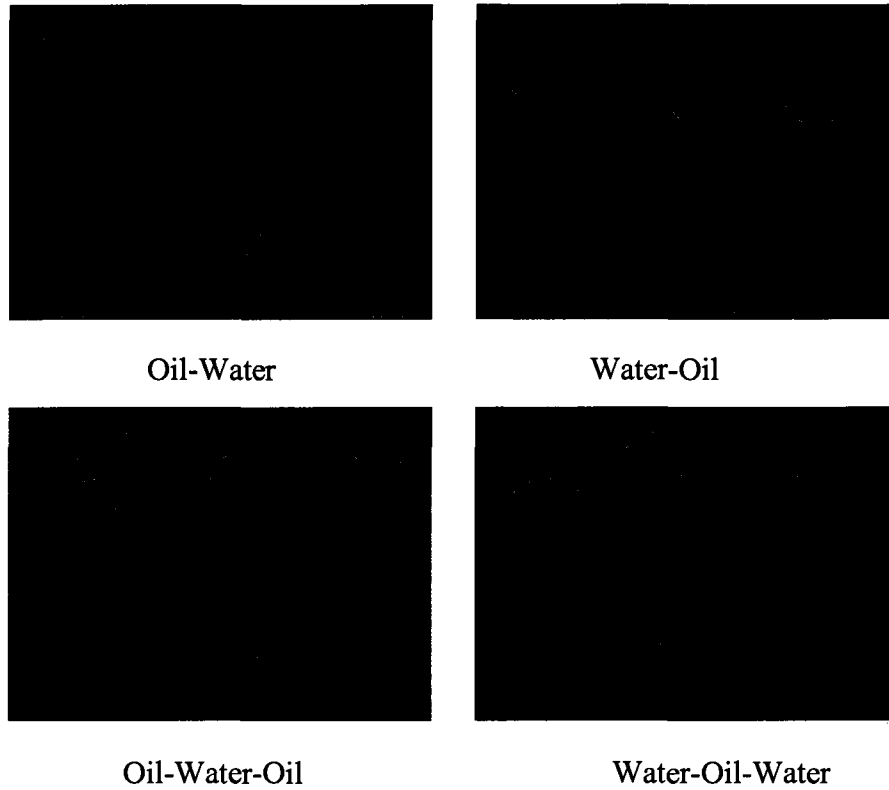


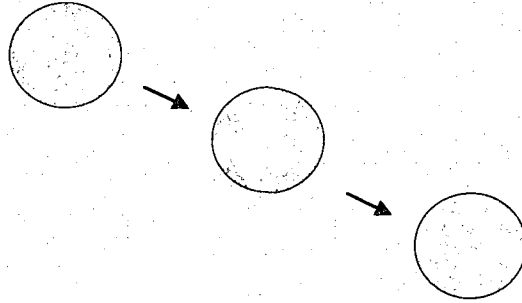
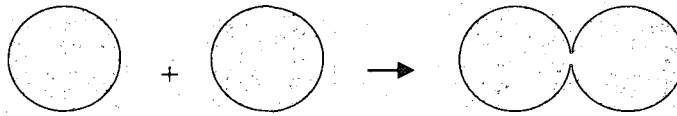
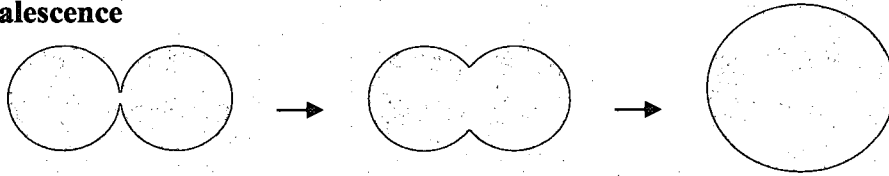
**Figure 1.1:** Four common types of emulsions. Black indicates oil and blue indicates water (adapted from Schramm).<sup>1</sup>

This thesis exclusively focuses on water-in-oil emulsions.

Emulsions are thermodynamically unstable because the free energy of the system is not minimized due to the large amount of interfacial area that is created in an emulsion.<sup>1</sup>

$$dG = dA \sigma \quad (1.1)$$

Equation 1.1 shows that as the interfacial free energy,  $dA \sigma$ , increases, the Gibbs free energy,  $dG$ , also increases. Thermodynamically, the two immiscible phases prefer to be completely separated because two phase separation results in the minimization of the free energy of the system.<sup>1</sup> Figure 1.2 shows three common destabilization mechanisms of water-in-oil emulsions.

**Sedimentation****Flocculation****Coalescence**

**Figure 1.2:** Common destabilization mechanisms of water-in-oil emulsions.<sup>19</sup>

Sedimentation arises because of density differences between the two phases, and creaming is its analog for oil-in-water emulsions. Flocculation occurs as a result of attractions between the dispersed phase drops, and it can promote coalescence of drops in an emulsion. Coalescence occurs when the liquid film separating the two phases ruptures.<sup>19, 20</sup>

Emulsification leads to the development of additional interface. To create more interface, energy is required to overcome the LaPlace pressure.<sup>5</sup>

$$\Delta P_L = \sigma \left( \frac{1}{r_1} + \frac{1}{r_2} \right) = \sigma \frac{2}{r} \quad (1.2)$$

The LaPlace pressure,  $\Delta P_L$ , opposes external forces acting on the dispersed phase drops.

Mathematically, the interfacial tension can be understood according to the following expression.<sup>1</sup>

$$\sigma = \left( \frac{dG}{dA} \right)_{T,P} \Rightarrow \frac{\text{energy}}{\text{interfacial area}} \quad (1.3)$$

Interfacial tension describes the energy required to make additional interfacial area, and it arises because of an imbalance of intermolecular forces at the interface.<sup>1</sup> In other words, the interfacial tension is the cohesive force applied over the circumference of the drop.<sup>1</sup>

Surfactants combat the inherent instability of emulsions.<sup>19, 21</sup> The name itself indicates the function of surfactants, “surface active agents.” The main function of surfactants is to adsorb at the interface that separates the two immiscible phases, thus imparting kinetic stability to the emulsion.<sup>19</sup>

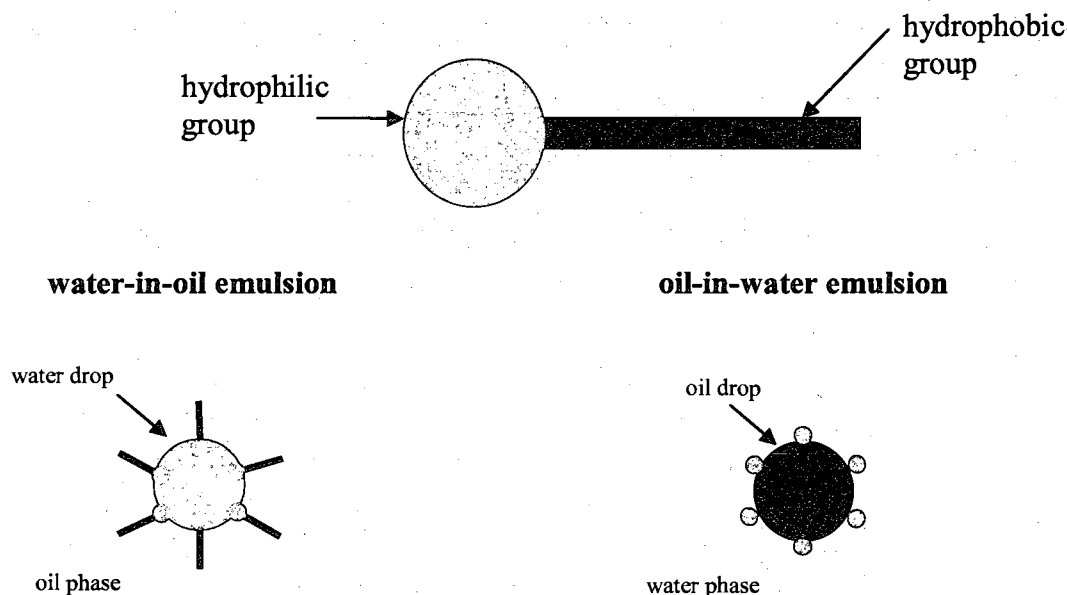


**Figure 1.3:** Illustration of surfactants at oil-water interfaces.<sup>22</sup>



A typical surfactant consists of a hydrophilic head group and a hydrophobic tail group. Therefore, this amphiphilic molecule can adsorb in both polar and non-polar phases. Surfactants impart emulsion stability in a variety of ways including steric effects<sup>1</sup> and enhancement of viscoelastic properties.<sup>23</sup>

Surfactants reduce the interfacial tension,  $\sigma$ , between the water and oil phases, as well as promote interfacial tension gradients. Interfacial tension gradients facilitate the Marangoni effect which has been shown to greatly enhance emulsion stability.<sup>8, 24, 25</sup>

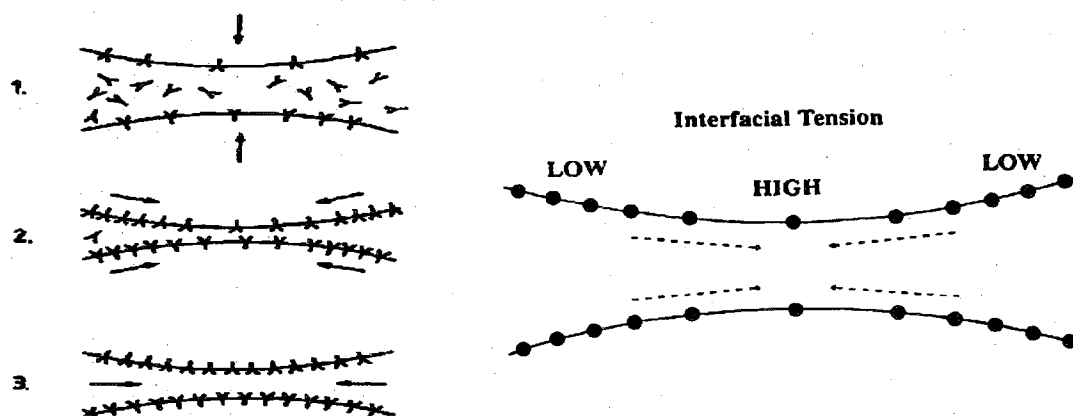


Figure 1.4: Illustration of the Marangoni effect.<sup>8, 24</sup>

As two drops come together, surfactants preferentially adsorb along the exterior regions of the approaching drops, thereby reducing the interfacial tension along the exterior. The interface flows from regions of low interfacial tension along the exterior of the drops to regions of high interfacial tension along the interior of the drops thereby providing stability.

Surfactants promote viscoelastic behavior at the interface.<sup>24</sup> The visco-elasticity of the interface is represented by the interfacial dilatational modulus.<sup>23</sup>

$$\epsilon = \frac{d\sigma}{d \ln(A)} \quad (1.4)$$

The change in interfacial tension that arises from a small change in area of the drop can be written as a function of both elastic and viscous contributions.<sup>23</sup>

$$\Delta\sigma = \text{elastic} + \text{viscous} = \varepsilon_d \Delta \ln a + \mu_d \frac{d \ln A}{dt} \quad (1.5)$$

Both contributions are determined by making sinusoidal oscillations of the interfacial area and measuring the resulting interfacial tension fluctuations.

This thesis focuses on crude oil emulsions. This type of emulsion commonly occurs when crude oil is produced in the presence of water, usually in the form of brine. As the two phases travel through production equipment such as chokes, pumps, and valves, water-in-crude-oil emulsions form.<sup>5, 6, 26</sup> The naturally occurring substances in the crude oil such as asphaltenes, resins, and naphthenic acids, along with other chemical species, impart stability to the water-in-crude-oil emulsions as a result of their interfacial properties.<sup>27-30</sup> Petroleum emulsions present significant challenges because crude oil consists of many components which affect both the formation and stabilization of the emulsions.

### **1.3 Gas hydrates**

Gas hydrates are clathrate structures held together by a hydrogen bonded network that forms when nonpolar gas molecules, such as methane, come into contact with polar water molecules at high pressures and low temperatures.<sup>10</sup> Gas hydrates are increasingly becoming popular on two fronts. First, gas hydrates can potentially serve as a future energy source.<sup>10</sup> Second, gas hydrates can form blockages in production piping thereby limiting overall production of crude oil and gas.<sup>10</sup> This thesis addresses the second topic, namely the formation of gas hydrates in water-in-oil emulsions.

Three clathrate hydrate crystal structures have been observed in nature. These classes are structure I,<sup>31</sup> structure II,<sup>32</sup> and structure H.<sup>33</sup> The size of the guest molecule determines the class. For structure I, the guest molecule is between 4.2 and 6 Angstroms.<sup>10</sup> This class includes such guest molecules as methane, carbon dioxide, and ethane. This thesis focuses on structure I hydrates, namely methane hydrates, which is the primary component in natural gas. Structure II consists of both small and large guests including nitrogen, hydrogen, and propane. Finally, structure H consists of large molecules (~8 Angstroms) in the presence of smaller molecules such as methane.

In 1934, Hammerschmidt unveiled the occurrence of gas hydrates in the oil and gas industry.<sup>34</sup> Since that time, significant research has been performed to understand hydrate formation in production equipment during oil and gas production. The primary motivation for this research has been the steep cost associated with both hydrate prevention and plug remediation.<sup>10, 35</sup>

Traditionally, the energy industry used thermodynamic inhibitors, such as methanol, to manage gas hydrate blockages.<sup>36</sup> Thermodynamic inhibitors shift the hydrate equilibrium conditions toward higher pressures and lower temperatures by disrupting the hydrogen bonded network. Though the use of thermodynamic inhibitors is well documented, they typically must be added at high concentrations,<sup>9</sup> thereby resulting in significant capital and operating costs.

In an attempt to reduce these costs, the industry developed low dosage hydrate inhibitors (LDHI), namely kinetic hydrate inhibitors (KHI) and anti-agglomerates (AA).<sup>10, 35</sup> Both kinetic inhibitors and anti-agglomerates do not shift the thermodynamic conditions for gas hydrate formation. Rather, kinetic inhibitors delay the nucleation and

growth of hydrate. Unfortunately, kinetic hydrate inhibitors are limited by the amount of subcooling, and they begin to fail with 20°F subcooling.<sup>37</sup> Anti-agglomerates are polymeric surfactants that adsorb to the surface of hydrate particles. They do not prevent the formation of hydrate; rather, they maintain the hydrate particles dispersed as a slurry, thus preventing the formation of a hydrate plug.

Despite the successful development of low dosage hydrate inhibitors, the energy industry prefers to avoid adding chemicals to production fluids because of the related cost and separation issues. Recent evidence suggests that stable water-in-oil emulsions can promote the successful transport of hydrate slurries in water-in-oil emulsions.<sup>7, 11-13</sup> This particular method requires no addition of chemicals. Therefore, knowledge about the relationship between water-in-oil emulsions and gas hydrate formation provides insight about this prevention strategy.

Direct measurements of hydrate formation in crude oil emulsions are rare because crude oil inhibits the use of standard optical techniques.<sup>37</sup> Recently, Gao directly measured gas hydrate formation in water-in-oil emulsions using NMR.<sup>38</sup> However, the relationship between emulsion drop size distribution and gas hydrate formation is not well understood.<sup>35</sup> Therefore, this work incorporates NMR to investigate gas hydrate formation in water-in-oil emulsions because NMR has the ability to directly measure both gas hydrate formation<sup>38,39</sup> and drop size distributions of emulsions.<sup>40</sup>

## ***1.4 Safety and Environment***

This thesis required working with crude and model oils as well as solvents such as toluene and acetone. To avoid exposure to these substances, nitrile gloves were worn at all times when working with the oils and solvents. Safety goggles were worn at all times

when working in the laboratory. The crude and model oils were stored in a ventilated storage closet. All samples were stored in a ventilated fume hood when not in use. All fluids were disposed in marked, ventilated containers in the fume hood.

## **1.5 Thesis contents**

Chapter 2 describes the fundamental concepts of nuclear magnetic resonance (NMR) and discusses the NMR techniques used in this thesis. Chapter 3 illustrates the ability of NMR to measure drop size distributions of water-in-oil emulsions. Chapter 4 focuses on the characterization of emulsion formation mechanisms in well defined shear fields using Taylor-Couette flow. Chapter 5 presents data regarding emulsion formation and stability in non-uniform shear fields using a Rushton turbine. Chapter 6 presents an investigation of the effects of gas hydrate formation on emulsion drop size distributions in water-in-oil emulsions. Finally, Chapter 7 contains the significant contributions and future work.

## **1.6 Notation**

$A$	interfacial area ( $\text{m}^2$ )
$G$	Gibbs free energy ( $\text{J}/\text{m}^2$ )
$P_L$	LaPlace pressure ( $\text{N}/\text{m}^2$ )
$r_1, r_2$	radii of curvature (m)
$\varepsilon$	interfacial dilatational modulus ( $\text{mN}/\text{m}$ )
$\varepsilon_d$	elastic contribution ( $\text{mN}/\text{m}$ )
$\mu_d$	viscous contribution ( $\text{mN}/\text{m}$ )
$\sigma$	interfacial tension ( $\text{mN}/\text{m}$ )

## **Chapter 2: Nuclear Magnetic Resonance (NMR): Background and Techniques**

### ***2.1 Introduction***

Nuclear magnetic resonance (NMR) measures physical properties of emulsions, rock samples, and biological systems.<sup>41, 42</sup> Because NMR does not rely on optical properties of the samples, the drop size distributions of crude oil emulsions can be directly measured using NMR. In addition, NMR directly measures gas hydrate formation.<sup>38, 39</sup> NMR measurements are non-invasive and non-destructive, and samples can be measured multiple times over long periods of time.<sup>41</sup> This thesis incorporates multiple NMR techniques to quantify the properties of water-in-oil emulsions. The Carr Purcell Meiboom Gill (CPMG)<sup>43, 44</sup> technique directly measures transverse relaxation, drop size distributions, and methane hydrate formation in emulsified systems. Drop size distributions are also measured using the pulse field gradient (PFG)<sup>45</sup> and pulse field gradient with diffusion editing (PFG-DE)<sup>46-48</sup> techniques. One dimensional imaging information is obtained using the rapid acquisition with relaxation enhancement (RARE)<sup>49</sup> technique.

### ***2.2 Principles of NMR***

The principles of NMR hinge on the fact that magnetic nuclei have an intrinsic angular momentum referred to as spin.<sup>50</sup> Based on magnetism, the spinning nucleus produces a magnetic field. Coates et al. state the following, “Nuclear Magnetic Resonance (NMR) refers to the response of atomic nuclei to magnetic fields.”<sup>51</sup> When a

magnetic field is applied to a spinning nucleus, the magnetic moment of the nucleus responds by precessing around the direction of the applied magnetic field.

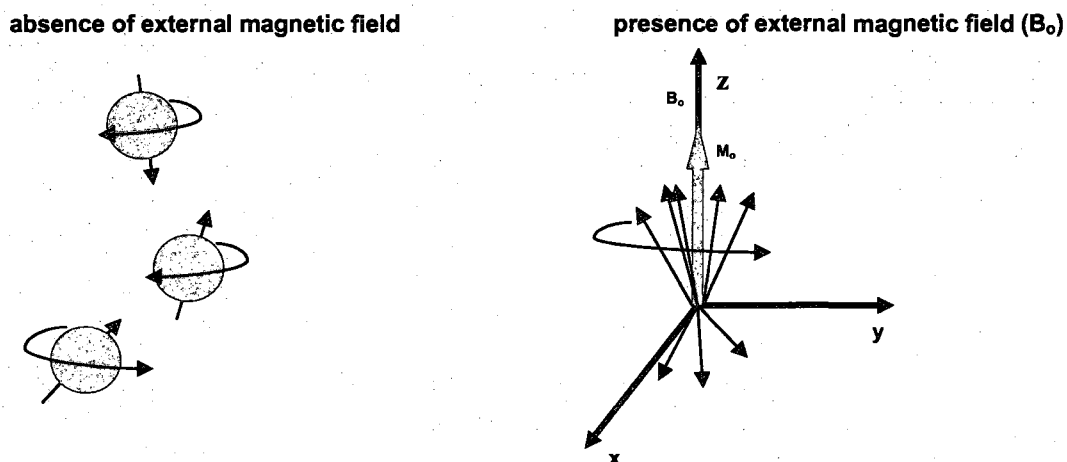


**Figure 2.1:** Illustration of spinning nuclei in the absence and presence of an external magnetic field,  $B_0$ . Note that the nuclei precess around the direction of  $B_0$ .

The precession is a common, physical phenomenon that occurs when a torque is applied to a spinning object.<sup>51</sup> The Larmor relation describes the frequency at which the nuclei precess.<sup>52</sup>

$$\nu = \frac{\gamma_g B_0}{2\pi} \quad (2.1)$$

In this equation,  $\nu$  is the Larmor frequency,  $\gamma_g$  is the gyromagnetic ratio of the nuclei, and  $B_0$  is the strength of the applied magnetic field. Each nucleus has a unique gyromagnetic ratio. Thus, the precession frequency of the magnetic moment of the nucleus is “proportional to and uniquely determined by the gyromagnetic ratio and the strength of the magnetic field.”<sup>52</sup> This thesis exclusively focuses on the measurement of the  $^1\text{H}$  nucleus. Therefore, the measurements are only sensitive to molecules which contain  $^1\text{H}$ . For  $^1\text{H}$ ,  $\gamma_g = 2.675 \times 10^8 \text{ T}^{-1} \text{ s}^{-1}$ .<sup>50</sup> Most NMR applications in the petroleum industry make use of  $^1\text{H}$  NMR.<sup>51</sup>

Millions of  $^1\text{H}$  nuclei exist in a water-in-oil emulsion. Therefore, when an external magnetic field is applied, the nuclear spins combine to form an ensemble of spins called a magnetization vector,  $M_o$ .<sup>41, 51</sup> The magnetization vector is given by Curie's Law:<sup>51, 53</sup>

$$M_o = N \frac{\gamma_g^2 h^2 I (I+1)}{3 (4 \pi^2) k T} B_o \quad (2.2)$$

The magnetization vector provides the signal that is measured by the NMR instrument. In this equation,  $N$  is the number of nuclei per unit volume,  $k$  is the Boltzman's constant,  $T$  is the absolute temperature (K),  $h$  is Planck's constant, and  $I$  is the spin quantum number of the nucleus, which is  $\frac{1}{2}$  for hydrogen.

The hydrogen nuclei align with the applied external magnetic field in a process called polarization. Polarization of a sample is not instantaneous.<sup>50</sup> The time constant that governs this polarization is referred to as the longitudinal relaxation time,  $T_1$ . The following expression relates the magnitude of the magnetization to  $T_1$ :<sup>51</sup>

$$M_z(t) = M_o (1 - e^{-\frac{t}{T_1}}) \quad (2.3)$$

The magnitude of the magnetization at a given time  $t$  is  $M_z(t)$ , and the maximum magnitude of the magnetization is  $M_o$ .  $T_1$  is defined as "the time at which the magnetization reaches 63% of its final value."<sup>51</sup> The  $T_1$  relaxation time, also referred to as the spin-lattice relaxation time, describes the relaxation of the magnetization that occurs in the direction parallel to the applied magnetic field.<sup>53</sup>

After the nuclei are polarized with the external magnetic field, the spins can be tipped by applying a radio frequency field,  $B_1$ , which is perpendicular to the external



magnetic field. The angle at which the spins are tipped is a function of the strength of  $B_1$ , as well as the duration of the application of  $B_1$ .<sup>51</sup>

$$\theta = \gamma_g B_1 t_p \quad (2.4)$$

The two tip angles used in this work are  $\pi/2$  ( $90^\circ$ ) and  $\pi$  ( $180^\circ$ ). These tip angles are used because the measurements require tipping the nuclear spins into the transverse plane with  $\pi/2$  pulses and subsequently rephasing the spins with  $\pi$  pulses. When the nuclear spins are tipped by  $\pi/2$ , the spins reside in the transverse magnetization plane.<sup>50</sup> When the perpendicular magnetic field is terminated, the spins begin to lose phase coherency. Thus, the magnetization of the spins begins to degrade. In order to re-phase the spins so that a signal can be detected, a  $\pi$  pulse is applied.

A second relaxation time exists, referred to as transverse relaxation, spin-spin relaxation or  $T_2$ , which describes the “decay of the magnetization in the transverse plane.”<sup>53</sup> After applying a  $\pi/2$  radio frequency pulse, the nuclear spins lose their phase coherency in the transverse plane. Applying subsequent  $\pi$  pulses combines the spins into a measurable signal; however, the overall magnetization amplitude decays with time as a result of transverse relaxation.<sup>50</sup> The following expression illustrates the decay of the magnetization as a function of  $T_2$ .<sup>51</sup>

$$M_{xy}(t) = M_o e^{\frac{-t}{T_2}} \quad (2.5)$$

Measuring  $T_2$  distributions is fast with experiment times approximately equal to 10 minutes.

The governing concept of NMR is the presence of angular momentum and magnetic moments in the nuclei of atoms. When the correct magnetic fields are applied, the magnetic properties of the nuclei can be exploited to produce recordable signals. The

magnetization that is detected gives information about the physical properties and characteristics of the sample. NMR measurements are not restricted by optical properties of the sample, and the sample is not harmed as a result of the measurements.

## 2.3 Carr-Purcell-Meiboom-Gill (CPMG) Technique

As mentioned in the previous section, when the magnetic spins tip into the transverse plane, the recordable magnetization of the spins decays with time according to  $T_2$ . Multi-component fluids, such as crude oil, have broad  $T_2$  distributions. However, pure fluids, like water, have narrow  $T_2$  distributions. Therefore,  $T_2$  distributions distinguish different fluids that exist in a sample.

The most commonly used technique to measure transverse relaxation is referred to as the Carr-Purcell-Meiboom-Gill (CPMG) technique.

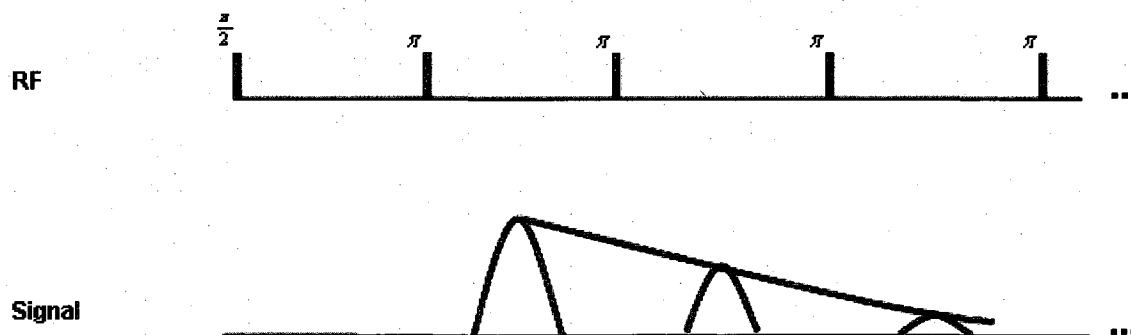


**Figure 2.2:** The CPMG pulse sequence. As time progresses, the magnetization vector in the transverse plane decays according to the transverse relaxation time ( $T_2$ ) (adapted from Peña 2006).<sup>4</sup>

The  $\pi/2$  pulse tips the nuclear spins to the transverse plane. Upon reaching the transverse plane, the nuclear spins immediately begin to lose phase coherency. The  $\pi$  pulses rephase the spins to ensure a recordable signal. The measurement usually requires approximately ten minutes.

The decay of the magnetization vector in the transverse plane,  $M_{xy}$ , is governed by a multi-exponential function.<sup>41</sup>

$$\frac{M_{xy}(2n\tau)}{M_{xy}(0)} = \sum_{i=1}^m f_i \exp\left(-\frac{2n\tau}{T_{2,i}}\right) \quad (2.6)$$

To obtain a  $T_2$  distribution, the multi-exponential function is fit to the experimental data.

Based on the designated list of  $T_2$  values, a corresponding list of  $f_i$  values is obtained.

The  $f_i$  values represent the fraction of the  $^1\text{H}$  nuclei which have a relaxation time of  $T_{2,i}$ .

Because this formulation is ill posed, multiple lists of  $f_i$  satisfy the fitting.<sup>54</sup> A

regularization method developed by Huang provides the best fit to the multi-exponential function.<sup>55, 56</sup> The following figure is an example of a  $T_2$  distribution of an emulsion.

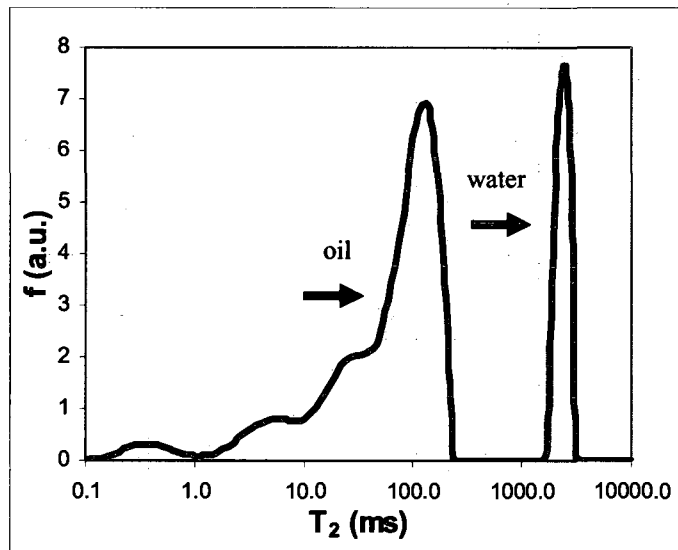


**Figure 2.3:** Example of a  $T_2$  distribution of a water-in-oil emulsion. Note that the oil and water are separated according to their  $T_2$  distributions.

In this thesis,  $T_2$  distributions are employed in a variety of ways when working with emulsified systems. If the water and oil contributions are separable in terms of  $T_2$ , as in Figure 2.3, important system properties such as water fraction can be determined. In addition,  $T_2$  distributions can be used to determine the drop size distribution of an

emulsion. The transverse relaxation of the dispersed phase can be written as the sum of bulk relaxation and surface relaxation.<sup>51</sup>

$$\frac{1}{T_2} = \frac{1}{T_{2,bulk}} + \frac{1}{T_{2,surface}} \quad (2.7)$$

Brownstein and Tarr showed that the contribution from surface relaxation can be written in terms of the geometry of the system and the surface relaxivity.<sup>57</sup>

$$\frac{1}{T_{2,i}} = \frac{1}{T_{2,bulk}} + \rho \left( \frac{S}{V} \right) \quad (2.8)$$

In this equation,  $\rho$  is the surface relaxivity and  $S/V$  is the surface to volume ratio of the drop. Assuming that the dispersed phase is composed of spheres, the drop diameter distribution is determined directly from the  $T_2$  distribution.

$$d_i = 6 \rho \left( \frac{1}{T_{2,DP,i}} - \frac{1}{T_{2,bulk}} \right)^{-1} \quad (2.9)$$

The drop size distribution can be calculated given the  $T_2$  distribution of the dispersed water ( $T_{2,DP,i}$ ), surface relaxivity, and the bulk water  $T_2$  value ( $T_{2,bulk}$ ).

There are limitations on the use of Equation 2.9. The surface relaxivity and bulk relaxation time of the dispersed phase must be known. The transverse relaxation of the dispersed phase must not overlap either the bulk oil or bulk water transverse relaxation distributions. In addition, measurements must be performed within the fast diffusion limit. The fast diffusion limit occurs when the diffusion time of water molecules from the center of the drop to the surface is much faster than the time for surface relaxation to occur.<sup>41</sup> The characteristic time for diffusion is given by the following expression.<sup>41</sup>

$$t_D = \frac{r^2}{D_{DP}} \quad (2.10)$$

The diffusivity of the dispersed phase is given by  $D_{DP}$  and the radius is  $r$ . The characteristic time for surface relaxation is a function of drop size and surface relaxation.<sup>41</sup>

$$t_{\rho} = \frac{r}{\rho} \quad (2.11)$$

The ratio of the time for diffusion and time for relaxation should be much less than one, but practically less than or equal to 0.25.<sup>41</sup>

$$\frac{t_D}{t_{\rho}} = \frac{\rho r}{D_{DP}} \leq \frac{1}{4} \quad (2.12)$$

Therefore, the maximum diameter determined by the fast diffusion limit is described by the ratio of the diffusivity of the bulk phase and the surface relaxivity.<sup>41</sup>

$$d_{\max, FDL} = \frac{D_{DP}}{2 \rho} \quad (2.13)$$

## 2.4 Pulsed Field Gradient (PFG) Technique

The previously discussed CPMG technique does not account for diffusion of the molecules in the sample. Through the implementation of an external magnetic field gradient, the pulsed field gradient with stimulated echoes (PFG) technique is commonly implemented to measure the diffusion of molecules in a sample and thereby characterize drop size distributions of water-in-oil emulsions.<sup>4, 58</sup> A magnetic gradient imparts a range of magnetic field values in the spins throughout the sample. To measure the diffusion, measurements are taken with and without the gradient. In both cases, the amplitude of the resulting spin echoes is measured.

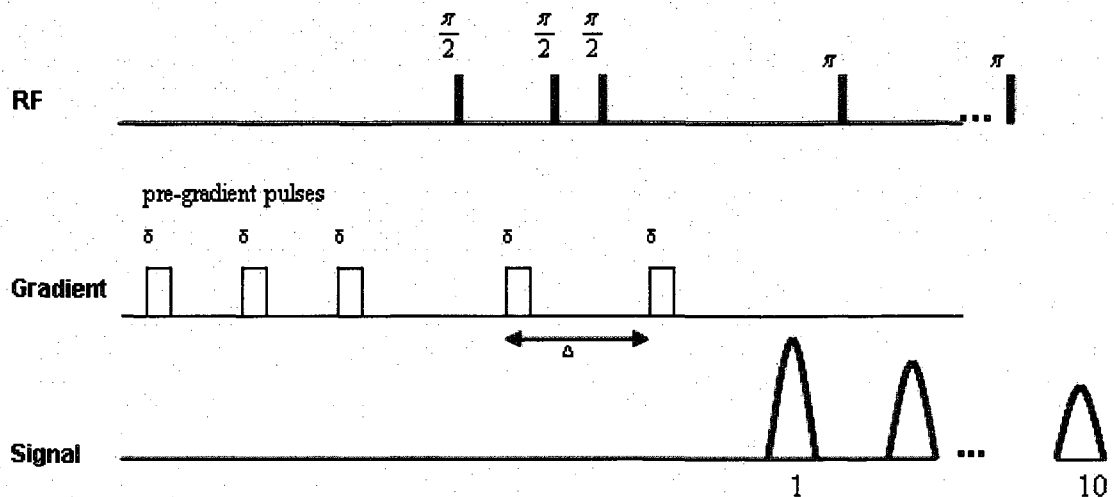


**Figure 2.4:** Pulsed field gradient (PFG) pulse sequence with stimulated echoes and pre-gradient pulses. The amplitudes of the first 10 echoes are fit by linear regression to obtain the amplitude of the first echo.

Figure 2.4 shows the pulsed field gradient pulse sequence with stimulated echoes and pre-gradient pulses. Three to nine pre-gradient pulses should be used to make the final two gradient pulses identically shaped. In this thesis, the gradient strength values were manipulated in each experiment to facilitate attenuation of the emulsion signal. The amplitude of the first echo is obtained by linearly fitting the amplitudes of the first ten echoes, thereby increasing the SNR of the measurement.

The duration of the gradient pulse is given by  $\delta$ . The gradient pulses are separated by a time which is referred to as the diffusion time,  $\Delta$ . The diffusion time is the time when the molecules diffuse and physically change location. The ratio of the two magnetization values is called the attenuation:<sup>41</sup>

$$R = \frac{M(2\tau, g, \Delta, \delta, D_{DP})}{M(2\tau, g = 0, \Delta, \delta)} \quad (2.14)$$

The attenuation of the signal in a PFG measurement is coupled with the model developed by Murday and Cotts<sup>59</sup> for diffusion in spheres to obtain the drop size

distribution of the emulsion. The model for attenuation of the signal of fluid confined in spheres is given by Equations 2.15 – 2.17.<sup>59, 60</sup>

$$R_{sp} = \exp \left\{ -2 \gamma_g^2 g^2 \sum_{m=1}^{\infty} \frac{1}{\alpha_m^2 (\alpha_m^2 r^2 - 2)} \left[ \frac{2 \delta}{\alpha_m^2 D_{DP}} - \frac{\Psi}{(\alpha_m^2 D_{DP})^2} \right] \right\} \quad (2.15)$$

$$\Psi = 2 + \exp(-\alpha_m^2 D_{DP} (\Delta - \delta)) - 2 \exp(-\alpha_m^2 D_{DP} \delta) - 2 \exp(-\alpha_m^2 D_{DP} \Delta) + \exp(-\alpha_m^2 D_{DP} (\Delta + \delta)) \quad (2.16)$$

The gyromagnetic ratio is given by  $\gamma_g$ , the gradient strength is  $g$ ,  $D_{DP}$  is the diffusivity of the fluid in the dispersed phase,  $r$  is the radius of the emulsion droplet,  $\Delta$  is the time between gradient pulses,  $\delta$  is the gradient pulse duration, and  $\alpha_m$  is the  $m^{\text{th}}$  positive root of Equation 2.17.

$$\frac{1}{\alpha r} J_{3/2}(\alpha r) = J_{5/2}(\alpha r) \quad (2.17)$$

$J_k$  is the Bessel function of the first kind with order  $k$ . The overall attenuation of the emulsion has been shown to be a function of the attenuation of both the continuous and dispersed phases.<sup>4</sup>

$$R_{emul} = (1 - \kappa) R_{DP} + \kappa R_{CP}; \quad 0 \leq \kappa \leq 1.0 \quad (2.18)$$

The fraction of the attenuation from the continuous phase is given by the parameter,  $\kappa$ .<sup>4</sup>

$$\kappa = \left[ 1 + \frac{\sum (f_i)_{DP} \exp \left[ \frac{-(\Delta + \tau)}{(T_{2,i})_{DP}} \right]}{\sum (f_i)_{CP} \exp \left[ \frac{-(\Delta + \tau)}{(T_{2,i})_{CP}} \right]} \right]^{-1} \quad (2.19)$$

The  $T_{2,i}$  and  $f_i$  values are obtained from a CPMG measurement. The time between the first and second  $\pi/2$  pulses is  $\tau$ . The attenuation of the continuous phase,  $R_{CP}$ , is given by Equation 2.20.

$$R_{CP} = \exp\left(-\gamma_g^2 g^2 D_{CP} \delta^2 \left(\Delta - \frac{\delta}{3}\right)\right) \quad (2.20)$$

The attenuation of the dispersed phase,  $R_{DP}$ , is given by Eq. 2.21.<sup>61</sup>

$$R_{DP} = \frac{\int_0^{\infty} p(r) R_{sp(r)} dr}{\int_0^{\infty} p(r) dr} \quad (2.21)$$

The PFG technique requires the assumption of the functional form of the drop size distribution which is commonly assumed to be the lognormal probability density function.<sup>62</sup>

$$p(r) = \frac{1}{2 r \sigma (2 \pi)^{\frac{1}{2}}} \exp\left(-\frac{(\ln(2 r) - \ln(d_v))^2}{2 \sigma^2}\right) \quad (2.22)$$

The volume weighted mean is given by  $d_v$ , and the width of the distribution is  $\sigma$ .

The PFG technique involves obtaining attenuation of the signal as a function of gradient strength and subsequently fitting the experimental attenuation to the predicted attenuation according to the restricted diffusion model by adjusting  $d_v$  and  $\sigma$ . For this work, a nonlinear least squares algorithm with optimization was used to perform the fitting (lsqcurvefit in MatLab 7.1, The MathWorks Inc.).

One of the biggest limitations of the PFG technique is the assumption that the drop size distribution must follow a specific distribution, such as the lognormal distribution. Though the drop size distributions of emulsions can be lognormal, there are cases when the distribution is not necessarily lognormal.<sup>63</sup> By forcing the shape of the distribution to be lognormal, valuable information about the actual shape of the distribution can be lost.



## 2.5 Pulsed Field Gradient with Diffusion Editing (PFG-DE) Technique

The PFG pulse sequence can be modified to include several thousand  $\pi$  pulses at the end of the gradient sequence to gather transverse relaxation information.<sup>46,47</sup>

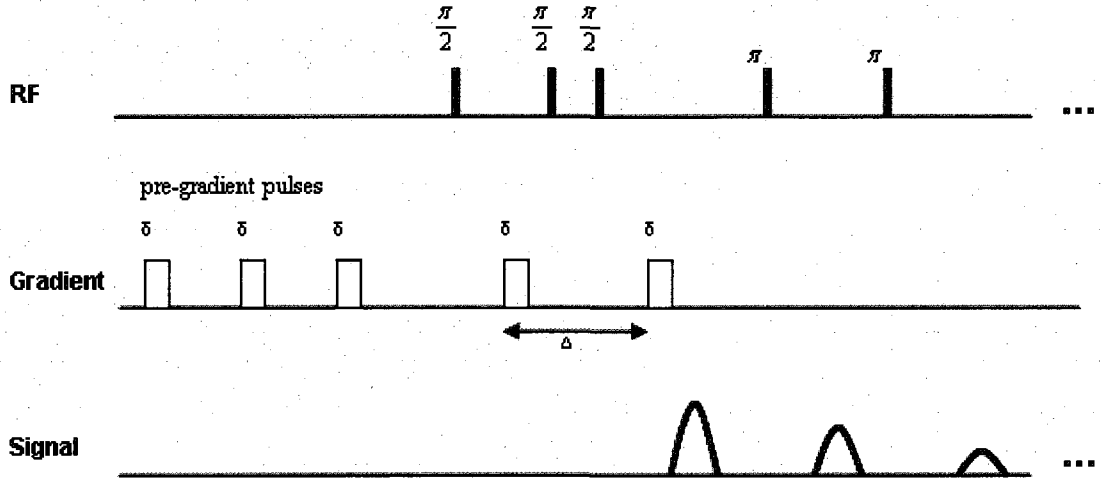


**Figure 2.5:** Pulsed field gradient with diffusion editing (PFG-DE) pulse sequence.

Similar to the PFG technique, the gradient values are manipulated to facilitate attenuation due to restricted diffusion. However, the PFG-DE technique acquires thousands of echoes, thus resulting in the attainment of both diffusion and transverse relaxation information.

Flaum derived the magnetization equation used to characterize restricted diffusion in spheres and transverse relaxation simultaneously.<sup>46</sup>

$$M_{xy}(g, t) = \iint f(r, T_2) \exp\left(-\frac{t}{T_2}\right) R_{sp}(\Delta, \delta, g, r) \exp\left(-\frac{\Delta + \delta}{T_1} - 2\delta\left(\frac{1}{T_2} - \frac{1}{T_1}\right)\right) dr dT_2 \quad (2.23)$$

The longitudinal relaxation time,  $T_1$ , was assumed to be equal to  $T_2$  in this work, which is a valid assumption for liquids at 2 MHz.<sup>64</sup> The attenuation of the brine drops according to Equations 2.15 - 2.17 is given by  $R_{sp}$ .

The distribution of both drop size and transverse relaxation,  $f(r, T_2)$ , is determined using a two dimensional inversion with regularization.<sup>46-48</sup> Figure 2.6 shows an example of the two dimensional information that is obtained from this measurement.

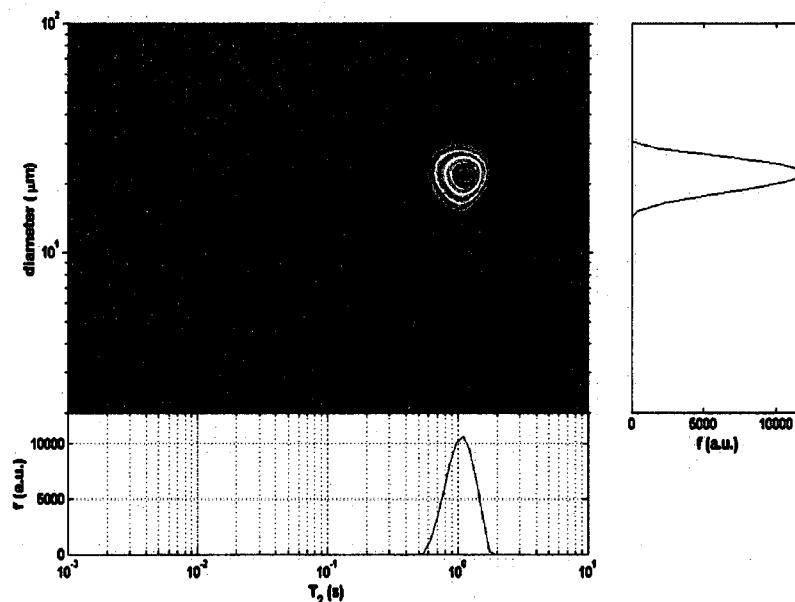


**Figure 2.6:** Example of the two dimensional result obtained from the PFG-DE technique. Recently, this technique was shown to resolve drop size distributions of multimodal drop size distributions because the form of the drop size distribution is not assumed, thereby making it a robust technique to investigate complex emulsified systems.<sup>11</sup>

## 2.6 Rapid Acquisition with Relaxation Enhancement (RARE)

The rapid acquisition with relaxation enhancement (RARE) technique captures one dimensional imaging information.<sup>49</sup>

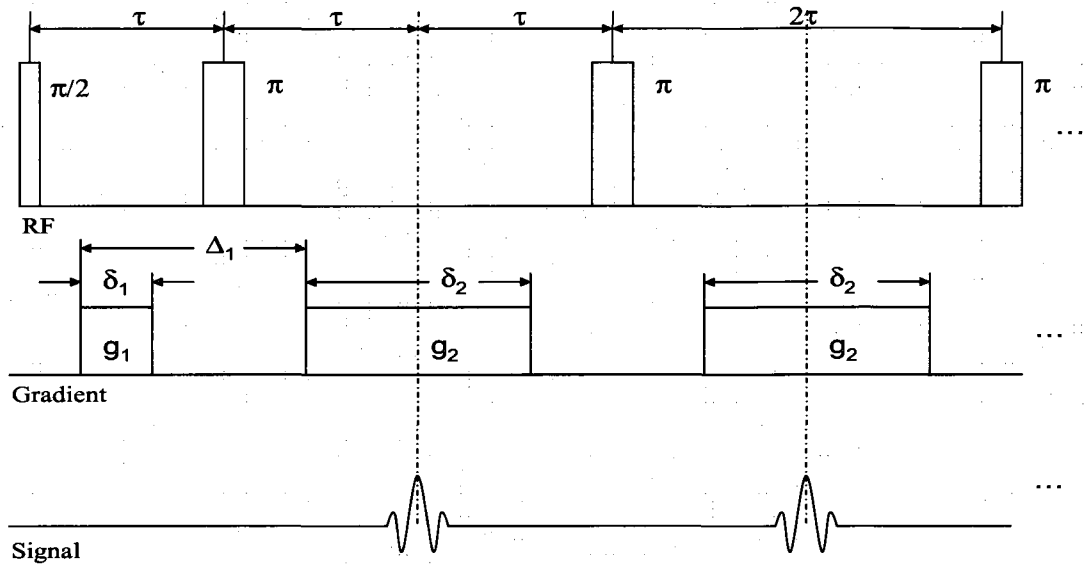


**Figure 2.7:** Pulse sequence for the RARE technique (from Rauschhuber, 2007).<sup>65</sup>

The RARE technique is useful for gaining vertical morphological information about emulsion samples. The technique obtains transverse relaxation distributions at slices throughout the height of the sample, thus yielding a vertical map of the distribution of fluids in the sample.

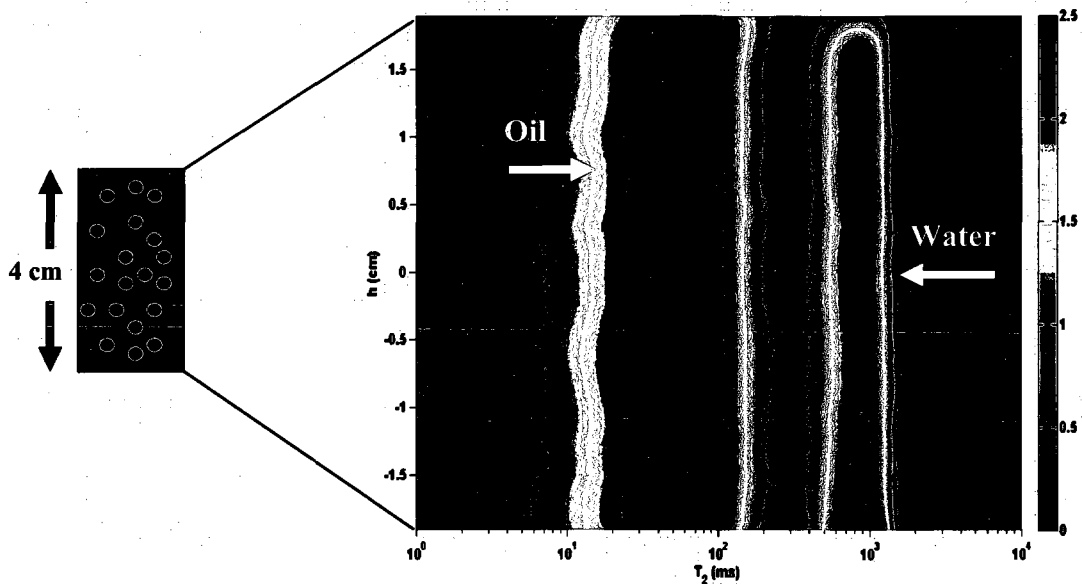


**Figure 2.8:** Example of a typical vertical image of an emulsion produced by the RARE technique. Note the distinction between oil and water in the sample.

Figure 2.8 shows that the RARE technique differentiates between oil and water and thereby provides the spatial distribution of each phase in the sample.

## 2.7 Conclusions

Nuclear magnetic resonance is a particularly useful tool to investigate water-in-oil emulsions. This thesis employs four techniques to quantify emulsion formation, stability, and methane hydrate formation in water-in-oil emulsions. The CPMG technique measures transverse relaxation which leads to obtaining the drop size distribution and quantifying methane hydrate formation. The PFG and PFG-DE techniques exploit the diffusion of water molecules to measure drop size distributions of emulsions. Finally, the RARE technique provides spatial, morphological information about the emulsions. These techniques provide a comprehensive evaluation of emulsified systems which lead to insight about emulsion formation, stability, and methane hydrate formation in water-in-oil emulsions.

## 2.8 Notation

$B_o$	stationary magnetic field (T)
$B_I$	applied magnetic field (T)
$D_{DP}$	diffusivity of dispersed phase ( $\text{cm}^2/\text{s}$ )
$D_{CP}$	diffusivity of continuous phase ( $\text{cm}^2/\text{s}$ )
$d_{\text{max},FDL}$	max. diameter determined by the Fast Diffusion Limit ( $\mu\text{m}$ )
$d_i$	drop size of the $i^{\text{th}}$ bin ( $\mu\text{m}$ )
$d_v$	volume weighted mean diameter ( $\mu\text{m}$ )
$f_i$	amplitude of the $i^{\text{th}}$ bin (arbitrary units)
$g$	gradient strength (T/m)
$h$	Planck's constant
$I$	spin quantum number
$J_k$	Bessel function of the 1 <sup>st</sup> kind with order k
$k$	Boltzmann's constant
$M_o$	initial magnetization
$M_{xy}$	transverse magnetization

$M_z$	longitudinal magnetization
$m$	number of bins in the $T_2$ distribution
$N$	number of nuclei per unit volume
$n$	echo number
$p(r)$	probability distribution function
$R$	attenuation
$R_{CP}$	attenuation of continuous phase
$R_{DP}$	attenuation of dispersed phase
$R_{sp}$	attenuation of a sphere
$R_{emul}$	overall attenuation of the emulsion
$r$	radius of drop ( $\mu\text{m}$ )
$(S/V)_{drop}$	surface area to volume ratio of a drop ( $1/\text{m}$ )
$T$	absolute temperature (K)
$T_1$	longitudinal relaxation (ms)
$T_2$	transverse relaxation (ms)
$T_{2,bulk}$	bulk $T_2$ of dispersed phase (ms)
$T_{2,DP,i}$	dispersed phase $T_2$ of the $i^{\text{th}}$ bin (ms)
$T_{2,surface}$	$T_2$ that occurs at a surface (ms)
$t$	experiment time (s)
$t_D$	diffusion time from the interior of the drop to the surface (s)
$t_p$	pulse duration (s)
$t_\rho$	time scale for surface relaxation ( $\mu\text{m/s}$ )
$\alpha_m$	$m^{\text{th}}$ positive root of the Bessel function
$\nu$	Larmor frequency ( $1/\text{s}$ )
$\gamma_g$	gyromagnetic frequency ( $\text{T}^{-1} \text{s}^{-1}$ )
$\theta$	tip angle (radians)
$\tau$	time between $\pi/2$ and $\pi$ pulses ( $\mu\text{s}$ )
$\rho$	surface relaxivity ( $\mu\text{m/s}$ )
$\delta$	gradient pulse duration ( $\mu\text{s}$ )
$\Delta$	time between gradient pulses ( $\mu\text{s}$ )
$\kappa$	fractional contribution of continuous phase to overall attenuation
$\sigma$	standard deviation of drop size distribution ( $\mu\text{m}$ )

## **Chapter 3: Water-in-Oil Emulsion Droplet Size Characterization Using a Pulsed Field Gradient with Diffusion Editing (PFG-DE) NMR Technique**

### ***3.1 Introduction***

Historically, researchers have attempted to measure drop size distributions of emulsions using techniques including microscopy, light scattering, Coulter counting, and nuclear magnetic resonance.<sup>1, 4, 15</sup> For brine-in-crude-oil emulsions, nuclear magnetic resonance is a superior technique because it is not destructive to the emulsion, it considers the entire sample, and it is not restricted by the fact that brine-in-crude-oil emulsions do not transmit an appreciable amount of light. Traditionally, NMR has been used to measure drop size distributions of emulsions according to the technique developed by Packer and Rees.<sup>61</sup> The Packer-Rees technique incorporates the idea of restricted diffusion established by Neuman<sup>60</sup> and refined by Murday and Cotts<sup>59</sup> for diffusion in spheres.

The method presented by Packer and Rees relies on the assumption that the drops in emulsions are distributed in size according to the lognormal distribution. This restriction often results in the loss of valuable information about the actual emulsion drop size distribution. Therefore, techniques have been developed and discussed in the literature that are designed to yield more general information about drop size distributions of emulsions, independent of the assumption that the drops are lognormally distributed.<sup>66</sup>

This work presents a new technique that provides both the  $T_2$  and drop size distributions of brine-in-crude-oil emulsions simultaneously, referred to as the pulsed field gradient with diffusion editing (PFG-DE) technique. This chapter also presents an

algorithm that can be used to calculate parameters for both PFG-DE and PFG experiments for a variety of emulsion conditions. The PFG-DE technique involves a two dimensional inversion with regularization much like that used for obtaining diffusivity and transverse relaxation information.<sup>46-48</sup> The drop size distributions obtained from the PFG-DE technique are compared to drop size distributions obtained from the stimulated echo pulsed field gradient (PFG) technique.<sup>4, 58</sup> In this work, the PFG-DE technique is shown to be useful for obtaining drop size distributions when the  $T_2$  distribution of the emulsified brine overlaps either the bulk brine or crude oil  $T_2$  distribution. Finally, the utility of the PFG-DE technique is particularly observed when the drop size distribution of the emulsion is more complicated, such as when the distribution is bimodal.

### 3.2 Experimental Methods

The  $^1\text{H}$  NMR measurements discussed in this chapter were performed on a 2 MHz Maran Ultra spectrometer that was maintained at  $30 \pm 0.1^\circ\text{C}$ .

#### 3.2.1 Carr-Purcell-Meiboom-Gill (CPMG)

As described in Chapter 2, the Carr-Purcell-Meiboom-Gill (CPMG) technique measures transverse relaxation distributions of emulsions.<sup>43, 44</sup> After obtaining the  $T_2$  distribution, the resulting drop size distribution can be determined according to Equation 3.1.<sup>4</sup>

$$d_i = 6 \rho \left( \frac{1}{T_{2,DP,i}} - \frac{1}{T_{2,bulk}} \right)^{-1} \quad (3.1)$$

The surface relaxivity,  $\rho$ , is determined either by combining a CPMG and PFG measurement<sup>66</sup> or by performing a PFG-DE measurement. The bulk transverse relaxation

time of the fluid that is confined in the drops is given by  $T_{2,bulk}$ . Equation 3.1 is useful for determining drop size distributions of emulsions when the transverse relaxation distribution of the emulsified brine is separated from both the crude oil distribution and the bulk brine distribution.

### 3.2.2 Pulsed Field Gradient (PFG) and Pulsed Field Gradient with Diffusion Editing (PFG-DE)

As described in Chapter 2, the pulsed field gradient (PFG) technique is the traditional diffusion NMR technique to measure emulsion droplet size distributions.<sup>61</sup> The standard PFG pulse sequence can be modified to include several thousand  $\pi$  pulses at the end of the gradient sequence to gather transverse relaxation information.<sup>46, 47</sup> This chapter compares the PFG-DE technique to the standard PFG technique, and thereby illustrates the effectiveness of the PFG-DE technique. In addition, this chapter shows that the PFG-DE technique yields more detailed morphological information about emulsions than the traditional PFG technique.

The parameters that are used in both the PFG and PFG-DE techniques are obtained by solving the series model for restricted diffusion in spheres given by Murday and Cotts.<sup>46, 59</sup> Specifically, the primary parameters that affect both the PFG-DE and PFG measurements are the time between gradient pulses ( $\Delta$ ), gradient duration ( $\delta$ ), and gradient strength ( $g$ ). Both physical and equipment constraints must be accounted for when determining the parameters for a given experiment. Selection of  $\Delta$  must be made based on the range of sizes of the drops expected in the sample and the SNR of the system. To distinguish restricted diffusion from free diffusion, the dimensionless time between gradient pulses must be greater than or equal to 1.0.<sup>46</sup>



$$\frac{2 D_{DP} \Delta}{r^2} \geq 1.0 \quad (3.2)$$

If  $\Delta$  is too small, the measurement will not be sensitive to large drops. If  $\Delta$  is too large, the SNR will be low because of  $T_2$  relaxation of the drops.

$$\frac{r^2}{2 D_{DP}} \leq \Delta \leq 0.3 T_{2,DP} \quad (3.3)$$

Therefore, to investigate the largest possible sphere sizes,  $\Delta$  must be as large as possible but less than a fraction of the dispersed phase transverse relaxation time. After  $\Delta$  is established, the gradient duration,  $\delta$ , is calculated. The minimum value of the gradient duration is instrument specific, and the maximum value is based on an established rule of thumb.<sup>46</sup>

$$\delta_{\min} \leq \delta \leq 0.2 \Delta \quad (3.4)$$

With the gradient spacing and duration calculated, the gradient values that achieve the desired attenuation can be calculated using the previously described series model for restricted diffusion in spheres. Ideally, for a given sphere size, the attenuation should range from 0.99 to 0.01.<sup>46</sup>

Figure 3.1 illustrates the relationship between the parameters in a given experiment.

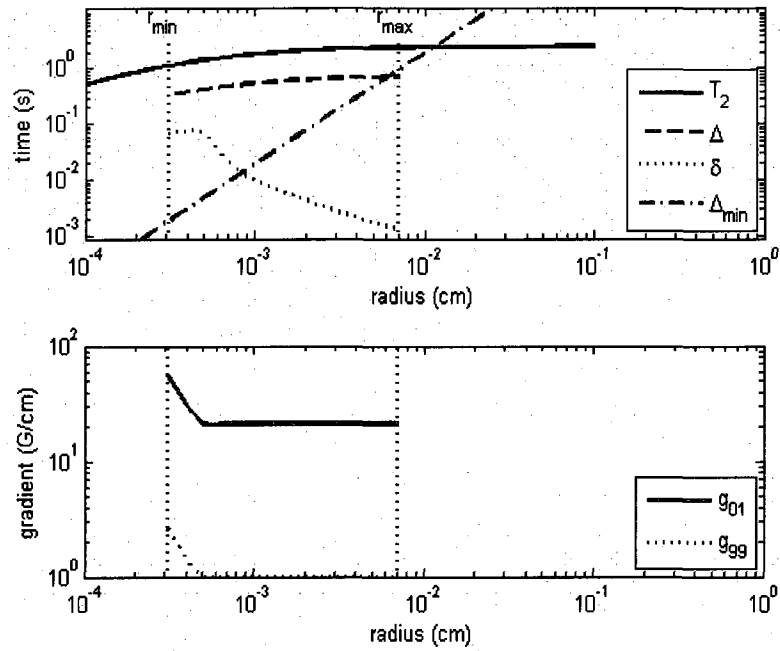


**Figure 3.1:** Example of parameters calculated for PFG-DE and PFG measurements. These parameters were calculated with ( $\rho = 1.0 \mu\text{m/s}$ ,  $D_{DP} = 2.6 \times 10^{-9} \text{ m}^2/\text{s}$ ,  $T_{2,bulk} = 2.5 \text{ s}$ , and  $\Delta/T_{2,DP} = 0.3$ ).

In the top figure, the solid curve shows the  $T_2$  distribution of the dispersed fluid. The dashed curve is the time between the two gradient pulses in the pulse sequence,  $\Delta$ , and the dotted curve is the gradient duration,  $\delta$ . The minimum time between gradient pulses,  $\Delta_{min}$ , is shown as the dashed-dotted line in the top figure. When the calculated  $\Delta$  falls below  $\Delta_{min}$ , the measurement is no longer sensitive to restricted diffusion, thus resulting in the maximum detectable drop size,  $r_{max}$ . The minimum detectable drop size,  $r_{min}$ , is calculated based on the maximum gradient duration and maximum gradient strength of the instrument. Finally, the bottom figure contains the range of gradient values that facilitate the desired amount of attenuation ranging from 1% signal remaining,  $g_{01}$ , to 99% signal remaining,  $g_{99}$ . In this work, 20 – 25 logarithmically spaced gradient values were calculated for each parameter set. If the drop size range of the system is not known

before the measurement, one PFG measurement can be performed which gives an estimate of the range of drop sizes in the system.

For all PFG-DE measurements discussed in this chapter, 32 scans were applied, 15,360 echoes were collected with the echo spacing equal to 600  $\mu$ s, and the relaxation delay was equal to 10 s. With these parameters, a typical measurement required 5 – 7 hours for each parameter set. The PFG-DE technique is not affected by sedimentation of the drops in the emulsion; however, the technique is sensitive to coalescence. Therefore, the PFG-DE technique is applicable to emulsions that resist coalescence for many hours.<sup>5, 27-29, 67</sup> Though this work is focused on brine-in-crude-oil emulsions, oil-in-water emulsions could also be investigated using the PFG-DE technique with the described parameter selection method. A possible problem that could occur with oil-in-water emulsions is that  $\Delta$  might be required to be long to characterize larger drops, thus resulting in a significant loss of signal due to  $T_2$  relaxation of the oil.

Using a technique developed by Flaum, multiple sets of parameters can be used to characterize a given drop size range.<sup>46</sup> This technique, referred to as masking, incorporates multiple parameter sets with each set optimized for a particular radius and consisting of one  $\Delta$  value, one  $\delta$  value, and a logarithmically spaced list of gradient strength values. For drop size masking, the masking technique weights the most sensitive drop size range of each parameter set based on the attenuation imparted by the parameter set and the SNR of the measurement. Figure 3.2 shows the attenuation curves that were obtained with  $\Delta = 244$  ms,  $\delta = 49$  ms, and  $g = 2 - 47$  G/cm.

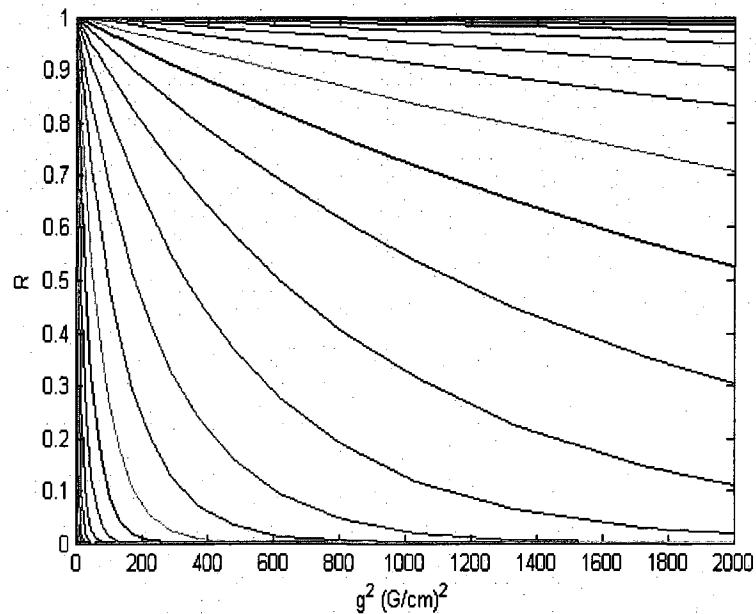


**Figure 3.2:** Attenuation of 60 drop sizes using one parameter set ( $\Delta = 244$  ms,  $\delta = 49$  ms,  $g = 2 - 47$  G/cm).

Each curve in Figure 3.2 represents the attenuation imparted by a given parameter set to fluids diffusing in a specific sphere size. In this figure, the attenuation curves from 60 different radii logarithmically spaced between 0.00001 cm and 0.1 cm are displayed.

The attenuation for each parameter set can be used to determine the sensitivity of each parameter set. Figure 3.3 illustrates the determination of the sensitive region of each parameter set by plotting the sums of the square differences of attenuation between each drop size and the two adjacent drop sizes for five parameter sets.

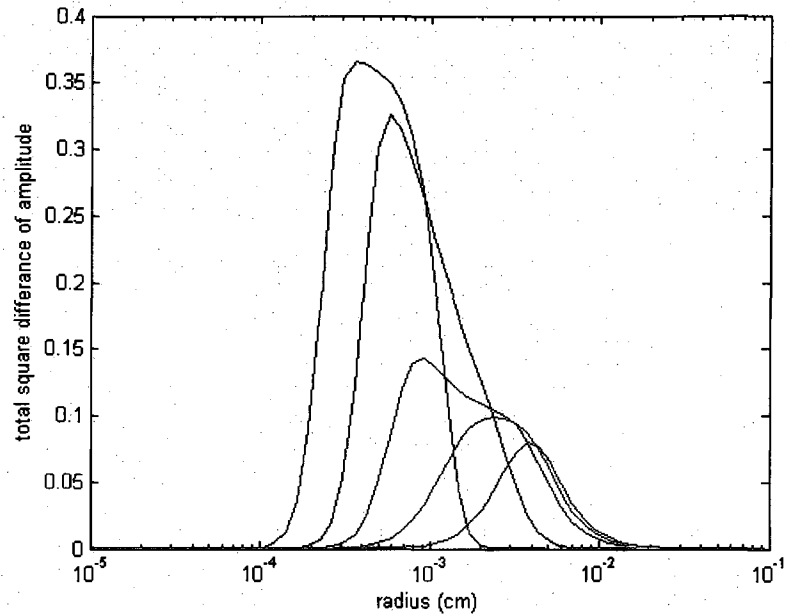


**Figure 3.3:** Sensitivity of five parameter sets.

At each gradient value, the attenuation of one sphere size is compared to the attenuation of the two adjacent sphere sizes to ensure that the sphere sizes can be distinguished. The limit of each parameter set is dictated by the noise of the measurement.

$$cutoff = 2 (\sigma_{noise})^2 N_{grad} \quad (3.5)$$

In this equation, the standard deviation of the noise is given by  $\sigma_{noise}$  and the number of gradients is given by  $N_{grad}$ . The intersections of the value obtained from Equation 3.5 with the sensitivity curves in Figure 3.3 designate the boundaries of the sensitivity of each parameter set. For this example, the cutoff was calculated to be 0.001, resulting in Figure 3.4.

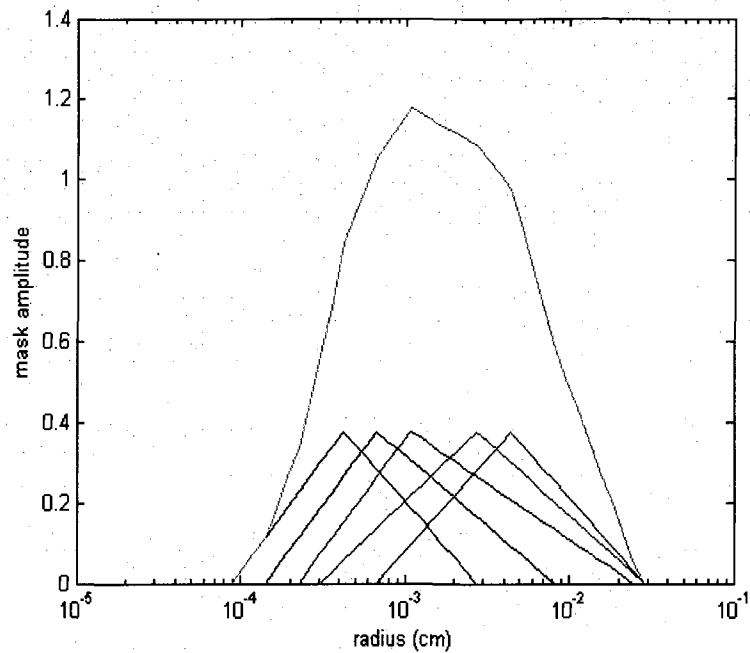


**Figure 3.4:** Drop size masks for each parameter set.

The masks have maximum amplitude at the radii for which the parameters are most sensitive, and the range extends to the boundaries of the sensitivity of each parameter set as determined by Equation 3.5. The masked drop size distribution is a weighted sum of the drop size distribution obtained from each parameter set divided by the amplitude of the combined mask.

Similarly, the transverse relaxation distribution is masked according to  $\Delta$ . In this work, transverse relaxation times shorter than half of  $\Delta$  were masked. The masking proceeds linearly in  $\log T_2$  until the value of  $\Delta$  is reached as shown in Figure 3.5 for five parameter sets.

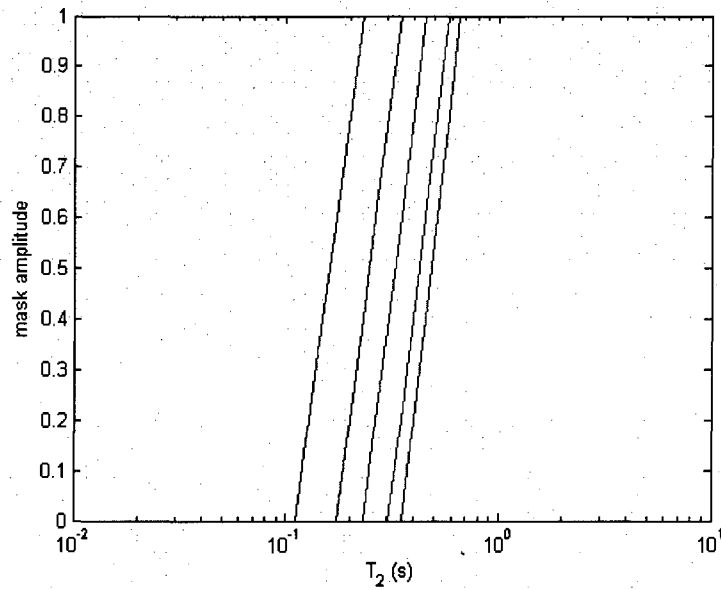


**Figure 3.5:**  $T_2$  masking for five parameter sets.

Any component that has a relaxation time significantly faster than  $\Delta$  will have relaxed substantially before the first echo is collected. In this work, components that relaxed faster than 0.5 times  $\Delta$  were masked which corresponded to a decrease in signal amplitude of 85%. The fast relaxing crude oil components were the only species affected by the  $T_2$  masking in this work.

Table 3.1 contains the NMR parameters that were calculated for each of the three experiments discussed in this chapter.

**Table 3.1:** Experimental NMR parameters.

experiment #	$d_{optimal}$ ( $\mu\text{m}$ )	$\Delta$ (ms)	$\delta$ (ms)	$g$ (G/cm)	$d_{range}$ ( $\mu\text{m}$ )
1	20	598	5.7	1 - 10	10 - 140
2	10	552	28	1 - 13	5 - 60
3, first set	10	470	28	1 - 15	5 - 70
3, second set	20	598	5.7	1 - 10	10 - 140

### 3.2.3 Emulsion preparation

The emulsions considered in this work were prepared using a Taylor-Couette flow device. The rotating, inner cylinder was composed of Torlon with radius,  $r_T = 19.1$  mm. The stationary, outer cylinder was composed of glass with radius,  $r_g = 21.6$  mm. The rotational speed of the inner cylinder,  $\omega$ , was adjusted depending on the desired experimental conditions. Each emulsion was sheared for 10 minutes.

The sample temperatures were not measured during the NMR measurements. However, all samples were placed into a temperature controlled spectrometer at  $30 \pm 0.1^\circ\text{C}$  during the NMR measurements. For all of the emulsions discussed, the dispersed phase was ASTM synthetic seawater, also referred to as ASTM brine. Two different crude oils were used for the continuous phase, denoted as either crude oil A or crude oil B. Table 3.2 contains density and viscosity information of the fluids.

**Table 3.2:** Density and viscosity information of the fluids used in this work.

fluid type	density (g/mL)	viscosity (cP)
ASTM brine	1.03	1.2
crude oil A	0.85	20
crude oil B	0.81	2

Each emulsion discussed in this chapter contained 20 vol. % brine and 80 vol. % crude oil. After forming each emulsion, the glass sample vessel containing the emulsion was placed in the NMR instrument. Table 3.3 summarizes the formation conditions and measurement durations for the three experiments presented in this work.

**Table 3.3:** Summary of formation conditions and measurement durations for the three experiments.

experiment #	$\omega$ (rpm)	measurement duration (hr.)
1	1600	7
2	4000	7
3	1600, 2875	25

### 3.3 Results



The following sections contain three different cases that show the usefulness of the PFG-DE technique. The first case illustrates a situation when the  $T_2$  distribution of the emulsified brine overlaps the bulk brine  $T_2$  distribution. The second case illustrates the situation when the  $T_2$  distribution of the emulsified brine overlaps the  $T_2$  distribution of the crude oil. Finally, the third case illustrates the ability of the PFG-DE technique to resolve a bimodal drop size distribution.

### 3.3.1 Emulsified brine $T_2$ distribution overlaps the bulk brine $T_2$ distribution (experiment # 1, crude oil A)

Drop size distributions of brine-in-crude-oil-A emulsions were obtained using the CPMG, PFG-DE, and PFG techniques. Figure 3.6 shows the  $T_2$  distribution of an emulsion that was formed by combining 10 mL of brine with 40 mL of crude oil A.

Shear was applied to the emulsion with  $\omega = 1600$  rpm.

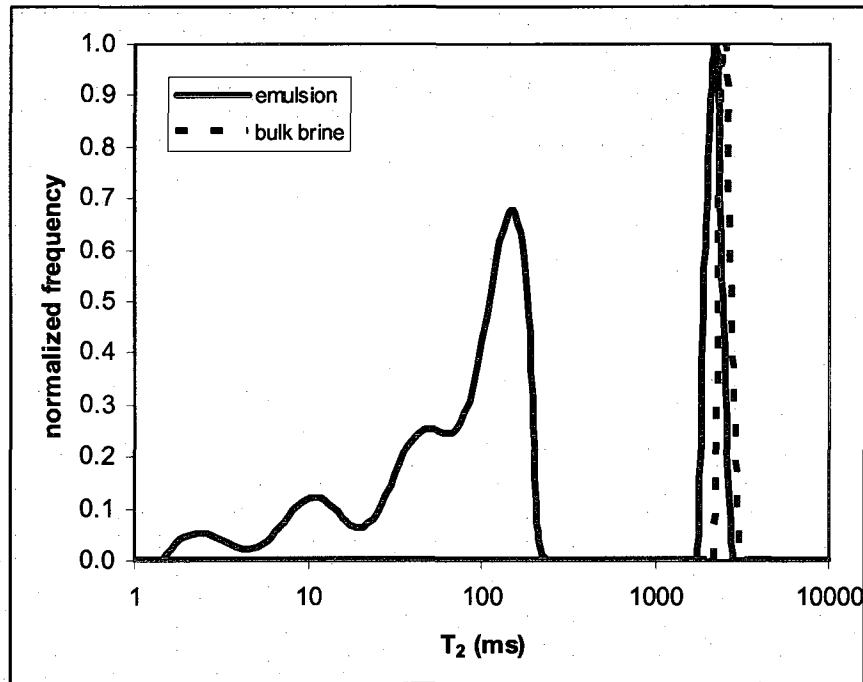


**Figure 3.6:**  $T_2$  distribution of an emulsion with  $\omega = 1600$  rpm for 10 minutes. Note the proximity of the emulsified brine  $T_2$  distribution to the bulk brine  $T_2$  distribution.

Figure 3.6 shows the overlap of the emulsified brine  $T_2$  distribution and the bulk brine  $T_2$  distribution. Figure 3.7 shows the drop size distribution that was obtained by using the emulsified brine  $T_2$  distribution in conjunction with Equation 3.1.

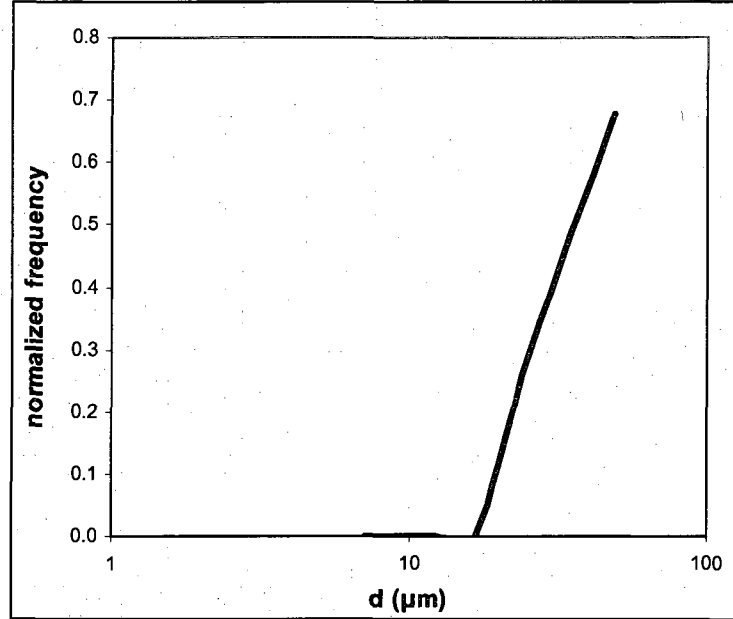


**Figure 3.7:** Drop size distribution obtained from transverse relaxation data. Note the increase in the width of the distribution that was caused by the approach of the emulsified brine  $T_2$  distribution to the bulk brine  $T_2$  distribution.

The drop size distribution in Figure 3.7 illustrates the error that is introduced when using Equation 3.1 if the  $T_2$  distribution of the emulsified brine is close to the bulk brine  $T_2$  distribution. Equation 3.1 assumes that the transverse relaxation distribution of the bulk brine is single valued. Experimentally, the bulk brine exhibits a finite range of  $T_2$  values. Therefore, the emulsified brine can overlap the bulk brine distribution, thus causing a significant increase in the uncertainty of the drop size distribution. In addition, Equation 3.1 requires the use of the surface relaxivity, which was obtained from Equation 3.6.

$$\rho = \frac{d_v}{6} \left( \frac{1}{T_{2,lm}} - \frac{1}{T_{2,bulk}} \right) \quad (3.6)$$

The volume weighted mean diameter,  $d_v$ , and the log mean  $T_2$  value of the emulsified brine,  $T_{2,lm}$ , were obtained from a PFG-DE measurement. For this brine/crude oil system, the surface relaxivity was  $0.5 \mu\text{m/s}$ .

The PFG-DE and PFG techniques were performed on the same emulsion. With the input values of  $T_{2,bulk} = 2.5 \text{ s}$ ,  $\rho = 0.5 \mu\text{m/s}$ , and  $\Delta/T_{2,DP} = 0.3$ , the following parameters were calculated, as shown in Table 3.1:  $\Delta = 598 \text{ ms}$ ,  $\delta = 5.7 \text{ ms}$ , and  $g = 1 - 10 \text{ G/cm}$ . These parameters were sensitive to drop diameters in the range,  $10 - 140 \mu\text{m}$ .

Unlike the CPMG technique, the PFG-DE technique does not rely on the  $T_2$  distribution to generate the drop size distribution. Figure 3.8 contains the two dimensional map produced from the PFG-DE technique.

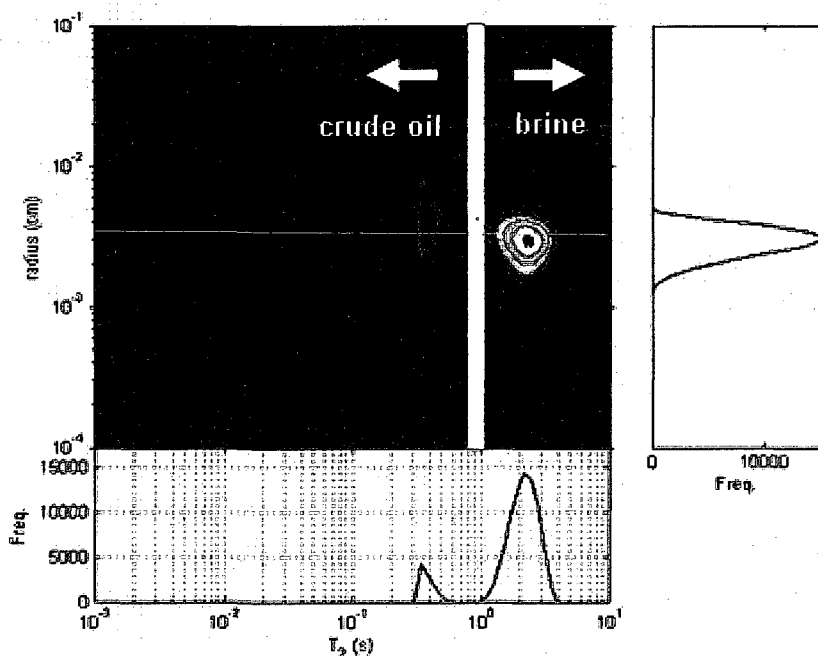


**Figure 3.8:** Two dimensional map produced from the PFG-DE technique after application of the mask. Note the separation of the crude oil A and brine in terms of transverse relaxation. Only brine contributes to the drop size distribution.

The emulsified brine and crude oil A contributions are separated with respect to the  $T_2$  distribution, thereby making the drop size distribution only dependent on the brine contribution. In addition, the  $T_2$  relaxation contribution from the crude oil has been minimized as a result of the choice of the gradient spacing. The PFG technique was performed to compare to the drop size distribution obtained from the PFG-DE technique, and the results are shown in Figure 3.9.

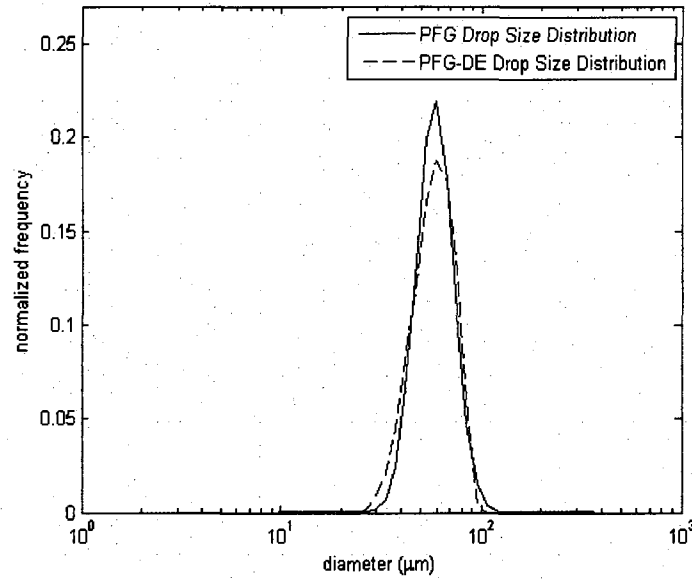


**Figure 3.9:** Comparison of drop size distributions obtained from the PFG-DE and PFG techniques. The drop size distribution from the PFG-DE technique given by the mean and one standard deviation on either side of the mean (45, 59, 72)  $\mu\text{m}$  agrees well with the traditional PFG technique, (47, 58, 72)  $\mu\text{m}$ .

The drop size distributions shown in Figure 3.9 are summarized by quantifying the volume weighted mean diameter,  $d_v$ , and one standard deviation on either side of the volume weighted mean diameter,  $(d_v - \sigma, d_v, d_v + \sigma)$ .

Because the PFG-DE technique yields a discrete drop size distribution and the PFG technique yields a continuous probability density function, a relationship must be

established between the two techniques to graphically compare the two techniques. The cumulative distribution of the PFG-DE technique is written according to Equation 3.7.

$$P(d_i) = \sum_{j=1}^{j=i} f_j \quad (3.7)$$

The normalized frequency obtained from the PFG-DE technique is given by  $f_j$ . Because the probability density function for the PFG technique is assumed to be lognormal with equal increments of the logarithm of the diameter, the discrete form of the cumulative distribution for the PFG technique can be written according to Equation 3.8.

$$P(d_i) = \sum_{j=1}^{j=i} p(d_j) d_j \Delta(\log(d_j)) \quad (3.8)$$

The probability density function for the PFG technique is denoted by  $p(d_i)$ . Unlike the CPMG technique as shown in Figure 3.7, the PFG-DE and PFG techniques have the ability to resolve the drop size distribution when the  $T_2$  distribution of the emulsion overlaps the bulk brine  $T_2$  distribution.

### 3.3.2 Emulsified brine $T_2$ distribution overlaps the bulk crude oil $T_2$ distribution (experiment # 2, crude oil B)

If the  $T_2$  distribution of the emulsified brine overlaps the  $T_2$  distribution of the crude oil in the emulsion, the transverse relaxation data cannot be used to obtain the drop size distribution of the emulsion. An emulsion was prepared by combining 5 mL of brine with 20 mL of crude oil B. The emulsion was sheared for ten minutes with  $\omega = 4000$  rpm. Figure 3.10 shows the overlap of the emulsified brine and crude oil  $T_2$  distributions.

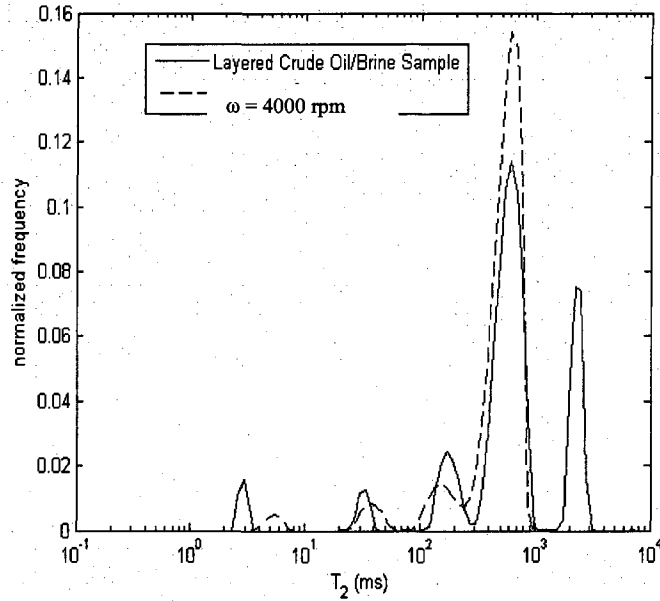


**Figure 3.10:** Overlap of emulsion and crude oil B  $T_2$  distributions.

The solid curve in Figure 3.10 is the  $T_2$  distribution of the layered crude oil B/brine sample, and the dashed curve is the  $T_2$  distribution of the emulsion. Because the emulsified brine and crude oil B  $T_2$  distributions are not separable, Equation 3.1 cannot be used to calculate the drop size distribution.

The parameters for the PFG-DE technique were calculated based on ( $T_{2,bulk} = 2.5$  s,  $\rho = 0.3$   $\mu\text{m/s}$ , and  $\Delta/T_2 = 0.3$ ), and the values were:  $\Delta = 552$  ms,  $\delta = 28$  ms, and  $g = 1 - 13$  G/cm, as shown in Table 3.1. The parameters were sensitive to drop diameters in the range, 5 – 60  $\mu\text{m}$ . The two dimensional map obtained from the PFG-DE technique after applying the masking technique is shown in Figure 3.11.

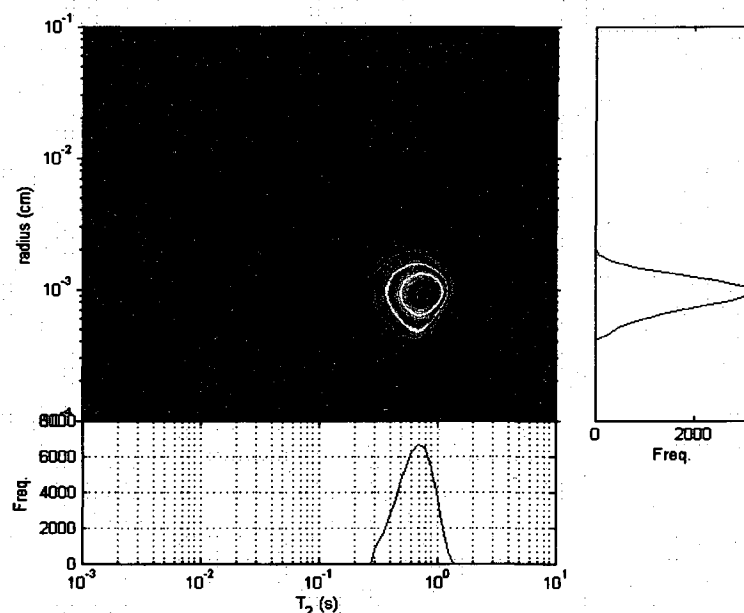


**Figure 3.11:** Two dimensional map of brine-in-crude-oil-B emulsion after masking. The emulsified brine and crude oil B  $T_2$  distributions overlap, but the crude oil B does not contribute to the drop size distribution because the crude oil B signal attenuated significantly.

Figure 3.11 shows that the drop size distribution of the brine phase was extracted using the PFG-DE technique even though the  $T_2$  distributions of the emulsified brine and crude oil B overlap. The lack of contribution of the crude oil B to the drop size distribution is evident when considering the attenuation of the emulsion as shown in Figure 3.12.

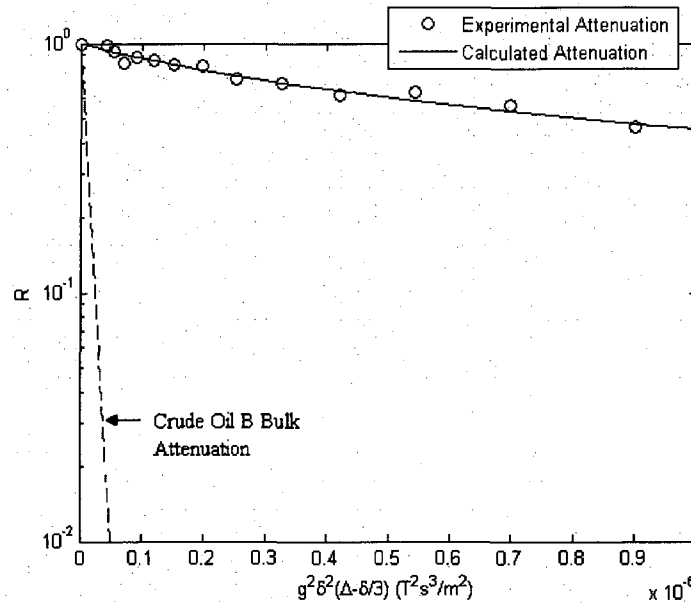


**Figure 3.12:** Experimental and predicted attenuation for the Experiment # 2 brine-in-crude-oil-B emulsion ( $\Delta = 552$  ms,  $\delta = 28$  ms, and  $g = 1 - 13$  G/cm). Note that the crude oil B does not contribute to the attenuation of the signal of the emulsion, thereby facilitating the separation of the crude oil B and brine contributions.

Figure 3.12 shows that the crude oil B does not significantly contribute to the attenuation of the signal of the emulsion based on Equation 2.20. The signal of the crude oil B is negligible after the second gradient pulse; therefore, the emulsified brine and crude oil B contributions can be separated. As shown by Peña, if the signal from the continuous phase is diminished, only the brine signal contributes to the determination of the drop size distribution.<sup>4</sup> Though the oil signal does not have to be eliminated to use Equation 2.23, the effective diffusivities of the brine and crude oil must be separable to effectively characterize the emulsified brine drop size distribution.

The PFG measurement was performed using the same parameters as those used for the PFG-DE measurement, and the comparison of the drop size distributions is shown in Figure 3.13.



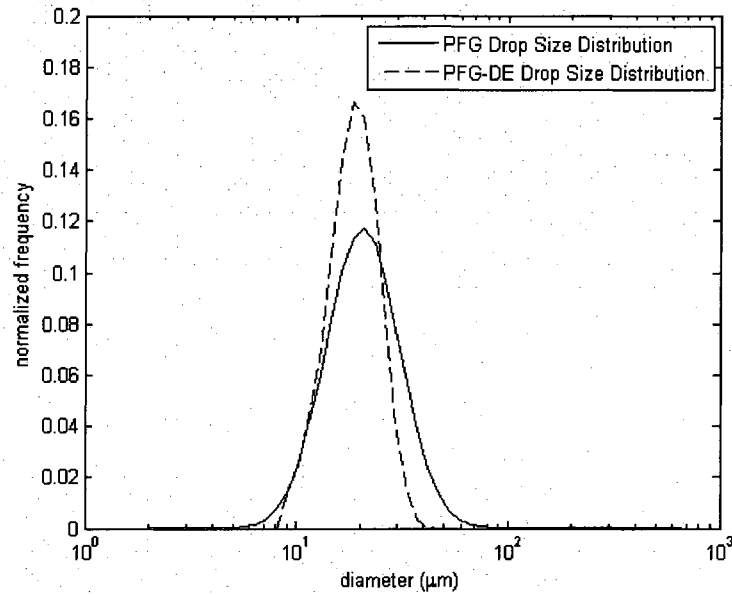


**Figure 3.13:** Comparison of drop size distributions obtained from the PFG-DE and PFG techniques. The drop size distribution from the PFG-DE technique, (14, 19, 24)  $\mu\text{m}$ , agrees well with the traditional PFG technique (14, 21, 31)  $\mu\text{m}$ .

Table 3.4 contains a summary of the results for the two previously described experiments.

**Table 3.4:** Summary of results for the unimodal brine-in-crude-oil emulsions.

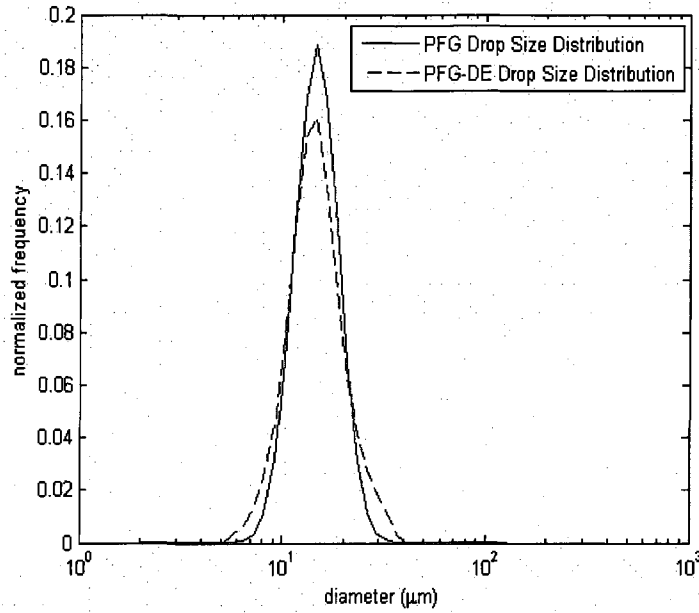
experiment #	method	$\omega$ (rpm)	$-\sigma$	$d_v$	$+\sigma$
1	PFG-DE	1600	45	59	72
1	PFG	1600	47	58	72
2	PFG-DE	4000	14	19	24
2	PFG	4000	14	21	31

### 3.3.3 Bimodal drop size distribution (experiment # 3, crude oil A)

The PFG-DE technique is particularly useful for determining the drop size distribution when the emulsion contains a bimodal drop size distribution. A bimodal drop size distribution was prepared by combining two independently formed emulsions. One emulsion was prepared by shearing 10 mL of brine with 40 mL of crude oil A. The shearing duration was 10 minutes with  $\omega = 2875$  rpm. An independent emulsion

consisting of 10 mL of brine and 40 mL of crude oil A was formed with  $\omega = 1600$  rpm and shearing duration equal to 10 minutes. The PFG-DE and PFG measurements were performed on both of the independent emulsions. From each independent emulsion, 25 mL was removed and combined into one glass sample vessel to form a bimodal drop size distribution. The PFG-DE measurement was performed on the combined emulsion.

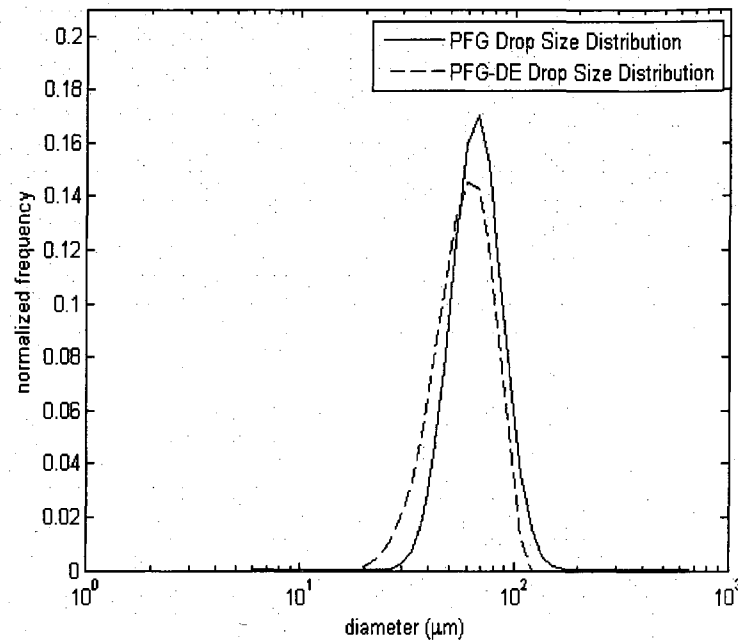
By applying two different shear rates, it was expected that two different populations of drops would form. Therefore, two different parameter sets were constructed to characterize the two different drop size distributions. With  $\omega = 2875$  rpm, parameters were calculated with maximum sensitivity to drops with diameters equal to 10  $\mu\text{m}$  in the range 5 – 70  $\mu\text{m}$ . To characterize this range of diameters, the following parameters were calculated based on  $T_{2,bulk} = 2.5$  s,  $\rho = 0.5$   $\mu\text{m/s}$ , and  $\Delta/T_2 = 0.3$ :  $\Delta = 470$  ms,  $\delta = 28$  ms,  $g = 1 - 15$  G/cm. The PFG technique was also used to measure the drop size distribution of the emulsion, and the comparison is shown in Figure 3.14.



**Figure 3.14:** Comparison of drop size distributions with  $\omega = 2875$  rpm. The PFG-DE technique yielded a drop size distribution, (10, 15, 20)  $\mu\text{m}$ , that agreed with the PFG technique, (11, 15, 19)  $\mu\text{m}$ .

Figure 3.14 shows the agreement that was achieved between the PFG-DE technique and the PFG technique with  $\omega = 2875$ .

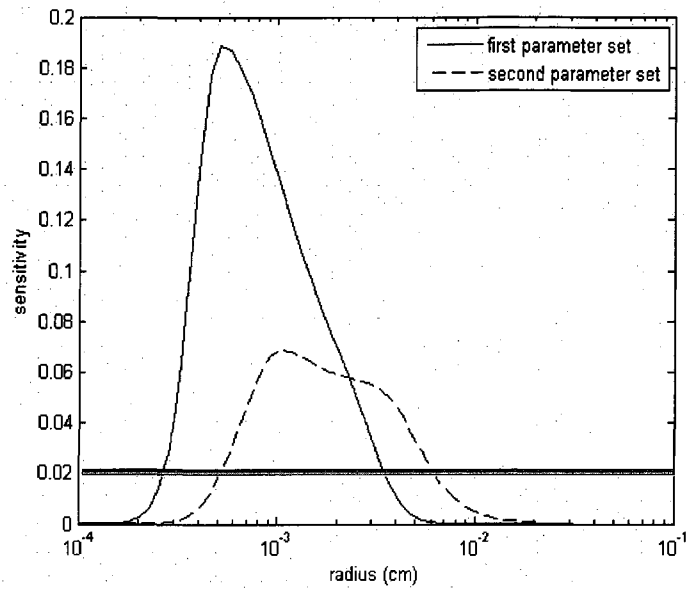
With  $\omega = 1600$  rpm, parameters were calculated with maximum sensitivity to drops with diameters equal to 20  $\mu\text{m}$  in the range 10 – 140  $\mu\text{m}$ . To characterize this range of diameters, the following parameters were calculated based on  $T_{2,bulk} = 2.5$  s,  $\rho = 0.5$   $\mu\text{m/s}$ , and  $\Delta/T_2 = 0.3$ :  $\Delta = 598$  ms,  $\delta = 5.7$  ms,  $g = 1 - 10$  G/cm. The PFG technique was also used to measure the drop size distribution of the emulsion, and the comparison is shown in Figure 3.15.



**Figure 3.15:** Comparison of drop size distributions with  $\omega = 1600$  rpm. The PFG-DE technique yielded a drop size distribution, (42, 60, 78)  $\mu\text{m}$ , that agreed with the PFG technique, (50, 66, 87)  $\mu\text{m}$ .

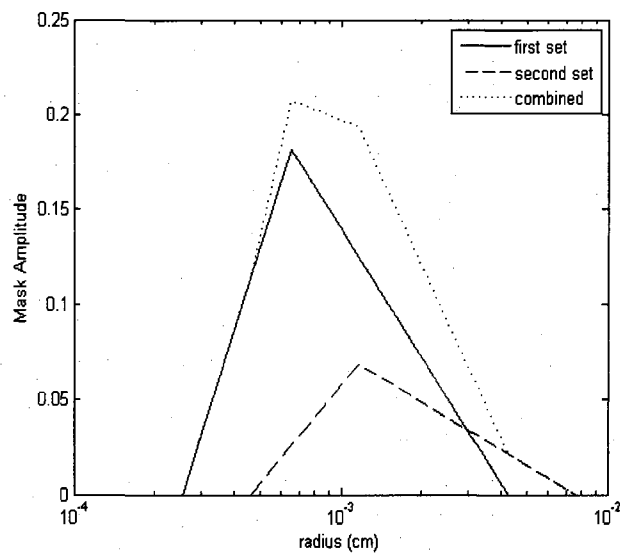
Figure 3.15 shows the agreement that was achieved between the PFG-DE and PFG techniques with  $\omega = 1600$  rpm.

An emulsion with a bimodal drop size distribution was formed by combining 25 mL of the emulsion with  $\omega = 2875$  rpm, with 25 mL of the emulsion with  $\omega = 1600$  rpm. The PFG-DE measurement of the bimodal emulsion consisted of two complete parameter sets: [ $\Delta = 470$  ms,  $\delta = 28$  ms,  $g = 1 - 15$  G/cm] and [ $\Delta = 598$  ms,  $\delta = 5.7$  ms,  $g = 1 - 10$  G/cm]. The masking technique developed by Flaum was used to investigate the range of sizes of the bimodal distribution as described in Section 3.2.2.<sup>46</sup> The sensitivity for each parameter set is given in Figure 3.16.



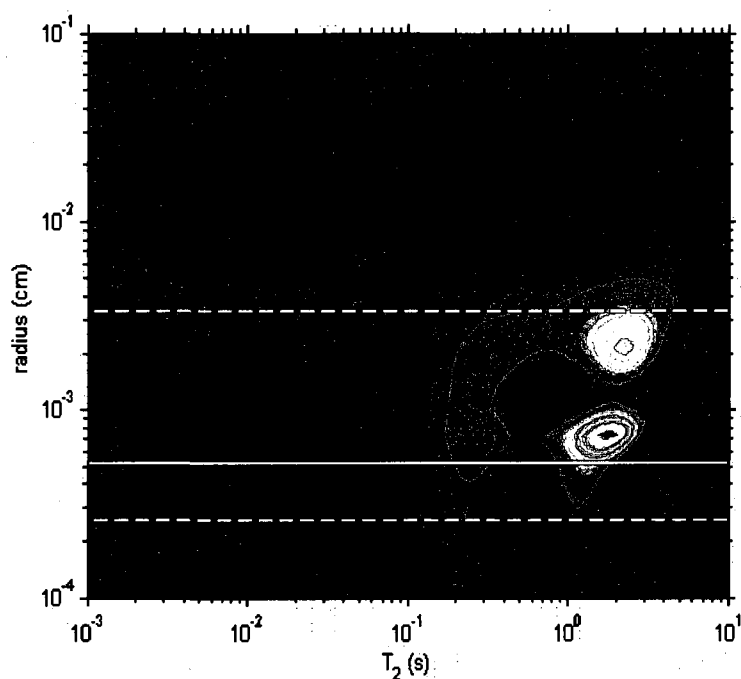
**Figure 3.16:** Sensitivity of the two parameter sets with the noise cutoff equal to 0.02.

The drop size masks were determined based on the sensitivity of each parameter set and the noise cutoff of the measurement which was 0.02 for this experiment.



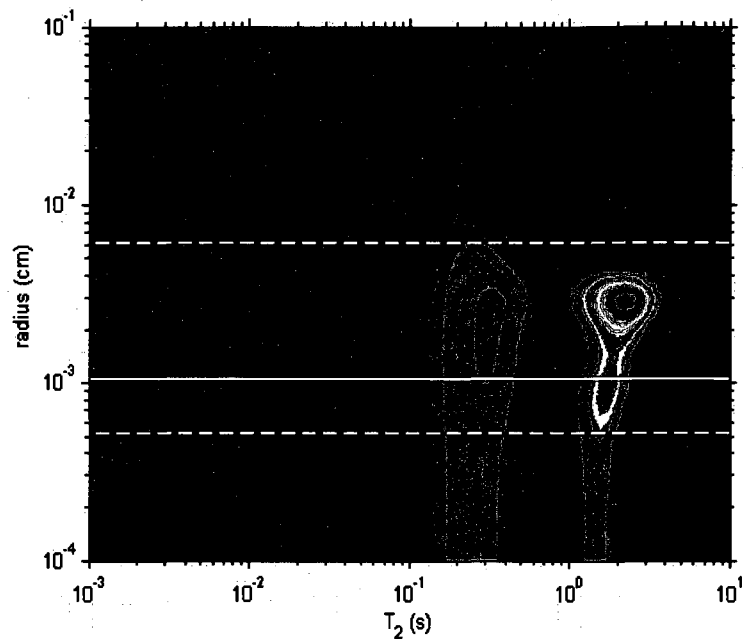
**Figure 3.17:** Drop size masks for each parameter set.

Figure 3.18 shows the limits of the sensitivity of the first parameter set.



**Figure 3.18:** Two dimensional results for the first parameter set. The most sensitive drop size is indicated by the solid line while the limits of the sensitivity of the measurement are indicated by the dashed lines. Note that the population of smaller drops exists in the sensitive region.

The solid line indicates the most sensitive drop size of the measurement, and the dashed lines indicate the limits of the sensitivity of the measurement. Similarly, the sensitivity of the second parameter set is shown in Figure 3.19.



**Figure 3.19:** Two dimensional results for the second parameter set. Note that the larger population of drop sizes is present in the sensitive region.

The second parameter set is sensitive to the larger population of drop sizes as shown in Figure 3.19.

In addition to masking the measurement according to the drop size, the masking procedure also applies to the transverse relaxation distribution.

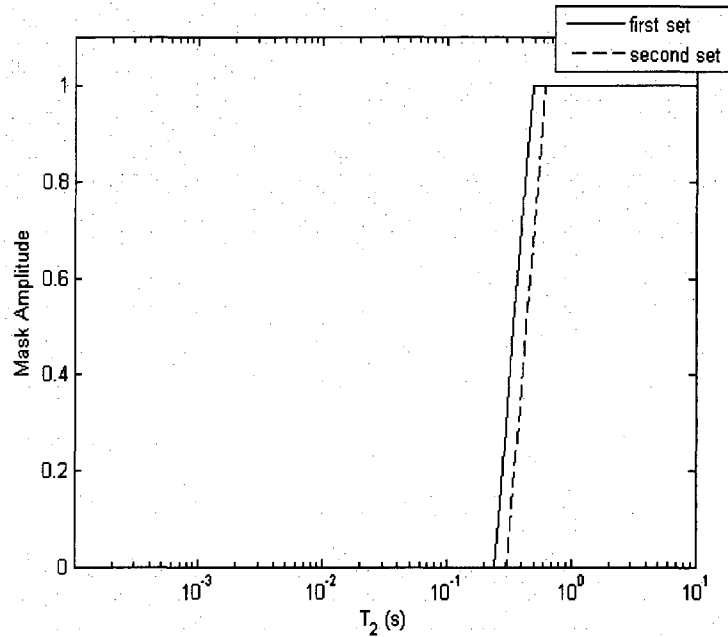


**Figure 3.20:** Transverse relaxation masks for the two parameter sets.

For this example, masking the transverse relaxation merely diminishes the transverse relaxation contribution of the crude oil while the emulsified brine contribution is unaffected. Figure 3.21 shows the final result after masking both drop size and transverse relaxation.



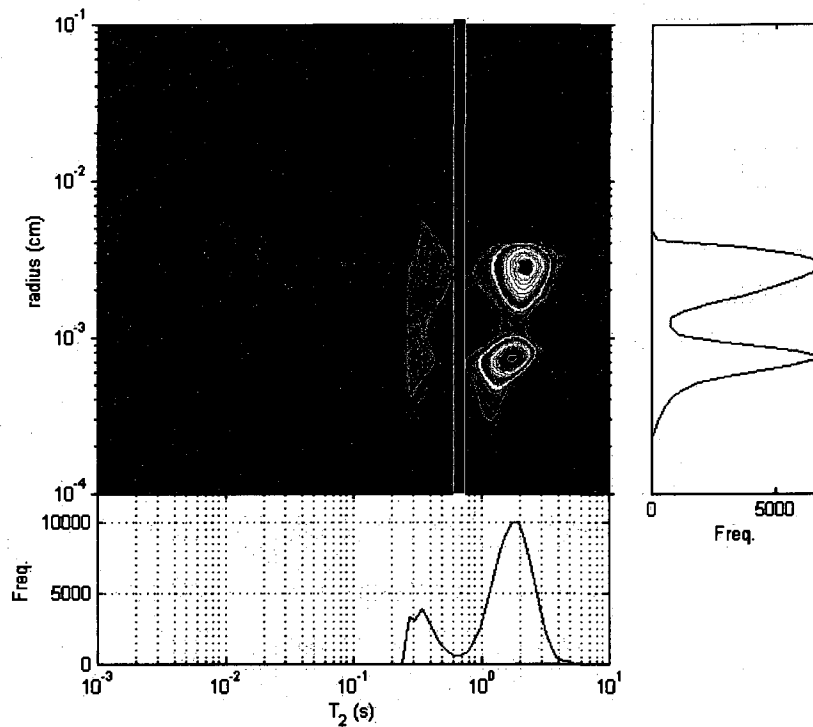


**Figure 3.21:** Two dimensional map of the bimodal drop size distribution after masking both drop size and transverse relaxation. The brine contribution to the drop size distribution was isolated according to the separation of the  $T_2$  distributions.

The crude oil A and brine contributions were isolated according to the separation in terms of the  $T_2$  distributions, and the resulting bimodal drop size distribution is given in Figure 3.22.

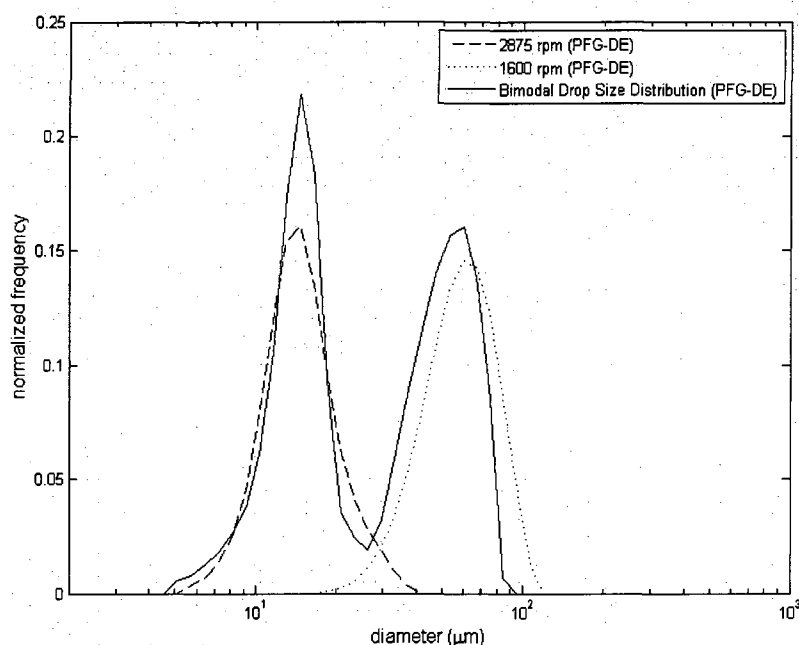


**Figure 3.22:** Comparison of unimodal drop size distributions with the bimodal drop size distribution obtained using the PFG-DE technique.

Figure 3.22 illustrates the ability of the PFG-DE technique to resolve the bimodal drop size distribution. The independently measured unimodal drop size distributions of each emulsion are plotted in conjunction with the bimodal drop size distribution. Figure 3.22 shows that the first population of sizes in the bimodal distribution, (11, 14, 17)  $\mu\text{m}$ , agrees with the PFG-DE measurement of the corresponding unimodal drop size distribution, (10, 15, 20)  $\mu\text{m}$ . In addition, the second population of drop sizes in the bimodal distribution, (39, 52, 65)  $\mu\text{m}$ , also agrees with the PFG-DE measurement of the corresponding unimodal distribution, (42, 60, 78)  $\mu\text{m}$ . These results show that the PFG-DE technique has the ability to resolve a bimodal drop size distribution which is in agreement with the independent, unimodal drop size distributions.

### 3.4 Conclusions

This work showed that the PFG-DE technique measures drop size distributions of emulsions in different physical situations. In addition, the parameter selection algorithm developed by Flaum<sup>46</sup> facilitates accurate measurements of drop size distributions of emulsions. The results from the PFG-DE technique have been shown to agree with the traditional PFG technique. The PFG-DE technique also has the ability to resolve more complicated drop size distributions such as bimodal drop size distributions. In general, the PFG-DE technique is useful because it provides both transverse relaxation and drop size distributions simultaneously, and it is not constrained by an assumed shape of the drop size distribution.

### 3.5 Notation

$D_{DP}$	diffusivity of dispersed phase (cm <sup>2</sup> /s)
$d_i$	drop size of the $i^{\text{th}}$ bin ( $\mu\text{m}$ )
$d_{\text{optimal}}$	optimal diameter for a given parameter set ( $\mu\text{m}$ )
$d_{\text{range}}$	range of drop diameters ( $\mu\text{m}$ )
$d_v$	volume weighted mean diameter ( $\mu\text{m}$ )
$f_j$	normalized frequency of the PFG-DE drop size distributions
$g$	gradient strength (G/cm)
$g_{01}$	gradient resulting in 1% of the signal remaining (G/cm)
$g_{99}$	gradient resulting in 99% of the signal remaining (G/cm)
$N_{\text{grad}}$	number of gradients used in a PFG-DE measurement
$P(d_i)$	cumulative probability distribution function
$r$	droplet radius ( $\mu\text{m}$ )
$r_g$	radius of outer glass cylinder (mm)
$r_T$	radius of inner Torlon cylinder (mm)
$T_{2,\text{bulk}}$	bulk relaxation of dispersed phase (ms)
$T_{2,DP,i}$	transverse relaxation of the $i^{\text{th}}$ bin (ms)
$\rho$	surface relaxivity ( $\mu\text{m/s}$ )
$\Delta$	time between gradient pulses (ms)
$\delta$	gradient pulse duration (ms)
$\delta_{\text{min}}$	minimum gradient duration (ms)
$\sigma_{\text{noise}}$	standard deviation of noise
$\omega$	inner cylinder rotational speed (rpm)
$\sigma$	standard deviation of lognormal drop size distribution ( $\mu\text{m}$ )

## **Chapter 4: Analysis of Formation of Water-in-Oil Emulsions**

### **4.1 Introduction**

A large body of literature exists regarding emulsion formation for dilute systems in the absence of surfactants.<sup>68, 69</sup> However, a paucity of data exists regarding emulsion formation of concentrated emulsions, particularly for opaque systems such as crude oil emulsions.<sup>8, 70</sup> These systems are particularly difficult to investigate with traditional methods such as microscopy and light scattering. This work employs NMR to provide quantitative drop size information for emulsified systems because NMR considers the entire emulsion and is not constrained by the optical properties of the emulsions.<sup>4</sup>

Guido and Villone expressed the importance of understanding single drop deformation by stating the following: "The dynamics of an isolated sheared drop can be regarded as a sort of elementary event, which can provide some insight into the complex rheological behavior of a flowing dispersion of drops."<sup>71</sup> G.I. Taylor pioneered the initial work on single drop break-up of a Newtonian drop in a Newtonian continuous phase.<sup>72-74</sup> According to H.A. Stone, "many of the important ideas necessary for understanding drop deformation can be traced to three articles by G.I. Taylor."<sup>69</sup> The first of Taylor's legendary papers involved predicting the largest size of a drop in a given flow field that would not burst. Starting with Einstein's work on the viscosity of a fluid which contains solid, spherical particles, Taylor proceeded to extend this theory to emulsions. Thus, he derived an expression for the maximum drop radius that could be achieved in a simple shear field.<sup>72</sup>

$$r_{\max} = \frac{2 \sigma (\mu_{DP} + \mu_{CP})}{\alpha \mu_{CP} \left( \frac{19}{4} \mu_{DP} + 4 \mu_{CP} \right)} \quad (4.1)$$

The viscosity of the dispersed phase is  $\mu_{DP}$ , and the viscosity of the continuous phase is  $\mu_{CP}$ . The equilibrium interfacial tension between the dispersed and continuous phases is  $\sigma$ . The rate of distortion of the fluid surrounding the drop is  $\alpha$ . Equation 4.1 illustrates the balance between the cohesive action of the interfacial tension, the numerator, and the destructive exterior viscous forces, the denominator.

Taylor's second paper focused on investigating the mechanisms which led to drop deformation in specific flow fields. Taylor investigated both plane hyperbolic flow and simple shear flow. Figure 4.1 shows a drop in simple shear flow.

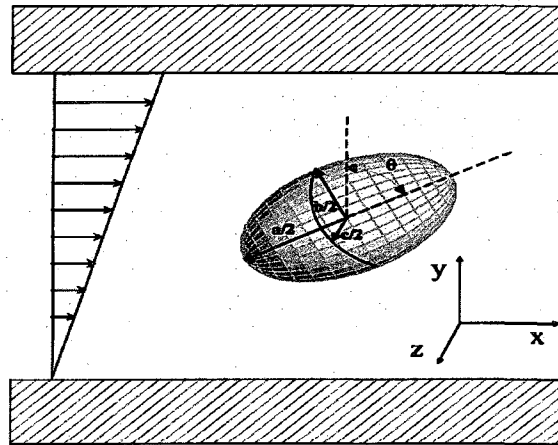


**Figure 4.1:** A drop existing in simple shear flow between two parallel plates (Guido and Villone 1998).<sup>71</sup>

Taylor developed a deformational theory which predicted the deformation of a drop in simple shear flow. In order to formulate his theory, Taylor made the following assumptions:<sup>73, 75</sup>

1. creeping flow around the drop
2. continuity of tangential stress at the interface
3. the interfacial pressure and normal stress difference are equal at the interface

Equation 4.2 shows the deformation parameter,  $D$ .<sup>73</sup>

$$D = \frac{a-b}{a+b} = Ca \frac{19\lambda + 16}{16\lambda + 16} \quad (4.2)$$

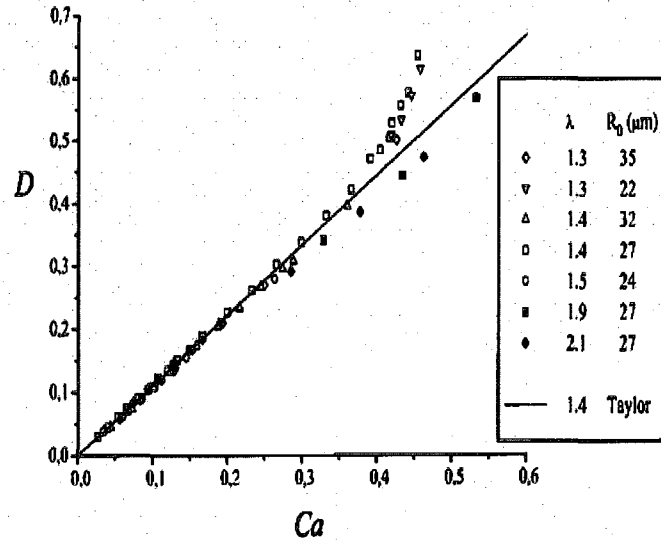
The drop deformation depends linearly on the Capillary number,  $Ca$ , with a slope that is a function of the viscosity ratio between the dispersed and continuous phases,  $\lambda$ .

$$Ca = \frac{\gamma \mu_{CP} r}{\sigma} \quad (4.3)$$

$$\lambda = \frac{\mu_{DP}}{\mu_{CP}} \quad (4.4)$$

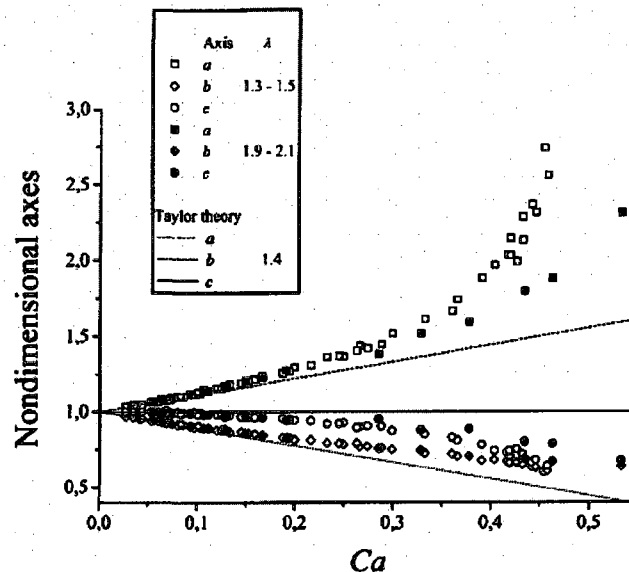
In Equation 4.3,  $\gamma$  is the shear rate applied to the drop and  $r$  is the radius of the undeformed drop. The capillary number is the ratio between the disruptive viscous shear stresses from the continuous fluid,  $\gamma \mu_{CP}$ , and the restoring LaPlace pressure of the drop,  $\frac{\sigma}{r}$ . Therefore, the capillary number compares the strength of the force required to disrupt the drop with that which is required to maintain the spherical shape of the drop.

Taylor's linear relationship to predict drop deformation as a function of Capillary number agrees with experimental data.<sup>71</sup>



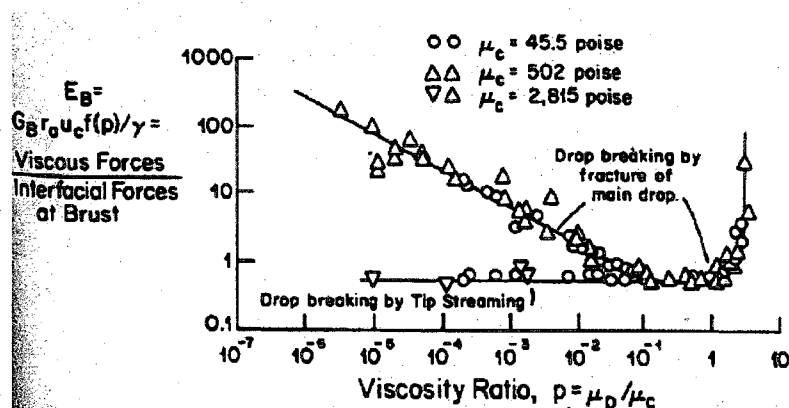
**Figure 4.2:** Experimental results for the drop deformation of a single drop undergoing simple shear. The experimental results match the theory proposed by Taylor at low Capillary numbers (Guido and Villone 1998).<sup>71</sup>

Figure 4.2 shows the excellent agreement between the experimental results found by Guido and Villone and the deformation theory proposed by Taylor for deformation of a single drop in simple shear with low Capillary numbers. Additional experimental results reported by Rumscheidt and Mason, Torza et al., and Grace correspond to the results published by Guido and Villone and the theory proposed by Taylor.<sup>71, 73, 76, 77</sup> These authors show that the experimental results agree with Taylor's theory at low Capillary numbers, but deviation from the theory occurs as the Capillary number increases. Guido and Villone also evaluated the three dimensional deformation of an isolated drop in simple shear flow produced in a parallel plate apparatus.<sup>71</sup> The results agreed with Taylor's theory at low Capillary numbers. However, as the Capillary number increased, Taylor's theory did not accurately predict the deformation of the drops.



**Figure 4.3:** Comparison of experimental data to Taylor's deformation theory. The three axes,  $a$ ,  $b$ , and  $c$ , are normalized with respect to the initial drop diameter (Guido and Villone 1997).<sup>71</sup>

Based on Taylor's work, Grace performed experiments to determine the critical Capillary number which leads to droplet breakup as a function of viscosity ratio. Grace used simple shear flow in his experiments.



**Figure 4.4:** Dependence of critical Capillary number on viscosity ratio (Grace 1982).<sup>78</sup>

The horizontal line refers to tip streaming in which small drops form at the ends of the main drop while the curve represents drop breakup as a result of drop fracture. These data provided by Grace indicate that drop breakup becomes difficult at either extreme of



the viscosity ratio, and breakup is nearly impossible when the viscosity ratio exceeds 3.5.<sup>78</sup>

Subsequent researchers attempted to provide theoretical validation to Grace's experimental results. Figure 4.5 displays the relationship between the critical Capillary number and viscosity ratio for simple shear flow.

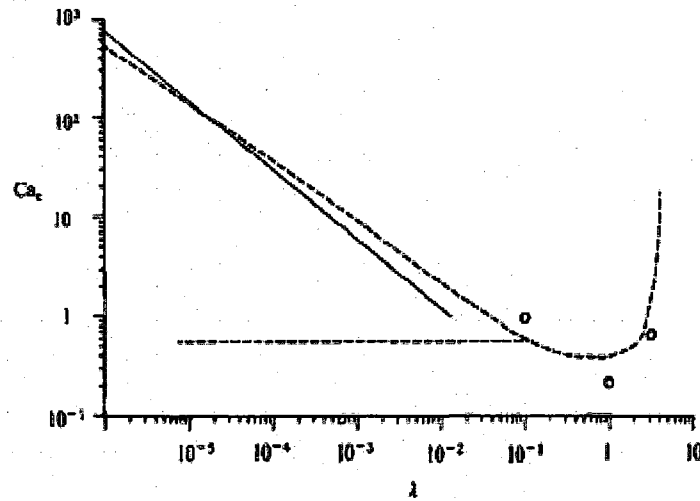


**Figure 4.5:** Critical Capillary number as a function of viscosity ratio for simple shear flow. The hatched lines are experimental results from Grace.<sup>78</sup> The solid line is asymptotic theory for  $\lambda$  going to zero by Hinch and Acrivos.<sup>79</sup> The open circles are theoretical predictions from Barthes-Biesel and Acrivos<sup>80</sup> (Rallison 1984).<sup>68</sup>

The hatched lines are experimental results obtained by Grace.<sup>78</sup> The solid line was obtained by Hinch and Acrivos based on theory developed for low dispersed phase viscosities ( $\lambda \rightarrow 0$ ).<sup>81</sup> This theory, referred to as slender body theory, states that as the dispersed phase viscosity approaches zero, the drop assumes a slender shape before breakup. The critical Capillary number in this region of viscosity ratio obeys Equation 4.5.<sup>81</sup>

$$Ca_c = 0.0541 \lambda^{\frac{2}{3}} \quad (4.5)$$

This prediction agrees with Grace's experimental results for low values of the dispersed phase viscosity. For higher values of the dispersed phase viscosity, Barthes-Biesel and Acrivos developed the theory for drop breakup by defining a deformation parameter and applying a linear stability analysis to the solution of the creeping flow equations. The results are represented by open circles in Figure 4.5.<sup>80</sup> The authors admit that "the theoretical results are generally found to be of acceptable accuracy although, in some cases, the agreement is only qualitative."<sup>80</sup>

When discussing the application of information about isolated drop break-up toward understanding the mechanisms of concentrated drop break-up in flow, H. Stone said the following, "One important and challenging problem which awaits an adequate solution is to incorporate the basic elements of the research described here into a model of a viscous multiphase flow containing a large number of dispersed droplets, with the goal to predict accurately the drop size distribution."<sup>69</sup> In an attempt to answer this challenge, one recent study performed by Zhao investigated the transient breakup of dilute emulsions (0.1 – 0.2 wt.%) in simple shear flow in the absence of surfactant.<sup>70</sup> Similar to Guido and Villone,<sup>71</sup> Zhao used a parallel plate apparatus to produce shear flow. One of the main focuses of Zhao's work was to understand the drop breakup mechanisms at high values of the Capillary number.<sup>75</sup> Through direct visualization techniques, Zhao compiled his understanding of the drop breakup mechanisms into Figure 4.6.

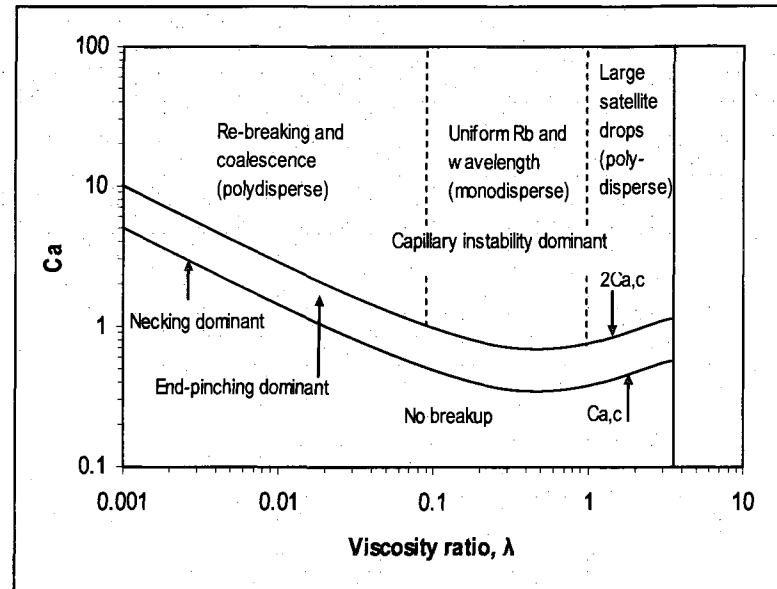


**Figure 4.6:** General drop breakup mechanisms that occur as a function of Capillary number and viscosity ratio (reproduced from Zhao 2007).<sup>70</sup>

Figure 4.6 shows the different regions and type of drop breakup that should be expected given the Capillary number and viscosity ratio. The necking mechanism causes drop breakup when the Capillary number is nearly equal to the critical Capillary number, and two daughter drops form from the original drop. End pinching is the dominant drop breakup mechanism when the Capillary number is in the range,  $Ca_c < Ca < 2 Ca_c$ . When  $Ca > 2 Ca_c$ , the mechanism that governs drop breakup is capillary instability. The mechanism can further be divided into three classes depending on the viscosity ratio. For the range  $\lambda < 0.1$ , “the daughter drops are formed from long wavelength capillary instability and may break again.”<sup>75</sup> Collisions are caused by the drop re-breaking, which leads to further re-breaking or coalescence. The re-breaking mechanism leads to additional collisions and coalescence at low viscosity ratios, as well as polydispersity of the resulting emulsion. This observation of concurrent drop breakup and coalescence was a new addition to the information about drop breakup mechanisms.<sup>75</sup> In the range,

$0.1 < \lambda < 1$ , threads formed from drops with different initial diameters, and the threads ultimately broke with the same diameter. When  $\lambda$  increased to  $1 < \lambda < 3.5$ , the breakup mechanism is similar, but “the satellite drops are substantially larger, resulting in polydisperse emulsions.”<sup>75</sup> Similar to Grace, Zhao observed polydisperse drop size distributions with increasing Capillary number.<sup>75, 78</sup>

Of great industrial importance is the formation of concentrated emulsions in the presence of surfactants. In this context, concentrated refers to emulsions with a water volume fraction greater than 0.1. As stated by Dalmazzone, there is a great need for data regarding emulsion formation of concentrated emulsions in the presence of surfactant: “Consequently, for very concentrated systems where the surfactants and the hydrodynamic conditions are difficult to identify, as in petroleum emulsions, the parameters that play a vital part in the break-up and coalescence mechanisms of the droplets have to be determined. The need to obtain reliable experimental data from perfectly controlled, if not perfectly understood, systems would appear to be a priority.”<sup>8</sup>

This chapter presents experimental data regarding emulsion formation of concentrated emulsions in the presence of surfactant in well defined flow fields. This work employs NMR to measure drop size distributions using the PFG-DE technique. In addition, the flow fields used to create the emulsions are modeled using computational fluid dynamics (CFD) (Fluent 6.4.11, Ansys). These experimental data, combined with the CFD simulations, provide insight about the formation of concentrated emulsions in the presence of surfactants.

## **4.2 Experimental methods**

This work investigated two crude oils and two model oils. The dispersed phase of the emulsions was ASTM brine. Figure 4.7 shows that each crude oil was matched with a model oil of similar viscosity.

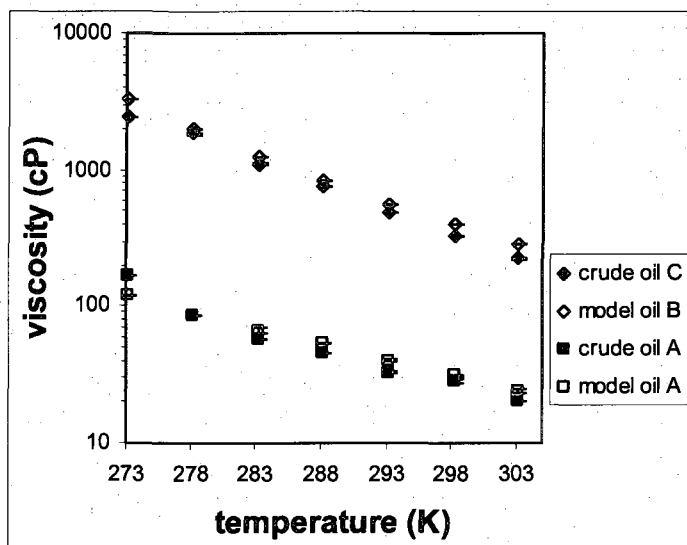


**Figure 4.7:** Viscosity as a function of temperature for the crude and model oils.

The viscosities of each fluid were measured using a Brookfield viscometer. The viscosities of the oils were independent of shear rate over the range of shear rates used in the viscosity measurements. The viscosities of the model oils were measured without surfactant. To quantify the effect of surfactant on the model oil viscosities, the viscosities of the model oils with 4 vol.% Span80 were measured at 278.2 K and 298.2 K, and the results are provided in Table 4.1.

**Table 4.1:** Effect of surfactant on model oil viscosity. Viscosity values are reported with units of cP.

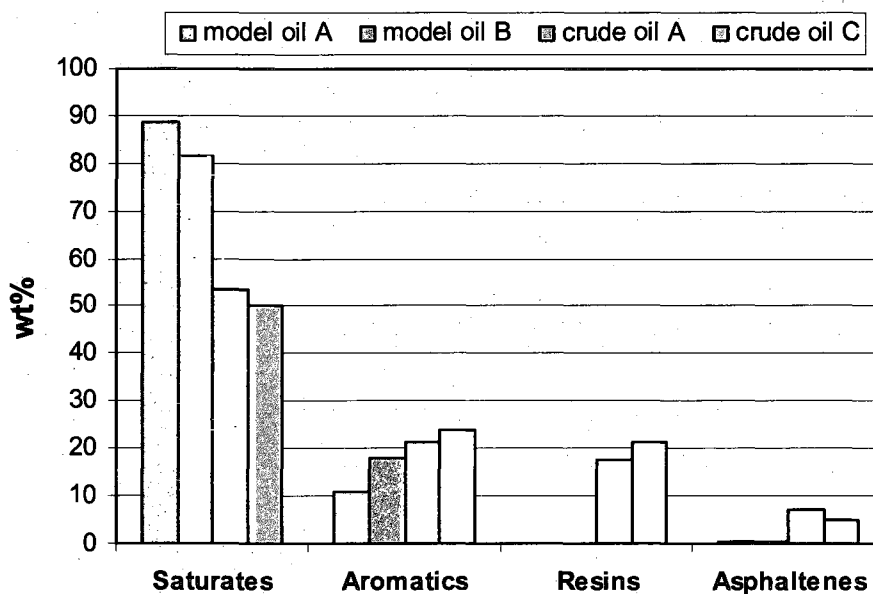
	278.2 K	298.2 K
model oil A with no surfactant	86.0	31.0
model oil A with 4 vol.% Span 80	98.4	34.4
crude oil A	86.1	28.2
model oil B with no surfactant	1982.0	405.0
model oil B with 4 vol.% Span 80	2079.7	412.4
crude oil C	1841.0	323.0

Table 4.2 provides the densities of the fluids, and they were measured by weighing a known volume of the oil on a Sartorius balance.

**Table 4.2:** Densities of the fluids.

Fluid	density (g/mL)
ASTM brine	1.03
Span80	1.00
crude oil A	0.85
model oil A	0.81
crude oil C	0.91
model oil B	0.80

The SARA analysis provides the amount of saturates, aromatics, resins, and asphaltenes in each oil, as shown in Figure 4.8.<sup>82</sup>



**Figure 4.8:** SARA analysis for the 4 oils used in this work (provided by Dr. Jill Buckley's laboratory at New Mexico Tech, 2008).<sup>82</sup>

The SARA analysis indicates that the model oils are essentially free of resins and asphaltenes which are potential stabilizers of water-in-crude-oil emulsions.<sup>6, 23, 83</sup>

Therefore, the interfacial properties of the model oils can be more reliably controlled.

Naturally occurring surfactants stabilized the water-in-crude-oil emulsions. The nonionic surfactant, Span80 (Sigma-Aldrich), stabilized the water-in-model-oil emulsions. In all experiments, the concentration of the oil soluble surfactant was 10 times the needed concentration for monolayer coverage. With the brine fraction equal to 0.2, the concentration of Span80 was 0.356 wt.% in terms of the mass of oil. The surfactant was dissolved in the model oils before the addition of brine.

Interfacial properties provide critical information about emulsion formation.<sup>8</sup>

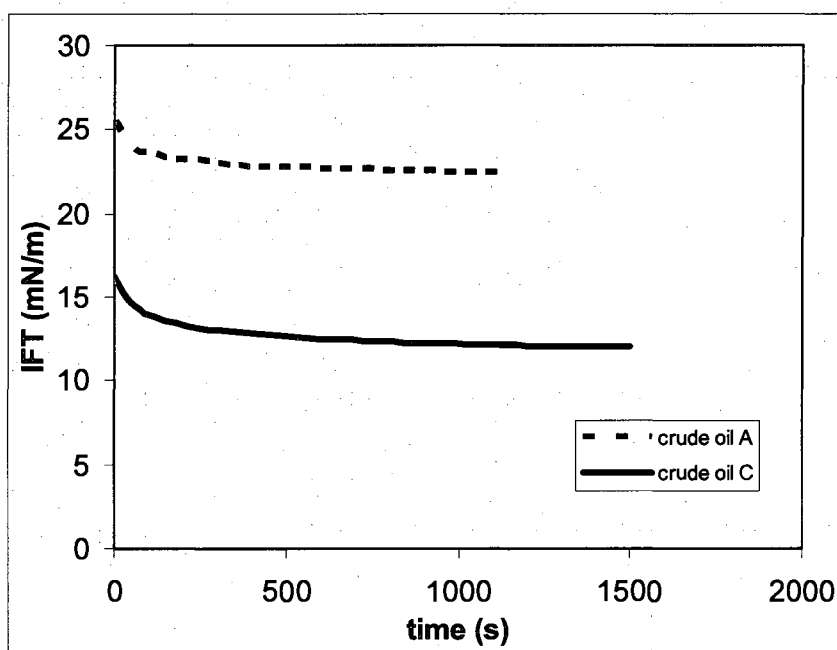


**Figure 4.9:** Equilibrium interfacial tension of the two crude oils.

A KSV CAM 200 instrument performed the interfacial tension measurements using the pendant drop technique. The drop profile and densities of the oil and brine enable the determination of the interfacial tension using the Young-LaPlace equation. The interfacial tension of crude oil C (12 mN/m) was significantly less than crude oil A (22 mN/m) indicating a difference in surface active material. Figure 4.10 shows the equilibrium interfacial tension of the model oils in the presence of surfactant.

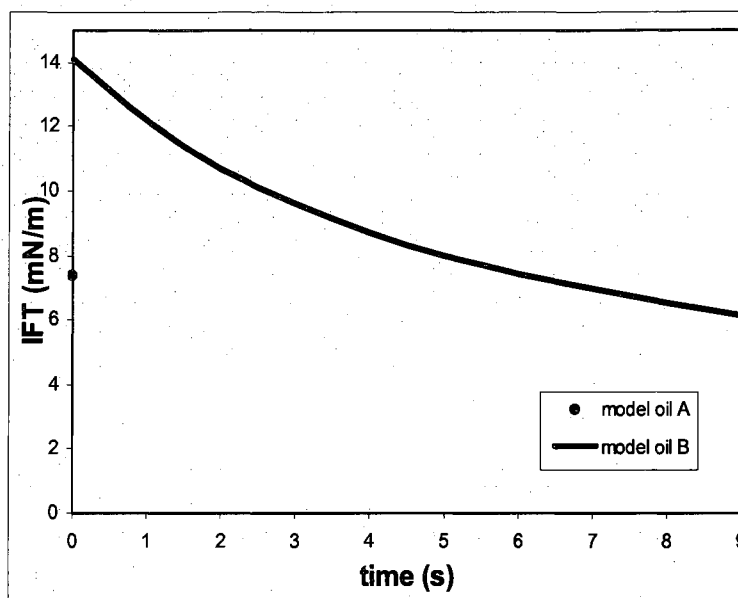


**Figure 4.10:** Equilibrium interfacial tension of the two model oils in the presence of surfactant.

In the presence of surfactant, the interfacial tension of the model oils decreased such that the pendant drop quickly rose off the tip of the needle. These data provide an order of magnitude estimate of 5 mN/m for the interfacial tension.

A Taylor-Couette flow device formed the emulsions in this work. The rotating, inner cylinder was composed of Torlon with radius equal to 19.1 mm. The stationary, outer cylinder was composed of glass with radius equal to 21.6 mm. Taylor-Couette flow leads to both simple and complex flows, as shown in Figure 4.11.



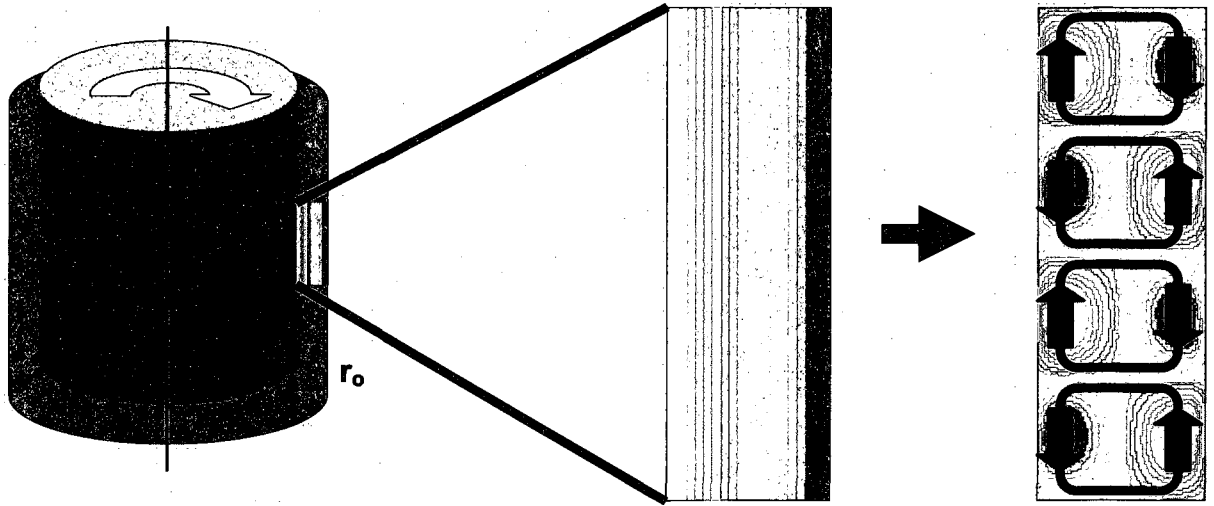


**Figure 4.11:** Taylor-Couette flow leads to the development of secondary flow patterns referred to as Taylor vortices.<sup>84</sup>

The dimensionless Reynolds and Taylor numbers describe the flow in this geometry.<sup>85</sup>

$$\text{Re} = \frac{\rho r_i \Omega (r_o - r_i)}{\mu} \quad (4.6)$$

$$\text{Ta} = \frac{\rho^2 r_i \Omega^2 (r_o - r_i)^3}{\mu^2} \quad (4.7)$$

G.I. Taylor showed that instabilities in the flow field can arise, and these instabilities are primarily governed by the critical Taylor number,  $\text{Ta}_c$ .<sup>86</sup>

$$\text{Ta}_c = \frac{\pi^4 \left(1 + \frac{d}{2 r_i}\right)}{0.0571 \left(1 - 0.652 \frac{d}{r_i}\right) + 0.00056 \left(1 - 0.652 \frac{d}{r_i}\right)^{-1}} \quad (4.8)$$

For the geometry used in this work,  $\text{Ta}_c = 1960$ .

Before the fluids were subjected to shear in the Taylor-Couette device, the inner cylinder was slowly moved up and down 20 times to promote interaction between the brine and oil phases. This action evenly dispersed the brine in the oil in large drops with diameters larger than millimeters. Independent measurements confirmed that this action

resulted in the development of dispersed brine with sizes too large for NMR characterization. The fluids were sheared with this device for 10 minutes in each experiment. For all emulsions, the volume of brine was 12 mL, and the volume of oil was 48 mL yielding a dispersed phase fraction equal to 0.2. The sample height for all samples was 4 cm.

NMR was used as the primary experimental tool in this work. The drop size distributions were obtained using the PFG-DE technique, as described in Chapter 2.<sup>40, 46-48</sup>

### 4.3 Computational methods

This work used the computational fluid dynamics package Fluent 6.4.11 (as marketed by Ansys Inc.). This work used a single phase approximation to simulate the effect of the dispersed phase using the Krieger-Dougherty relation for effective viscosity.<sup>87</sup>

$$\mu_{eff} = \mu_{CP} \left( 1 - \frac{\varphi}{\varphi_{max}} \right)^{-2.5 \varphi_{max}} \quad (4.9)$$

The maximum packing fraction for a face centered cubic lattice is represented by  $\varphi_{max}$ .<sup>15</sup> A multi-phase simulation was compared to a single phase simulation using the same inner cylinder rotational speed (3000 rpm).

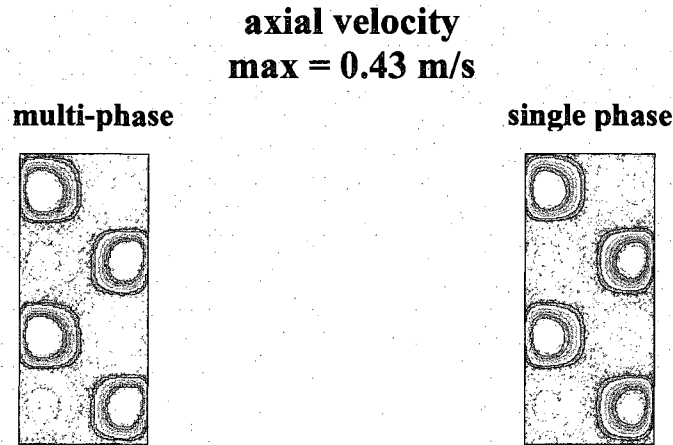


**Figure 4.12:** Comparison of axial velocities for a multi-phase simulation and single phase simulation (max. velocity = 0.43 m/s).

Figure 4.12 shows the similarity between the axial velocities from the multi-phase and single phase simulations. In addition, the multi-phase simulation showed that the water volume fraction was within 1 % of the initial concentration, thereby signifying that no significant depletion or enrichment of water droplets occurred throughout the fluid domain. Therefore, single phase simulations accurately represent the flow fields in this work.

The convergence criterion for the transient simulations was 0.001. The two dimensional mesh consisted of 72721 nodes, and the solver implemented the Green-Gauss node based algorithm. The grid passed grid refinement tests. The flow was modeled as laminar because  $k$ - $\epsilon$  turbulent calculations predicted no turbulence for the range of shear rates used in this work. Tests were performed in 3 dimensions, and it was shown that there were no deviations between 2 and 3 dimensional calculations.

## **4.4 Results**

### **4.4.1 Crude/model oil A systems**

The CFD simulations provide insight about the effect of flow field on emulsion formation. Figure 4.13 shows the swirl and axial velocities for the crude/model oil A systems.



**Figure 4.13:** Swirl and axial velocity profiles for the crude/model oil A systems ( $\mu_{eff} = 36$  cP,  $\omega = 1600$  rpm).

The effective viscosity for the crude/model oil A systems at 303.2 K was 36 cP. The swirl velocity is the component of the velocity coming out of the plane of the page, while the axial velocity is the component of the velocity that exists along the vertical axis.

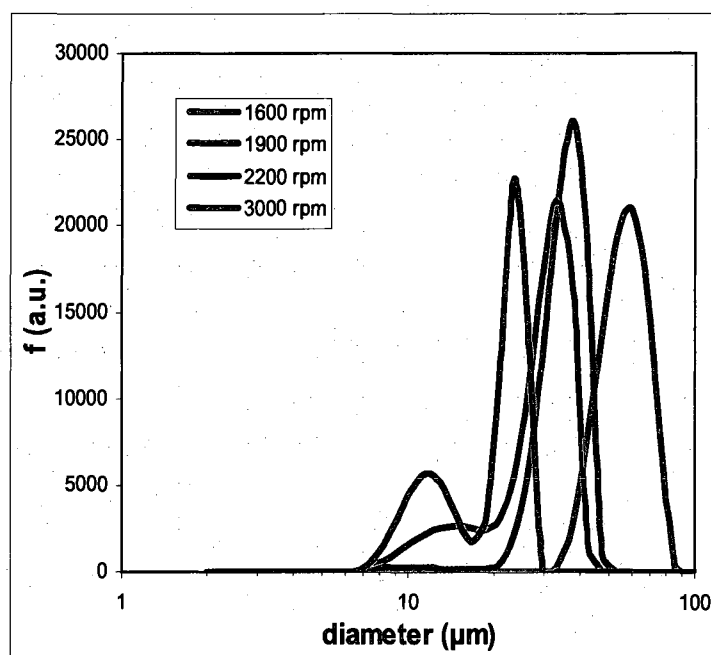
Figure 4.13 shows that at the minimum inner cylinder rotational speed used for the crude/model oil A systems (1600 rpm), secondary flows in the form of Taylor vortices begin to emerge. For these conditions,  $Re = 190$  and  $Ta = 4712$  which exceeds  $Ta_c$  (1960). Using the same Krieger-Dougherty viscosity at the maximum shear (3000 rpm), the presence of Taylor vortices becomes more enhanced.



**Figure 4.14:** Swirl and axial velocity profiles for the crude/model oil A systems ( $\mu_{eff} = 36$  cP,  $\omega = 3000$  rpm).

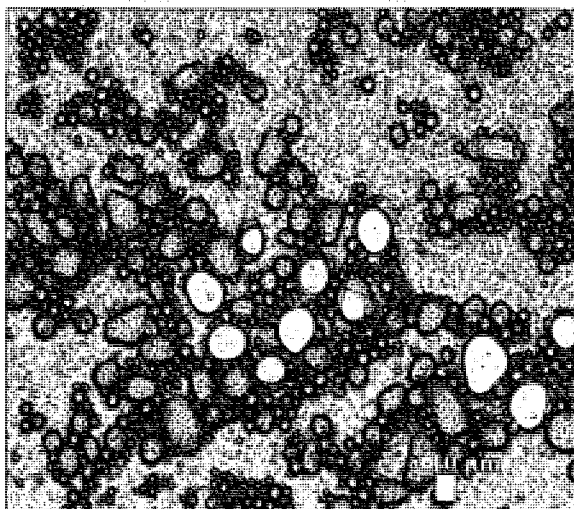
Comparison of Figures 4.13 and 4.14 illustrates the emergence of secondary flows in the form of Taylor vortices for the crude/model oil A systems. For these conditions,  $Re = 356$  and  $Ta = 16565$  which greatly exceeds  $Ta_c$  (1960).

Figure 4.15 shows the brine-in-crude-oil-A drop size distributions as measured with NMR. At least two emulsions were measured at each inner cylinder rotational speed, so Figure 4.15 shows representative drop size distributions at each inner cylinder rotational speed, so Figure 4.15 shows representative drop size distributions at each inner cylinder rotational speed.



**Figure 4.15:** Drop size distributions of the brine-in-crude-oil-A emulsions. Note the increase in multimodality with increasing inner cylinder rotational speed.

Optical microscopy qualitatively supported the NMR results at 3000 rpm.



**Figure 4.16:** Optical microscopy of brine-in-crude-oil-A emulsion at 3000 rpm (objective = 20X).

The photograph in Figure 4.16 was obtained from the brine-in-crude-oil-A emulsion formed at 3000 rpm. A drop of the emulsion was placed on a glass slide and covered with a glass cover slip. The sample was not diluted with solvent.

Figure 4.17 shows the brine-in-model-oil-A drop size distributions.

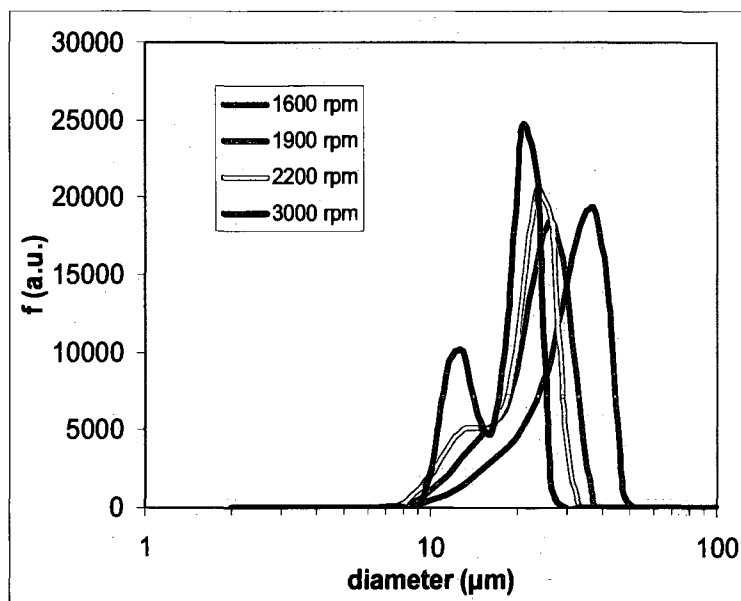


**Figure 4.17:** Drop size distributions of the brine-in-model-oil-A emulsions.

The increase in the multimodal nature of both the crude oil A and model oil A drop size distributions is attributed to the emergence of Taylor vortices in the Taylor-Couette flow device as shown by the CFD simulations. Three dimensional simulations using an inner cylinder rotational speed equal to 3000 rpm showed the existence of a multimodal distribution of shear rates throughout the fluid domain. Particle tracking in the CFD simulation showed that particles can experience different shear environments which could enhance the multimodality of the drop size distribution.

The experimental data were compared to two predictive models. The first model, referred to as the Grace model, is based on Grace's experimental work showing critical capillary number as a function of viscosity ratio.<sup>78</sup>

$$d_{\max} = 2 Ca_c(\lambda) \left( \frac{\mu_{\text{eff}} \gamma}{\sigma} \right)^{-1} \quad (4.10)$$

Grace's model predicts the maximum stable drop diameter in a given flow field. This model predicts single drop breakup in simple shear in the absence of surfactant. The second model, proposed by J.M.H. Janssen, accounts for partially mobile water/oil interfaces, thereby relaying coalescence information during breakup for a multi-drop system.<sup>88</sup>

$$d_{\text{coal}} = 2 \lambda^{\frac{2}{5}} \left( \frac{4}{\sqrt{3}} h_c \right)^{\frac{2}{5}} \left( \frac{\mu_{\text{eff}} \gamma}{\sigma} \right)^{\frac{3}{5}} \quad (4.11)$$

The critical thickness of the film between two approaching drops is given by  $h_c$ .<sup>75</sup>

$$h_c \sim \left( \frac{H r}{8 \pi \sigma} \right)^{\frac{1}{3}} \quad (4.12)$$

$H$  is the Hamaker constant ( $\sim 10^{-20}$  J),  $r$  is the initial drop radius, and  $\sigma$  is the interfacial tension. Equation 4.13 shows the effective shear rate that was used in Equations 4.10 and 4.11.

$$\gamma = \frac{\Omega r_i}{(r_o - r_i)} \quad (4.13)$$

The angular velocity of the inner cylinder is  $\Omega$  and the inner and outer cylinder radii are  $r_i$  and  $r_o$ , respectively.

Both models exhibit power law dependence on the flow group  $\left( \frac{\mu_{eff} \gamma}{\sigma} \right)$ . In addition, both models exclude the effects of surfactant. Figure 4.18 shows the comparison between the experimental mean and maximum diameters and the two predictive models for the brine-in-crude-oil-A system.

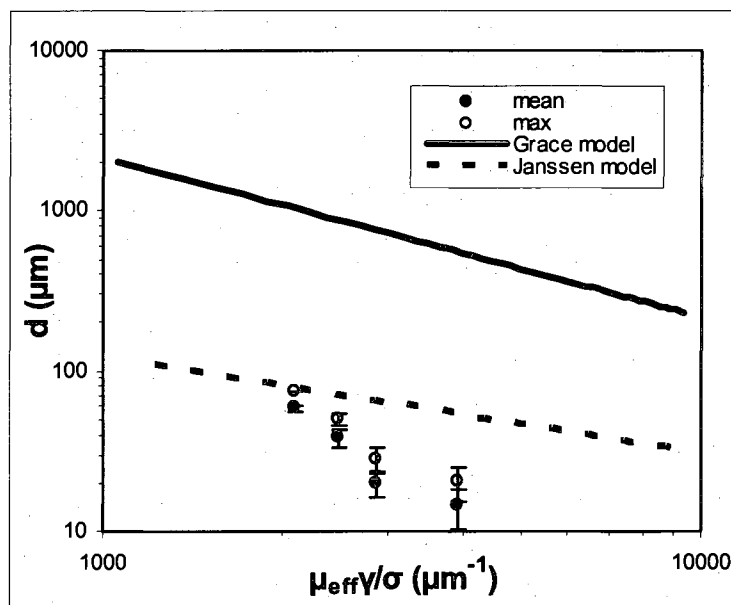


**Figure 4.18:** Comparison between model predictions and experimental data for the brine-in-crude-oil-A emulsions.



Figure 4.18 shows that both models over predict both the experimental mean and maximum drop sizes. The mean diameters were calculated based on Equation 4.14 while the maximum diameters were calculated based on 99% of the cumulative volume of the drop size distribution.

$$d_v = \frac{\sum(f_i d_i)}{\sum f_i} \quad (4.14)$$

For the  $i^{\text{th}}$  bin of the drop size distribution,  $f_i$  is the amplitude from NMR and  $d_i$  is the corresponding diameter. Both the Grace and Janssen models over predict the drop size.

The experimental data shows that the drop sizes of the crude oil emulsions have a steeper dependence on  $\left(\frac{\mu_{\text{eff}} \gamma}{\sigma}\right)$  than predicted by either model, thereby displaying the complex features that arise in the presence of surfactants.

The drop sizes of the brine-in-model-oil-A emulsions were also compared to the predictive models.

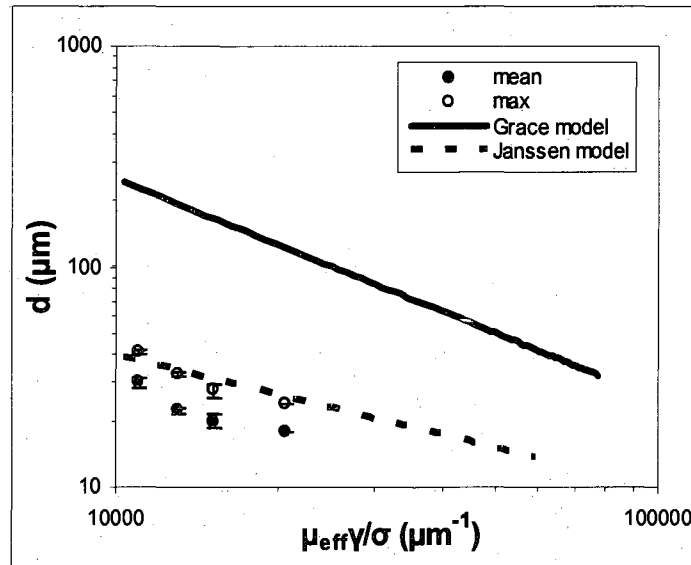
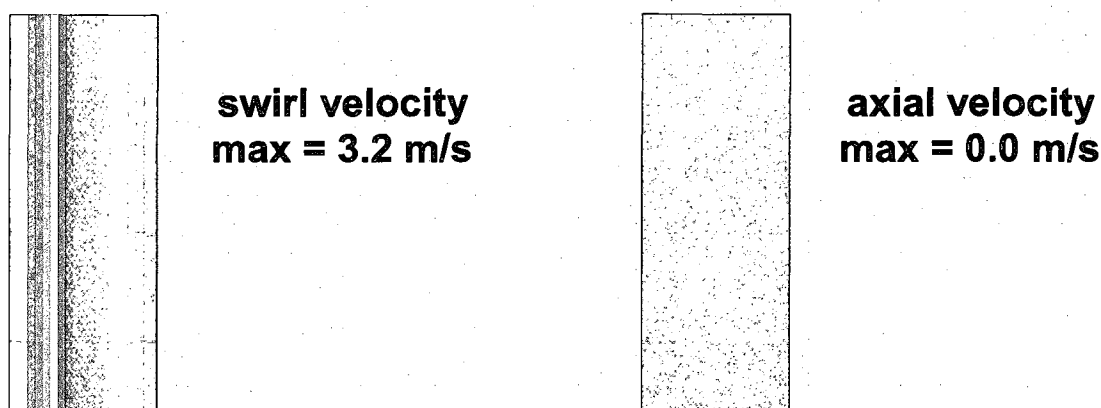


**Figure 4.19:** Comparison between model predictions and experimental data for the brine-in-model-oil-A emulsions.

Similar to the crude oil A emulsions, the drop sizes of the model oil A emulsions were over predicted by the Grace model. However, the Janssen model qualitatively predicted both the size and trend of the maximum drop diameter of the model oil A drop size distributions.

#### 4.4.2 Crude oil C/model oil B systems

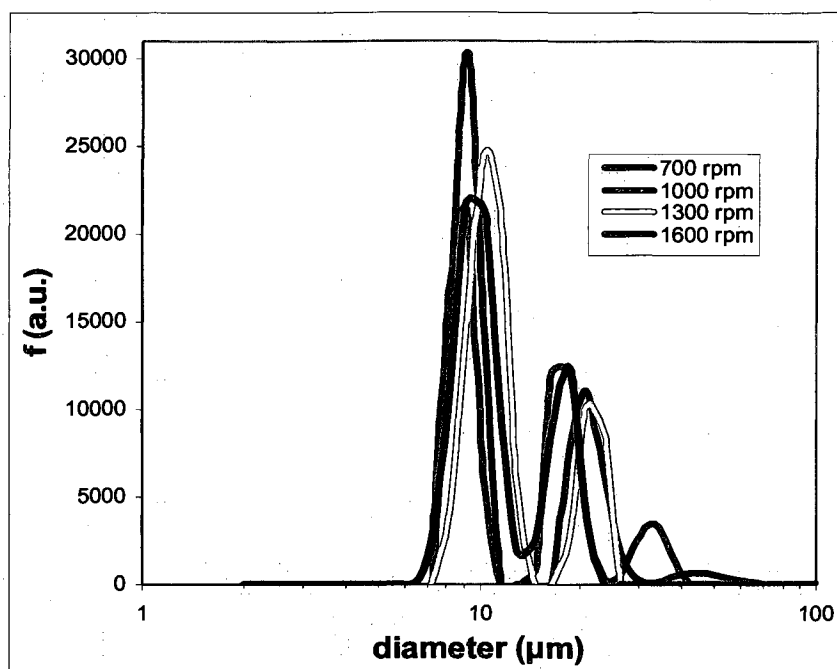
With the dispersed phase fraction equal to 0.2, the Kriegger-Dougherty viscosity for the crude oil C/model oil B systems was 400 cP. Figure 4.20 shows the CFD simulations at the maximum inner cylinder rotational speed.



**Figure 4.20:** Swirl and axial velocity profiles for the crude oil C/model oil B systems ( $\mu_{eff} = 400$  cP,  $\omega = 1600$  rpm).

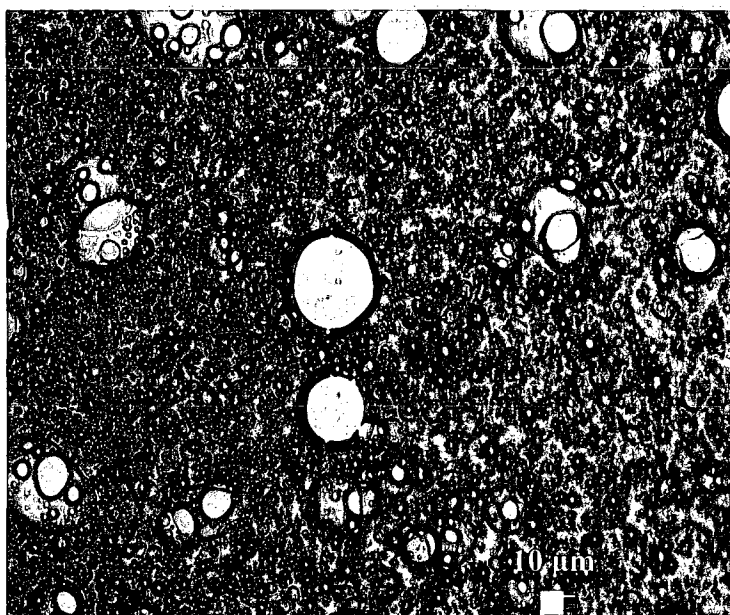
Figure 4.20 shows that even at the maximum inner cylinder rotational speed used in the crude oil C/model oil B systems, secondary flows do not develop. For these conditions,  $Re = 18$  and  $Ta = 43$  which is well below  $Ta_c$ . Simple shear flow dominates throughout the cell with a linear gradient in swirl velocity.

Figure 4.21 shows the drop size distributions for the brine-in-crude-oil-C emulsions as obtained by NMR.



**Figure 4.21:** Drop size distributions for brine-in-crude-oil-C emulsions.

Optical microscopy performed on the emulsion formed at 1300 rpm shows qualitative agreement with the NMR results.



**Figure 4.22:** Optical microscopy of the brine-in-crude-oil-C emulsion at 1300 rpm (objective = 20X).

The photograph in Figure 4.22 was obtained from the brine-in-crude-oil-C emulsion formed at 1300 rpm. A drop of the emulsion was placed on a glass slide and covered with a glass cover slip. The sample was not diluted with solvent. Figure 4.23 shows the drop size distributions for the brine-in-model-oil-B emulsions.

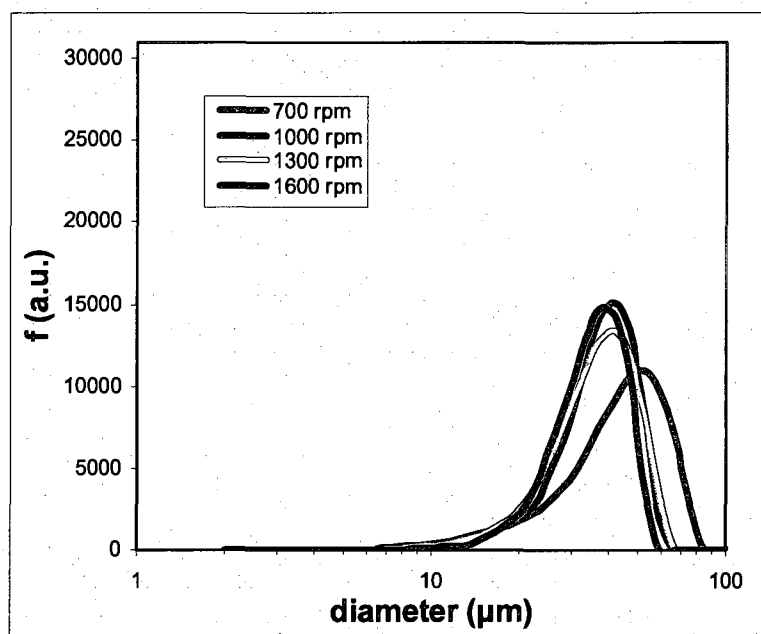


**Figure 4.23:** Drop size distributions for brine-in-model-oil-B emulsions.

At the same inner cylinder rotational speeds, the brine-in-crude-oil-B drop size distributions were multimodal while the brine-in-model-oil-B emulsions showed broad, unimodal drop size distributions. Given the similarity in viscosity, the difference in emulsion morphology between the two systems likely stems from differing interfacial properties and availability of surfactant during emulsification. Interfacial tension measurements indicate that with the addition of 0.356 wt.% Span80 to the model oil B, the surfactant migrates to the interface quickly. The crude oil C, however, contains a multitude of surfactants that take a period of time to migrate to the interface. These surfactant heterogeneities within crude oil C could possibly explain the distinct

populations of drops. With a homogeneous surfactant concentration in the model oil B, the emulsion drops exist with unimodal drop size distributions in simple shear flow.

The Grace and Janssen model comparisons are shown in Figures 4.24 and 4.25.

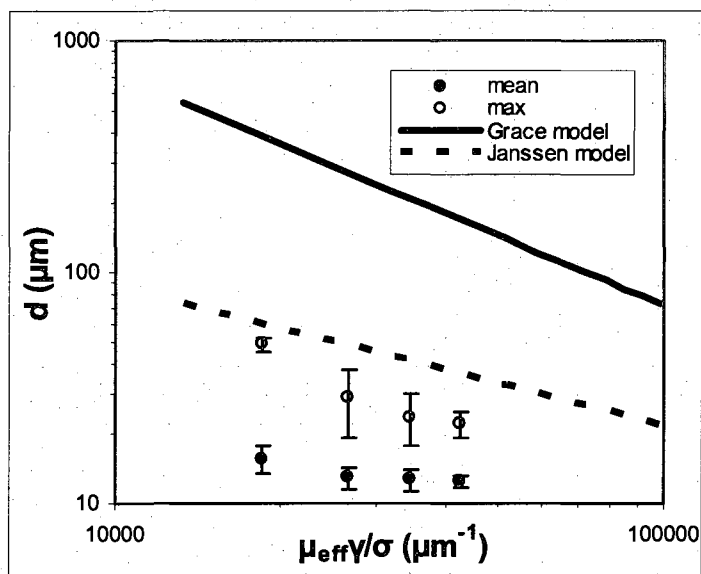


**Figure 4.24:** Comparison of experimental data to the Grace and Janssen models for the brine-in-crude-oil-C emulsions.

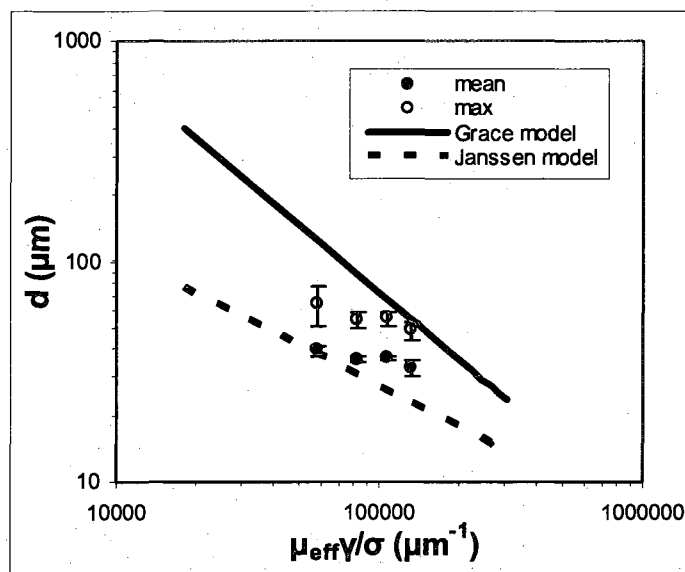


**Figure 4.25:** Comparison of experimental data to the Grace and Janssen models for the brine-in-model-oil-B emulsions.

The Grace and Janssen models over predict the experimental diameters for the brine-in-crude-oil-C emulsions. For the brine-in-model-oil-B emulsions, the Grace model over predicts the experimental diameters, while the Janssen model slightly under predicts the experimental diameters.

## 4.5 Conclusions

This work provides quantitative drop size distribution data for complex, concentrated emulsions. The PFG-DE technique effectively quantifies the morphology of these systems by not assuming a form of the drop size distribution and by considering the entire emulsion. By coupling the experimental data with computational fluid dynamics simulations, this work provides important quantitative insight about concentrated emulsion formation.

The crude/model oil A drop size distributions reflect the emergence of secondary flows as verified by CFD simulations. As the inner cylinder rotational speed increases in these systems, the drop size distributions become more multimodal. CFD simulations show that the secondary flows can lead to multimodal shear rate distributions, thereby leading to polydispersity in the drop size distributions. The experimental mean diameters reflect a power law dependence on  $\left( \frac{\mu_{eff} \gamma}{\sigma} \right)$  as expected by theories presented in the literature.

The crude oil C/model oil B emulsions display distinctly different morphologies. The brine-in-crude-oil-C emulsions display multimodal drop size distributions at each inner cylinder rotational speed while the brine-in-model-oil-B emulsions exhibit broad,

unimodal drop size distributions. This distinct difference in morphology of the emulsions likely arises from differences in interfacial properties between the two oils.

#### 4.6 Notation

$A$	interfacial area ( $\text{mm}^2$ )
$a$	x axis of deformed drop ( $\mu\text{m}$ )
$b$	y axis of deformed drop ( $\mu\text{m}$ )
$c$	z axis of deformed drop ( $\mu\text{m}$ )
$Ca$	capillary number
$Ca_c$	critical capillary number
$D$	drop deformation parameter
$d_{coal.}$	diameter predicted by Janssen's model ( $\mu\text{m}$ )
$d_i$	drop size of the $i^{\text{th}}$ bin ( $\mu\text{m}$ )
$d_{max}$	max. diameter predicted by Grace's work ( $\mu\text{m}$ )
$d_v$	volume weighted mean diameter ( $\mu\text{m}$ )
$f_i$	NMR amplitude of the $i^{\text{th}}$ bin (a.u.)
$H$	Hamaker constant (J)
$h_c$	critical thickness of interfacial film between two approaching drops ( $\mu\text{m}$ )
$r$	radius of un-deformed drop ( $\mu\text{m}$ )
$r_{max}$	max. drop radius in a simple shear field ( $\mu\text{m}$ )
$t$	time (s)
$\sigma$	interfacial tension ( $\text{mN/m}$ )
$\mu_{CP}$	viscosity of continuous phase ( $\text{Ns/m}^2$ )
$\mu_{DP}$	viscosity of dispersed phase ( $\text{Ns/m}^2$ )
$\mu_{KD}$	Kreiger-Dougherty viscosity ( $\text{Ns/m}^2$ )
$\mu_d$	interfacial viscosity ( $\text{Ns/m}^2$ )
$\alpha$	rate of distortion of continuous phase ( $\text{s}^{-1}$ )
$\lambda$	viscosity ratio
$\Omega$	inner cylinder angular speed ( $\text{s}^{-1}$ )
$\omega$	inner cylinder rotational speed (rpm)
$\gamma$	shear rate ( $\text{s}^{-1}$ )
$\varepsilon$	interfacial dilatational modulus ( $\text{mN/m}$ )
$\varepsilon_d$	interfacial elasticity ( $\text{mN/m}$ )
$\phi$	volume fraction

## Chapter 5: Characterizing Water-in-Crude-Oil Emulsions Formed with a Rushton Turbine

### 5.1 Introduction

Formation and stability characteristics of emulsions formed in complex flow fields are particularly applicable to the energy industry.<sup>5, 89</sup> Water, usually in the form of brine, is commonly produced in conjunction with crude oil. During the production of crude oil, the produced fluids can experience a wide range of flow conditions including both laminar and turbulent regimes. These flow regimes affect both the formation and stability of the emulsions.

In the laboratory, emulsions are generated using a variety of techniques, one of which is the use of a turbine mixer, specifically referred to as a Rushton turbine.<sup>90, 91</sup> Rushton turbines have been widely used in industry and academia to investigate mixing phenomena and drop breakup.<sup>17, 21, 90-94</sup> Rushton turbines facilitate adequate mixing of the immiscible fluids and provide sufficient shear to disperse water drops in oil. Both turbulent and laminar flow regimes can occur during the use of a turbine mixer. Published correlations facilitate the calculation of power and energy applied to the emulsion systems.

Hinze pioneered drop breakup in turbulent flow by showing that the maximum equilibrium drop size was a function of the energy dissipation rate.<sup>95</sup>

$$d_{\max} = C \epsilon^{-0.4} \left( \frac{\sigma}{\rho_{CP}} \right)^{0.6} \quad (5.1)$$

Work by Hinze showed that drop breakup in a stirred tank environment primarily occurs in the impeller region due to turbulent pressure fluctuations along the drop's surface.<sup>92, 95</sup>



Subsequently, Chen and Middleman used similar arguments to empirically derive an expression for the Sauter diameter for dilute emulsions with an inviscid dispersed phase produced by Rushton turbines.<sup>96</sup>

$$\frac{d_{32}}{L} = 0.053 We^{-3/5} \quad (5.2)$$

The Sauter mean diameter,  $d_{32}$ , is the size of a drop which has the same volume-to-surface area ratio as the entire population of drops.<sup>41</sup> Therefore, the Sauter mean diameter gives important information about the available interfacial area of the drops in the distribution. The Sauter mean diameter is commonly used in the literature to describe drop breakup in turbulent flow that incorporates turbine mixers.<sup>92-94, 96</sup> The Weber number,  $We$ , is defined according to Equation 5.3.

$$We = \frac{\rho_{CP} \gamma^2 L^3}{\sigma} \quad (5.3)$$

Wang accounted for the viscosity of the dispersed phase and adjusted the correlation accordingly.<sup>94</sup>

$$\frac{d_{32}}{L} = 0.053 We^{-3/5} [1 + 0.97 V_i^{0.79}]^{3/5} \quad (5.4)$$

The viscosity group is  $V_i$ .

$$V_i = \left( \frac{\rho_{CP}}{\rho_{DP}} \right)^{1/2} \mu_{DP} \frac{\gamma L}{\sigma} \quad (5.5)$$

To account for increased dispersed phase fractions, Calabrese developed an empirical formulation for dispersed phase fractions less than or equal to 0.2, though the dependence of  $d_{32}$  on dispersed phase fraction has not been experimentally validated.<sup>93</sup>

$$\frac{d_{32}}{L} = 0.054 (1 + 3 \phi) We^{-3/5} \left[ 1 + 4.42 (1 - 2.5 \phi) V_i \left( \frac{d_{32}}{L} \right)^{1/3} \right]^{3/5} \quad (5.6)$$

Equation 5.6 accounts for the effect of dispersed phase volume fraction on disruptive energy. Despite this work, there still remains a gap in characterizing drop size distributions of concentrated emulsions formed in turbulent flow in the presence of surfactants. Particularly, there is a need for drop size information for opaque emulsions such as crude oil emulsions.

This chapter employs a Rushton turbine to form water-in-crude-oil emulsions. In contrast to Chapter 4, the present chapter provides transient drop size information for crude oil emulsions formed in inhomogeneous shearing conditions. This work used transverse relaxation techniques to measure drop size distributions of crude oil emulsions, as described in Chapter 2. The data provides insight about the effects of power and energy input on emulsion drop size. The data is compared to published correlations that predict drop size in turbulent flow.

## **5.2 Experimental methods**

### **5.2.1 Fluid properties**

For all experiments described in this chapter, the dispersed phase was ASTM brine and the dispersed phase volume fraction was equal to 0.2 by combining 10 mL brine with 40 mL oil. Two types of crude oils were considered in this work, and they are the same crude oil A and crude oil C described in Chapter 4.

The  $T_2$  distributions were obtained for pure crude oil A, crude oil C, and brine at 303.2 K.

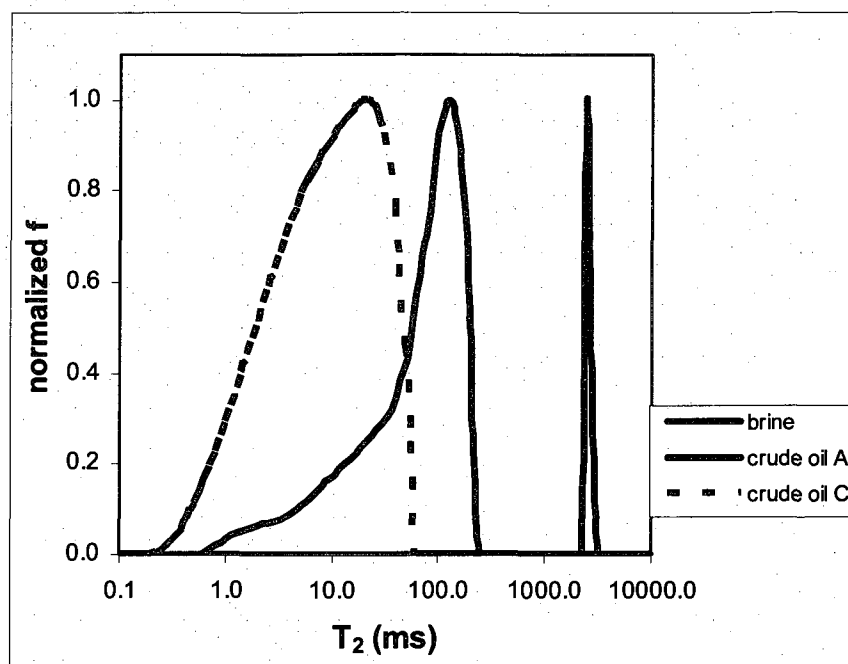


**Figure 5.1:**  $T_2$  distributions of pure crude oil A, crude oil C, and brine at 303.2 K.

The log mean of the bulk brine  $T_2$  distribution is 2550 ms. As expected, the  $T_2$  distribution of the more viscous crude oil C is shifted toward lower  $T_2$  values compared to the less viscous crude oil A  $T_2$  distribution. In addition, both crude oil  $T_2$  distributions are broad indicating the presence of a multitude of components. By contrast, the pure brine consists of a narrow, single peak.

### 5.2.2 Emulsion preparation equipment

A six bladed Rushton turbine was used to form the emulsions. The turbine was connected to a 115 volt, 0.31 amp, DC motor. A variac connected to the motor was used to adjust the mixing speed. A digital tachometer was used to measure the rotational speed of the impeller (rpm). The diameter of the impeller was 30mm. The impeller was attached to a shaft connected to the motor.

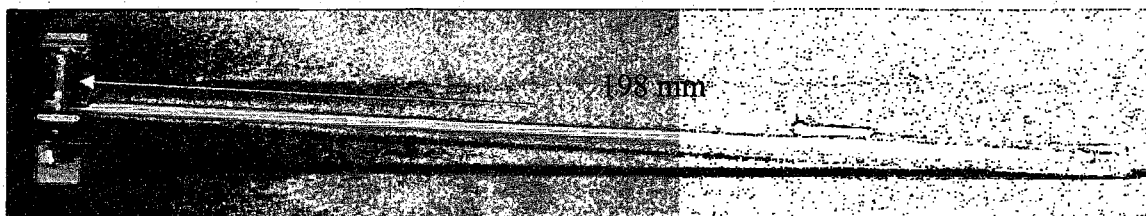


**Figure 5.2:** Impeller and shaft.

The emulsions were prepared in a glass vessel with the inside diameter equal to 43 mm and the length equal to 210 mm. Figure 5.3 shows the dimensions of the Rushton turbine relative to the glass vessel.

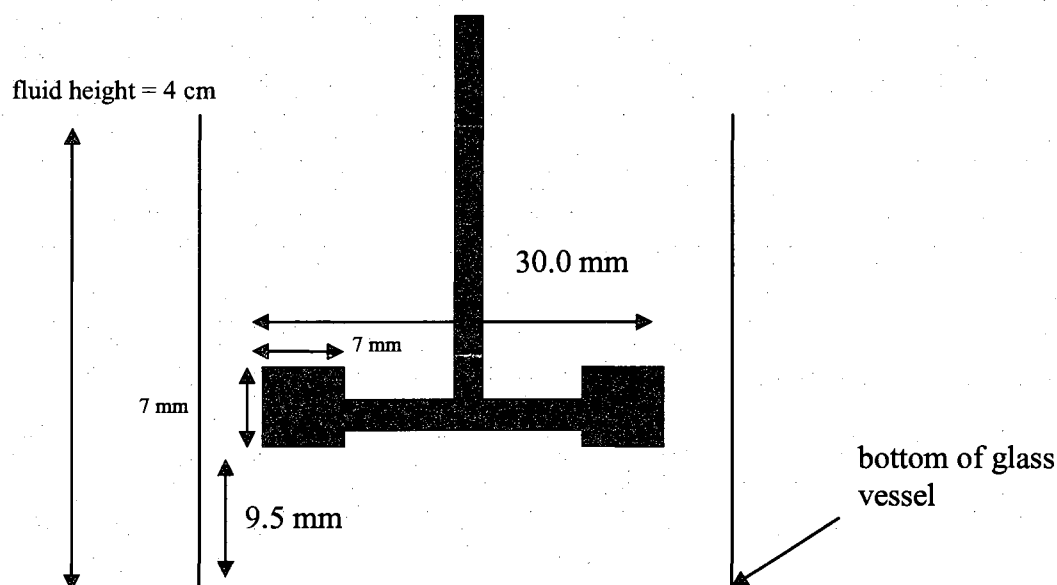


**Figure 5.3:** Position of the impeller.

For all experiments, the emulsions were mixed and measured in the same vessel.

Therefore, the entire sample that was mixed was also used for the measurement. Because of the high viscosity of the crude oil C, the brine-in-crude-oil-C emulsions were formed in a circulating water bath with temperature equal to 303.2 K.

### 5.2.3 Applied shear equipment

A bench top roller was used to apply mild shear to the samples after emulsification.

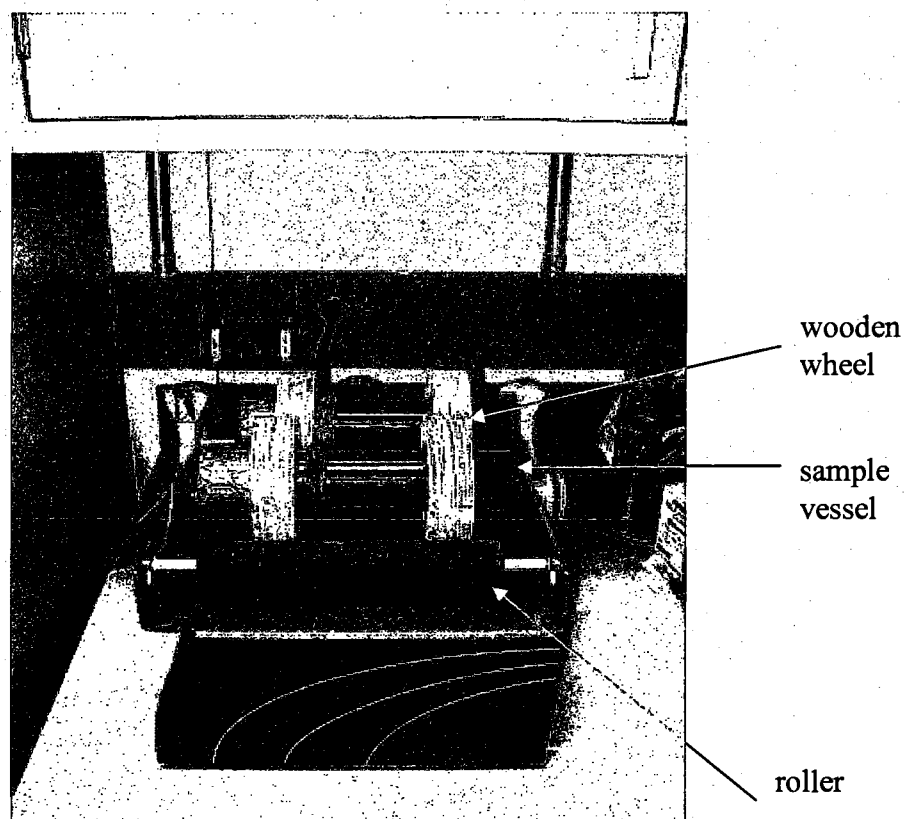


**Figure 5.4:** Bench top roller used to apply shear after emulsification.

The rollers' maximum rotational speed was 4 rpm, and this was the speed that was used in all of the experiments. The bench top roller had a maximum capacity of two sample vessels.

#### 5.2.4 NMR measurements

A 2 MHz NMR spectrometer was used to measure drop size distributions of water-in-crude-oil-emulsions. Specifically, CPMG<sup>43,44</sup> measurements were performed, and the  $T_2$  distributions of the emulsions were determined according to the methodology described in Chapter 2. As described in Chapter 2, the  $T_2$  distribution of a sample is a

function of the bulk  $T_2$  value of the dispersed phase, the surface relaxivity, and the surface:volume ratio.<sup>41</sup> Therefore, the drop size distribution of the emulsion can be obtained using Equation 5.7.

$$d_i = 6 \rho \left( \frac{1}{T_{2,DP,i}} - \frac{1}{T_{2,bulk}} \right)^{-1} \quad (5.7)$$

In this equation,  $\rho$  is the surface relaxivity, and it indicates the amount of relaxation that occurs at the interface. When determining the drop size distribution from the  $T_2$  distribution, the amplitude values from the  $T_2$  distribution are matched with the corresponding diameter values. The amplitude values associated with the diameters are normalized with the sum of the water amplitude values. Therefore, each diameter has a corresponding volume weighted amplitude. Thus, the volume weighted drop size distribution can be calculated if the  $T_2$  distribution is known with the limitations described in Chapter 2.

The surface relaxivity of a water/oil system can be determined by performing a PFG-DE measurement. The mean diameter and mean  $T_2$  is measured and used in Equation 5.8.

$$\rho = \frac{d_v}{6} \left( \frac{1}{T_{2,lm}} - \frac{1}{T_{2,bulk}} \right) \quad (5.8)$$

The volume weighted mean diameter is denoted as  $d_v$  and the log mean of the  $T_2$  distribution is  $T_{2,lm}$ . The surface relaxivity between the brine and crude oil A was measured to be 0.4  $\mu\text{m/s}$ , as obtained from Figure 5.5.

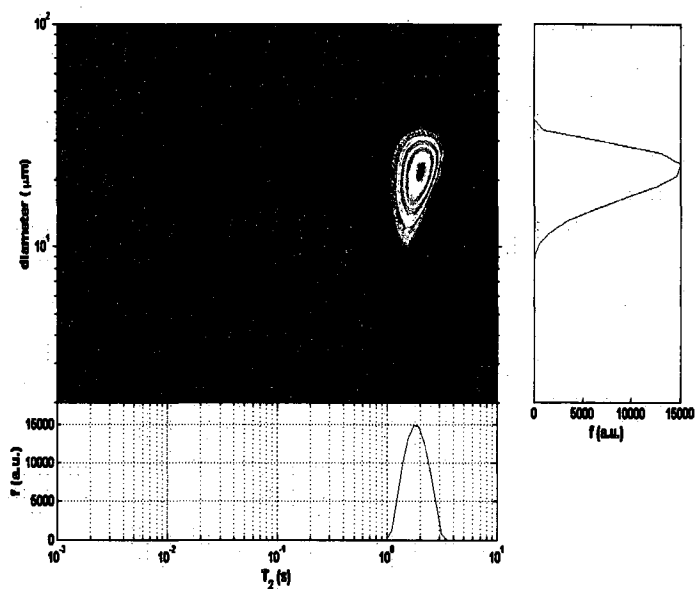


**Figure 5.5:** PFG-DE measurement used to determine the surface relaxivity for the brine-in-crude-oil-A system.

Similarly, the surface relaxivity of the brine-in-crude-oil-B system was measured to be  $0.9 \mu\text{m/s}$ . The surface relaxivity was assumed to be constant for each system.<sup>4</sup>

## 5.3 Results

### 5.3.1 Crude oil A: High mixing $Re$ with no applied shear after emulsification

This section discusses the results for the crude oil A emulsions formed with high mixing  $Re$  and no applied shear after mixing. First, drop size distributions with 10 minutes of mixing were obtained for three samples.

**Table 5.1:** Brine-in-crude-oil-A emulsions with 10 minutes of high mixing  $Re$  and no applied shear after emulsification.

sample #	$Re$	$N$ (rpm)	$P$ (W)	$E$ (kJ)
1	2990	3571	6.6	4.0
2	3140	3750	7.4	4.4
3	2718	3246	5.0	3.0

The Reynolds number was calculated according to Equation 5.9.<sup>90, 91</sup>

$$Re = \frac{d_{imp}^2 N \rho_{CP}}{\mu_{CP}} \quad (5.9)$$

Based on correlations by J.H. Rushton,<sup>90, 91</sup> the power number,  $N_P$ , was determined and the power input to the system was calculated.

$$P = \frac{N_P}{\left( \frac{g}{N^2 d_{imp}} \right)^{\left( \frac{a - \log(Re)}{b} \right)}} \frac{\rho_{CP} N^3 d_{imp}^5}{g} \quad (5.10)$$

The Sauter mean diameter was calculated for each distribution.<sup>41</sup>

$$d_{32} = \frac{\sum_{i=1}^M d_i^3 f_i}{\sum_{i=1}^M d_i^2 f_i} \quad (5.11)$$

The drop size distributions were obtained at several times after preparation (0 min., 30 min., 1 hr., 2 hr., 5 hr., 24 hr.). The following figure shows the transient Sauter diameters for the mean and three samples.



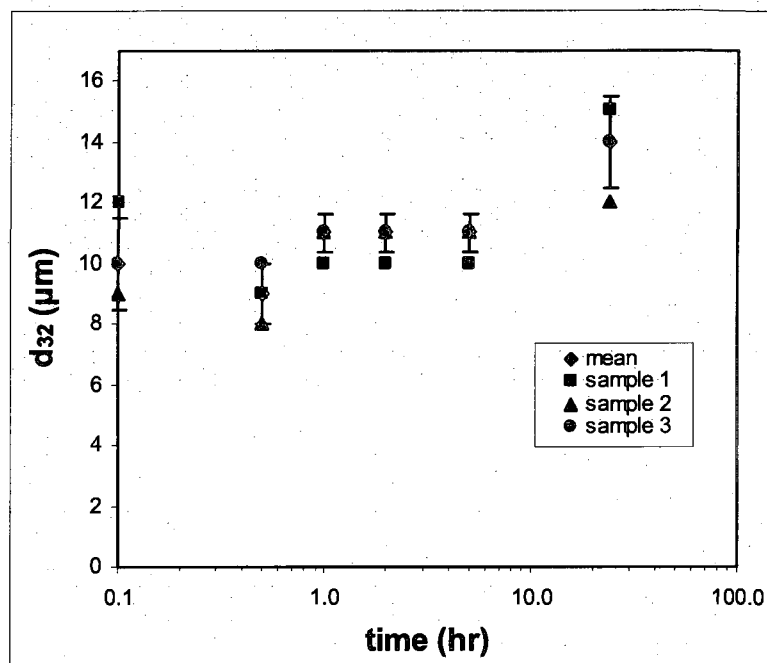


**Figure 5.6:** Brine-crude-oil-A Sauter diameters with 10 minutes of high mixing  $Re$  and no applied shear after emulsification.

Figure 5.6 illustrates that the Sauter diameter does not change appreciably with time under these conditions. The transient drop size distributions for one of the samples are given below.

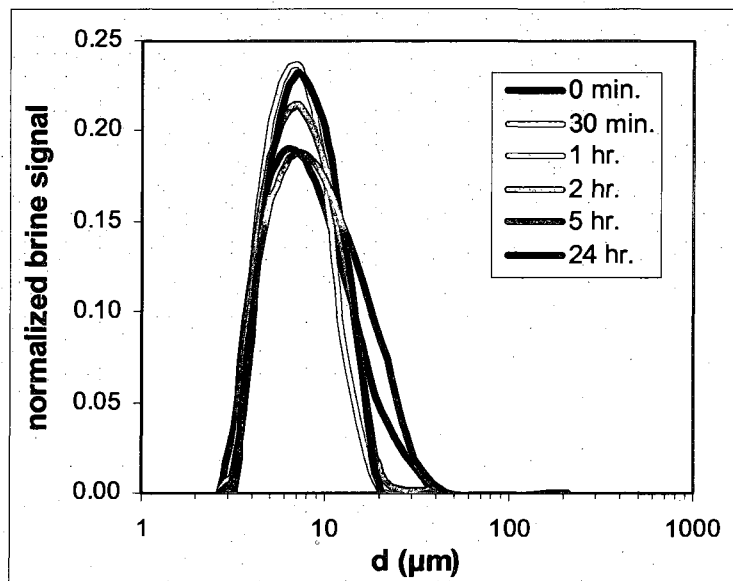


**Figure 5.7:** Brine-in-crude-oil-A drop size distributions with 10 minutes of high mixing  $Re$  and no applied shear after emulsification.

Figure 5.7 indicates that 10 minutes of mixing using high mixing speeds produced stable emulsions.

The mixing time of the brine-in-crude-oil-A emulsions was decreased to 1 minute with no applied shear after emulsification.

**Table 5.2:** Brine-in-crude-oil-A emulsions with 1 minute of high mixing  $Re$  and no applied shear after emulsification.

sample #	$Re$	$N$ (rpm)	$P$ (W)	$E$ (kJ)
1	3017	3603	6.8	0.4
2	2908	3472	6.1	0.4

The Sauter diameters as a function of time after emulsification are shown in Figure 5.8.

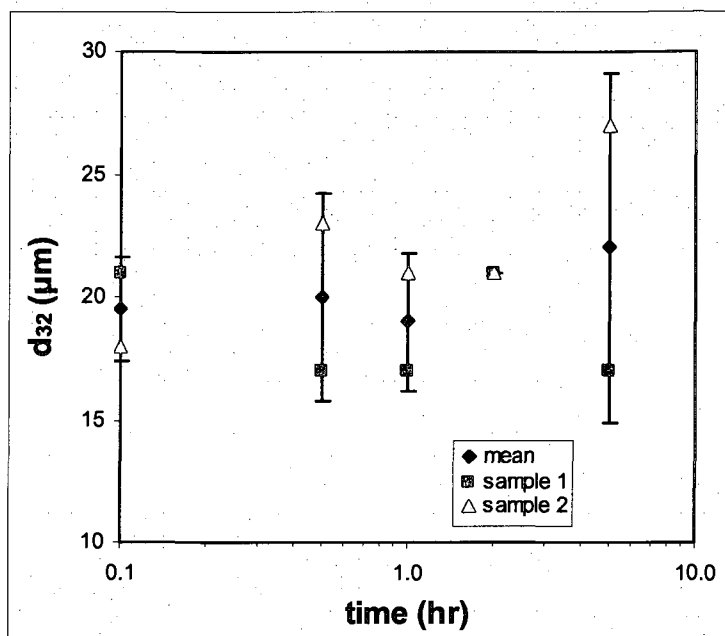


**Figure 5.8:** Brine-in-crude-oil-A Sauter diameters with 1 minute of high mixing  $Re$  and no applied shear after emulsification.

The drop size was too large to measure with NMR 24 hours after emulsification. The drop size distributions for one of the samples are given below.

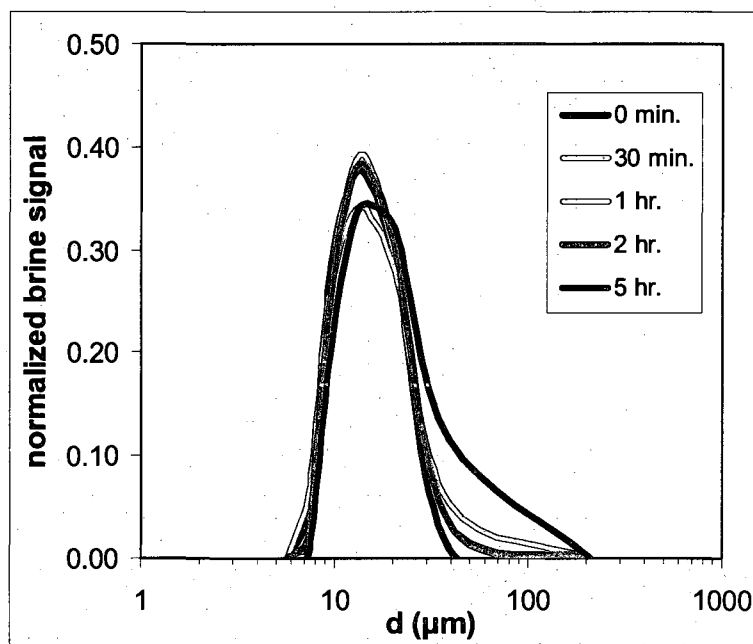


**Figure 5.9:** Brine-in-crude-oil-A drop size distributions with 1 minute of high mixing  $Re$  and no applied shear after emulsification.

With one minute of mixing, the transverse relaxation of the dispersed phase approached the bulk brine value, thereby introducing an increase in width of the drop size distribution.

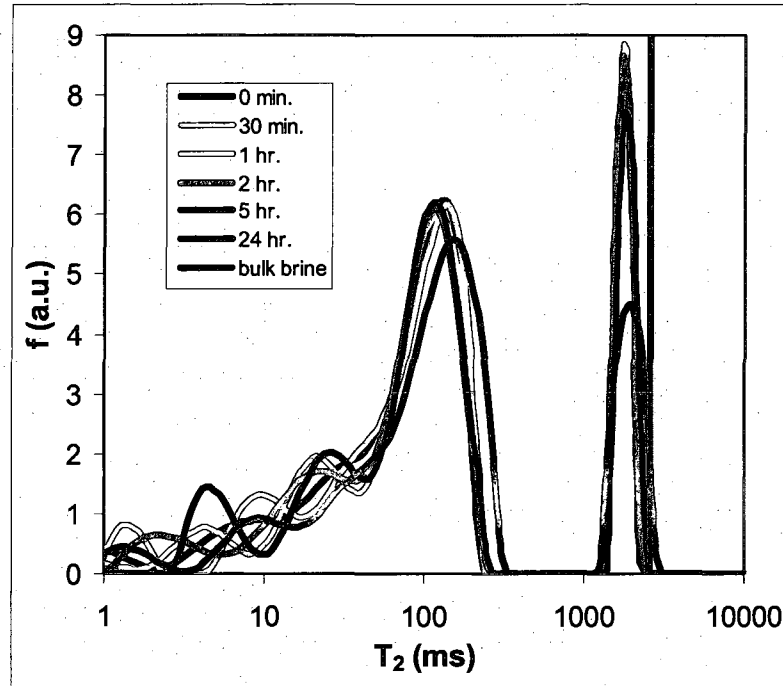


**Figure 5.10:** Brine-in-crude-oil-A transient  $T_2$  distributions with 1 minute of high mixing  $Re$  and no applied shear after emulsification.

Equation 5.7 shows that if  $T_{2,DP}$  overlaps  $T_{2,bulk}$ , ambiguous results arise in the drop size distribution. Therefore, the CPMG technique was unable to yield the drop size distribution 24 hours after emulsification.

Comparison of 10 minutes and 1 minute of mixing of the brine-in-crude-oil-A emulsions using high mixing speeds with no applied shear after emulsification revealed that drop size was affected by mixing time. Given the same mixing  $Re$ , the drops were larger and experienced coalescence with 1 minute of mixing.

### 5.3.2 Crude oil A: High mixing $Re$ with applied shear after emulsification

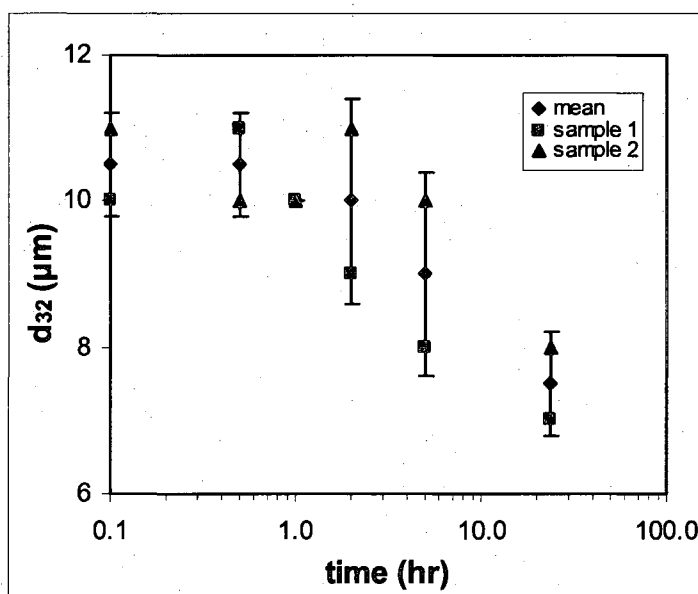
This section presents results for brine-in-crude-oil-A emulsions with high mixing  $Re$  and applied shear after emulsification. The shear was applied after emulsification using the bench top roller. Table 5.3 contains the experimental parameters for each sample.

**Table 5.3:** Brine-in-crude-oil-A with 10 minutes of high mixing  $Re$  and applied shear after emulsification.

sample #	$Re$	$N$ (rpm)	$P$ (W)	$E$ (kJ)
1	2903	3466	6.1	3.7
2	2612	3119	4.6	2.8

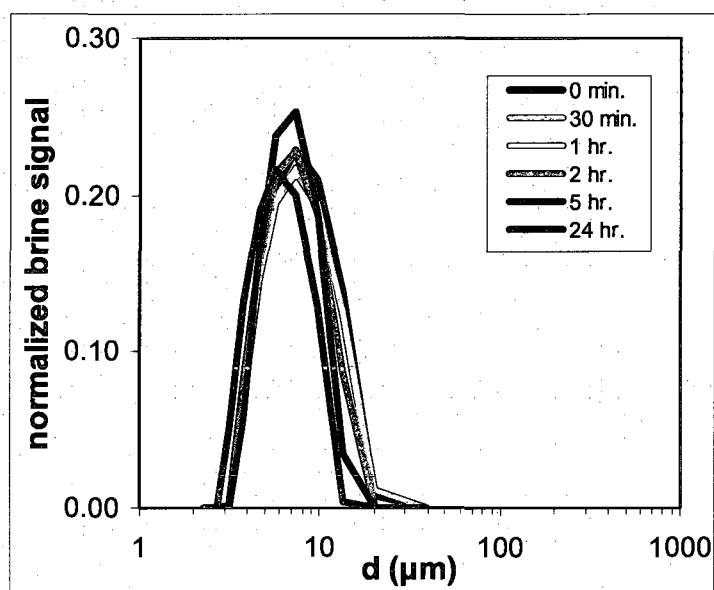
The Reynolds numbers and power numbers were kept in the same ranges that were used for the experiments with no applied shear after emulsification.

Figure 5.11 shows that the Sauter diameter decreased slightly with the application of the mild shear.



**Figure 5.11:** Brine-in-crude-oil-A Sauter diameters with 10 minutes of high mixing  $Re$  and applied shear after emulsification.

Figure 5.11 shows that the emulsions were stable in the presence of a mild shear and surfactant, as was expected based on work in the literature for dilute emulsions.<sup>97</sup> Nandi observed a reduction in the coalescence frequency of 1 vol.% emulsions in the presence of surfactant by applying mild shear. The authors attributed this observation to the ability of surfactants to stabilize the thin films between drops, and the applied shear rate minimized the contact time during droplet collisions, thereby reducing the coalescence rate.<sup>97</sup> Figure 5.12 shows the transient drop size distributions of one of the samples.



**Figure 5.12:** Brine-in-crude-oil-A drop size distributions with 10 minutes of high mixing  $Re$  and applied shear after emulsification.

The mixing time was decreased to 1 minute and shear was applied after emulsification.

**Table 5.4:** Brine-in-crude-oil-A emulsions with 1 minute of high mixing  $Re$  and applied shear after emulsification.

sample #	$Re$	$N$ (rpm)	$P$ (W)	$E$ (kJ)
1	2884	3384	5.7	0.3
2	2776	3315	5.5	0.3

With 1 minute of mixing, the diameter also decreased slightly with the application of mild shear after emulsification.

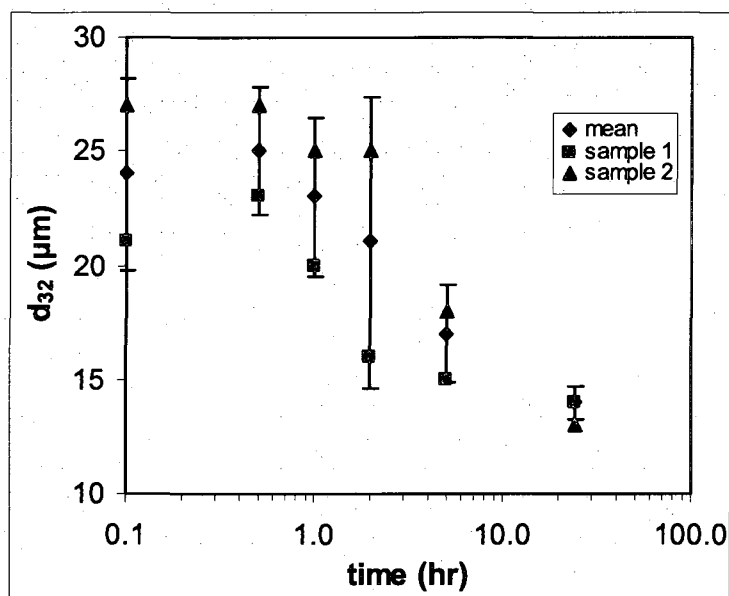


**Figure 5.13:** Brine-in-crude-oil-A Sauter diameters with 1 minute of high mixing  $Re$  and applied shear after emulsification.

The diameters were initially the same order of magnitude as the drops created with no applied shear after emulsification and 1 minute of mixing. However, the applied shear caused the emulsions to resist coalescence. This behavior is further illustrated with the transient drop size distributions of one of the samples.

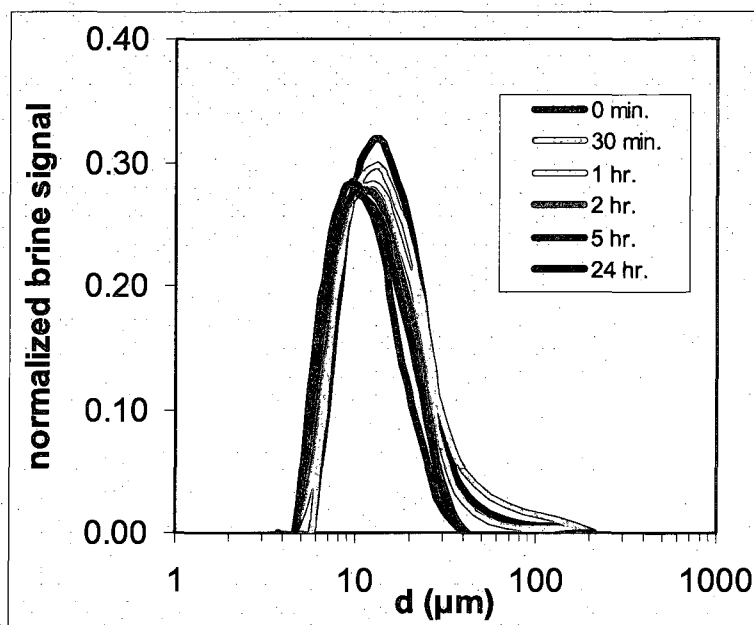


**Figure 5.14:** Brine-in-crude-oil-A drop size distributions with 1 minute of high mixing  $Re$  and applied shear after emulsification.

The results for both 10 minutes and 1 minute of mixing with applied shear after emulsification indicate that the emulsions resist coalescence throughout the duration of the experiments. In contrast to 1 minute of mixing with no applied shear after emulsification, 1 minute of mixing with applied shear after emulsification produced emulsions with drop size distributions that could be measured 24 hours after formation. Based on observations by Nandi, the application of mild shear in the presence of surfactants is expected to reduce the coalescence rate of emulsions.<sup>97</sup> The crude oil emulsions described in this section displayed similar behavior.

### 5.3.3 Crude oil A: Low mixing $Re$ with no applied shear after emulsification

This section contains results for emulsions formed using low mixing  $Re$  ( $Re = 300 - 420$ ). The low Reynolds number regime was chosen in order to match the highest attainable Reynolds number of the crude oil C emulsions.



**Table 5.5:** Brine-in-crude-oil-A with 10 minutes of low mixing  $Re$  and no applied shear after emulsification.

sample #	$Re$	$N$ (rpm)	$P$ (W)	$E$ (kJ)
1	406	485	0.04	0.024
2	410	490	0.04	0.024
3	410	490	0.04	0.024

For all times, the dispersed  $T_2$  distributions overlapped the bulk brine  $T_2$  value, so no drop size distributions were obtained.

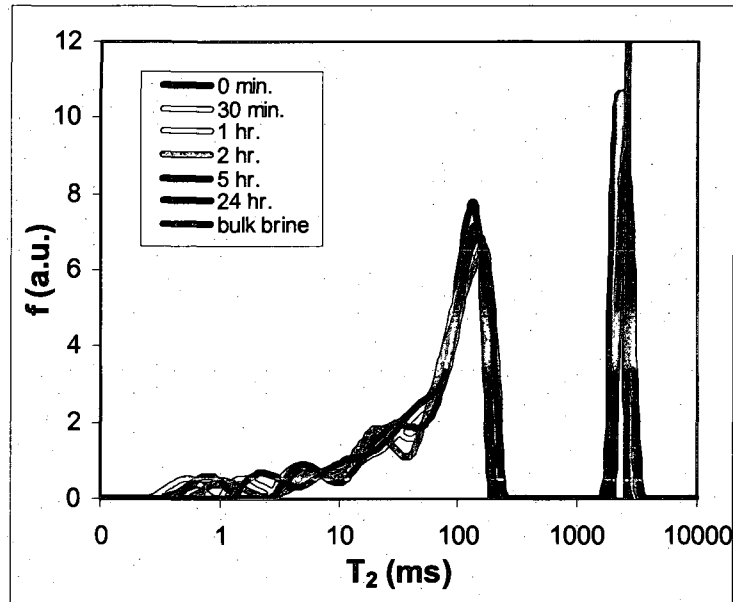


**Figure 5.15:** Brine-in-crude-oil-A transient  $T_2$  distributions with 10 minutes of low mixing  $Re$  and no applied shear after emulsification.

These results indicate that low mixing  $Re$  produced emulsions with drop size distributions that could not be quantified using the CPMG technique. Figure 5.16, taken 24 hours after emulsion formation, illustrates the two phase separation that was observed.

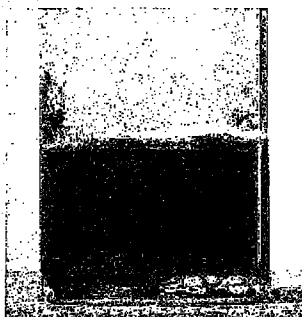


**Figure 5.16:** Brine-in-crude-oil-A emulsion 24 hours after emulsion formation with 10 minutes of low mixing  $Re$  and no applied shear after emulsification.

Two phase separation occurred, and NMR was unable to distinguish brine drops from bulk brine.

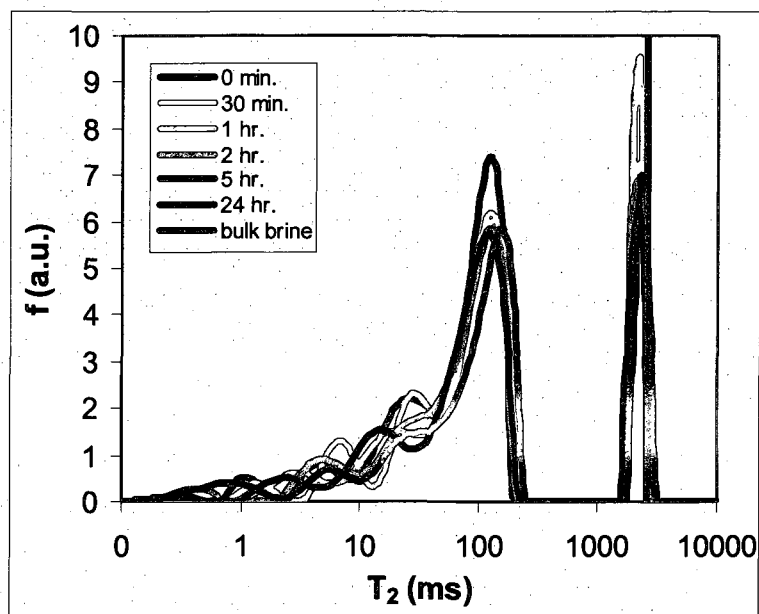
#### 5.3.4 Crude oil A: Low mixing $Re$ with applied shear after emulsification

Table 5.6 contains the mixing information for the two samples.

**Table 5.6:** Brine-in-crude-oil-A with 10 minutes of low mixing  $Re$  and applied shear after emulsification.

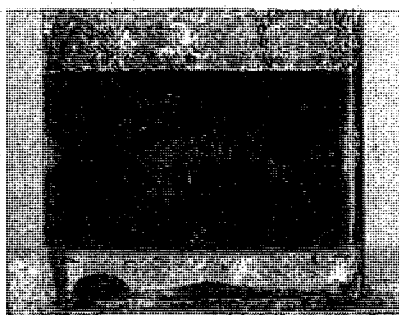
sample #	$Re$	$N$ (rpm)	$P$ (W)	$E$ (kJ)
1	419	500	0.04	0.024
2	419	500	0.04	0.024

Figure 5.17 shows that for the duration of the experiment, the dispersed  $T_2$  distribution overlaps the bulk brine  $T_2$  value.



**Figure 5.17:** Brine-in-crude-oil-A  $T_2$  distributions with 10 minutes of low mixing  $Re$  and applied shear after emulsification.

Drop size distributions were not obtained at any time due to the overlap of  $T_{2,DP}$  and the bulk brine value. Figure 5.18 illustrates the two phase separation of the brine-in-crude-oil-A emulsion 24 hours after formation.



**Figure 5.18:** Brine-in-crude-oil-A emulsion 24 hours after formation with 10 minutes of low mixing  $Re$  and applied shear after emulsion formation.

The application of mild shear after emulsification did not reduce the coalescence of the brine-in-crude-oil-A emulsions formed with low mixing  $Re$ .

### 5.3.5 Crude oil C: Low mixing $Re$ with no applied shear after emulsification

Due to the limitations of the mixer, only one Reynolds number region was explored for the crude oil C emulsions ( $Re = 300 - 420$ ). The following preparation conditions were used with 10 minutes of mixing.

**Table 5.7:** Brine-in-crude-oil-C mixing conditions with 10 minutes of low mixing  $Re$  and no applied shear after emulsification.

sample #	$Re$	$N$ (rpm)	$P$ (W)	$E$ (kJ)
1	385	6564	86.1	51.7
2	401	6836	96.8	58.1
3	405	6900	99.4	59.6

Though the Reynold's numbers for the crude oil C and crude oil A were kept in the same range (300 – 420), the power required for making the emulsions with the crude oil C (~100 W) was larger than the power required to make the emulsions with the crude oil A (0.04 W).

The Sauter diameters did not change with time.

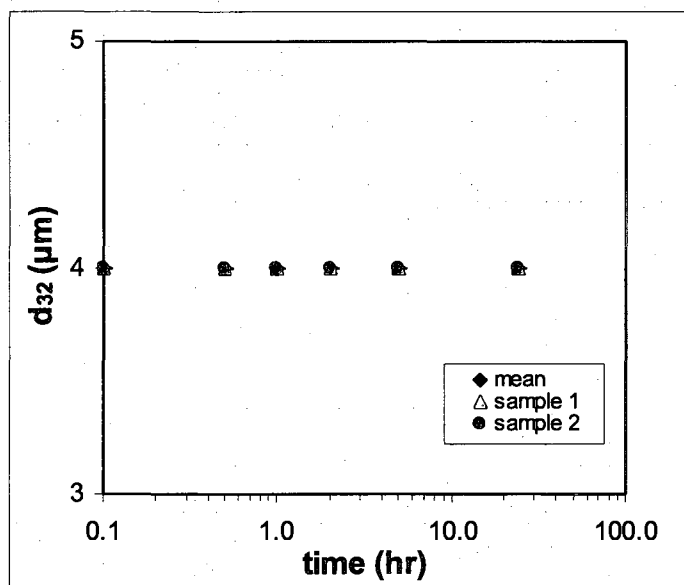


**Figure 5.19:** Brine-in-crude-oil-C Sauter diameters with 10 minutes of low mixing  $Re$  and no applied shear after emulsification.

Even with the low Reynolds number of mixing, the brine remained dispersed in the crude oil C throughout the duration of the experiments.

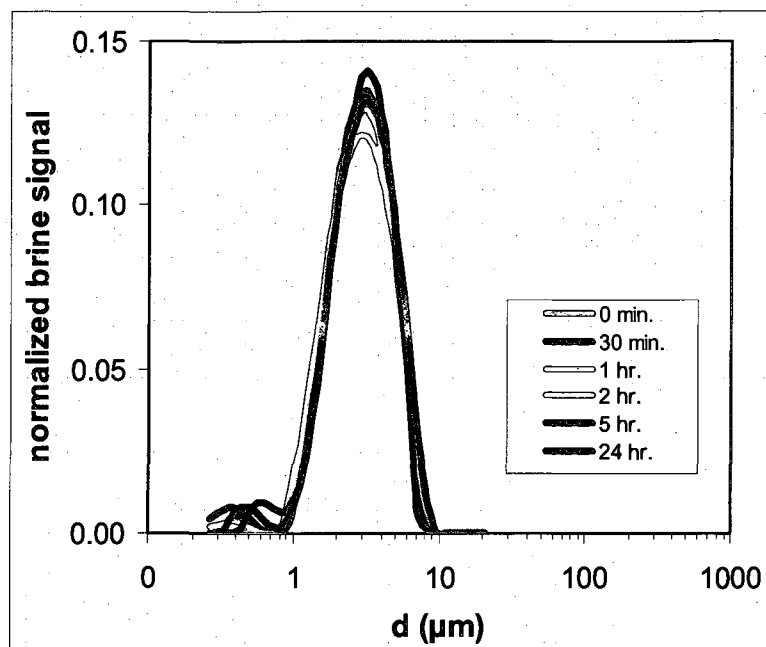


**Figure 5.20:** Brine-in-crude-oil-C drop size distributions with 10 minutes of low mixing  $Re$  and no applied shear after emulsification.

For the same Reynold's number of mixing as the brine-in-crude-oil-A emulsions, the drops in the brine-in-crude-oil-C emulsions were smaller. In addition, the drops in the the brine-in-crude-oil-C emulsions remained dispersed throughout the duration of the experiments, while the brine-in-crude-oil-A emulsions resulted in two phase separation.

Experiments were performed using the crude oil C with 1 minute of low mixing  $Re$ .

**Table 5.8:** Brine-in-crude-oil-C mixing conditions with 1 minute of low mixing  $Re$  and no applied shear after emulsification.

sample #	$Re$	$N$ (rpm)	$P$ (W)	$E$ (kJ)
1	352	6000	66.4	4.0
2	360	6130	70.7	4.2

The transient Sauter diameter did not change appreciably with 1 minute of mixing.

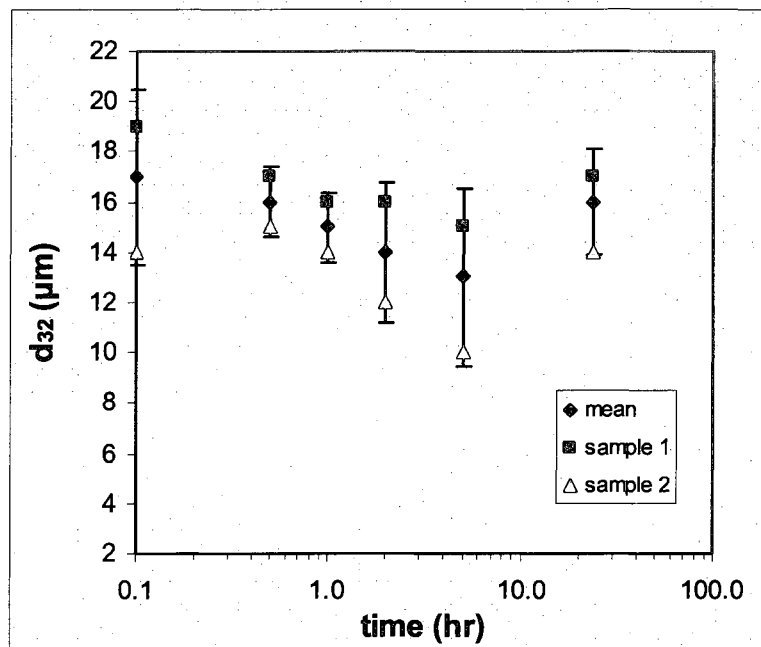


**Figure 5.21:** Brine-in-crude-oil-C Sauter diameters with 1 minute of low mixing  $Re$  and no applied shear after emulsification.

The drop size distributions for one of the samples are given in the following figure.

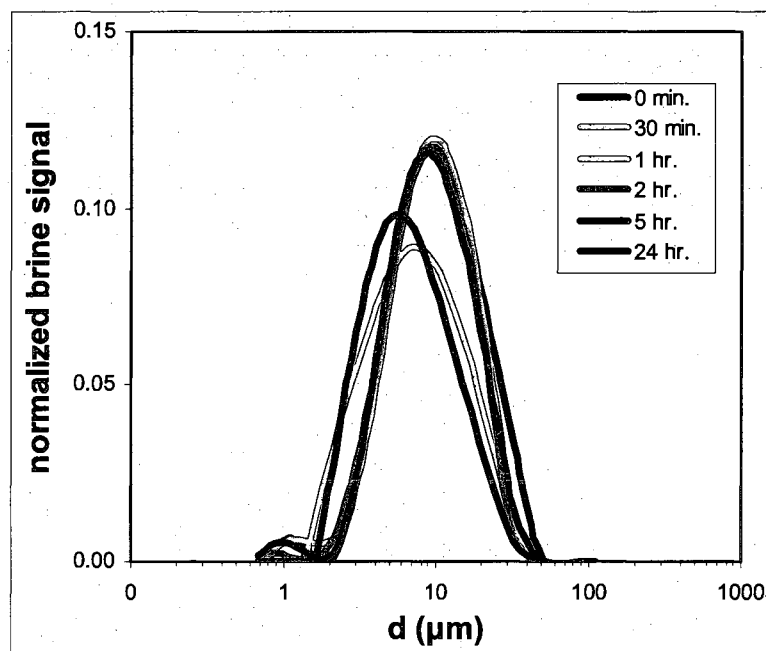


**Figure 5.22:** Brine-in-crude-oil-C drop size distributions with 1 minute of low mixing  $Re$  and no applied shear after emulsification.

Unlike the brine-in-crude-oil-A emulsions formed in the same flow regime ( $Re = 300 - 420$ ), the brine drops in the brine-in-crude-oil-C emulsions remained dispersed throughout the duration of the experiments.

### 5.3.6 Crude oil C: Low mixing $Re$ with applied shear after emulsification

The effects of mild shear after emulsification was investigated in the brine-in-crude-oil-C emulsions. The following table contains the mixing information for the crude oil C emulsions formed with 10 minutes of low mixing  $Re$  with applied shear after emulsification.

**Table 5.9:** Brine-in-crude-oil-C mixing conditions with the application of mild shear after 10 minutes of low mixing  $Re$ .

sample #	$Re$	$N$ (rpm)	$P$ (W)	$E$ (kJ)
1	344	5866	62.3	37.4
2	350	5942	64.6	38.8

The Sauter diameter increased slightly with time as shear was applied.

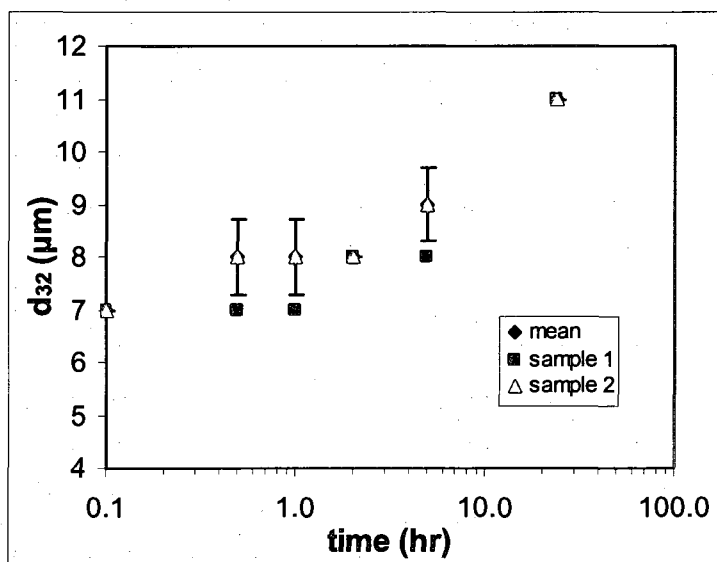


**Figure 5.23:** Brine-in-crude-oil-C Sauter diameters with 10 minutes of low mixing  $Re$  and applied shear after emulsification.

The transient drop size distributions for one of the samples are shown in Figure 5.24.

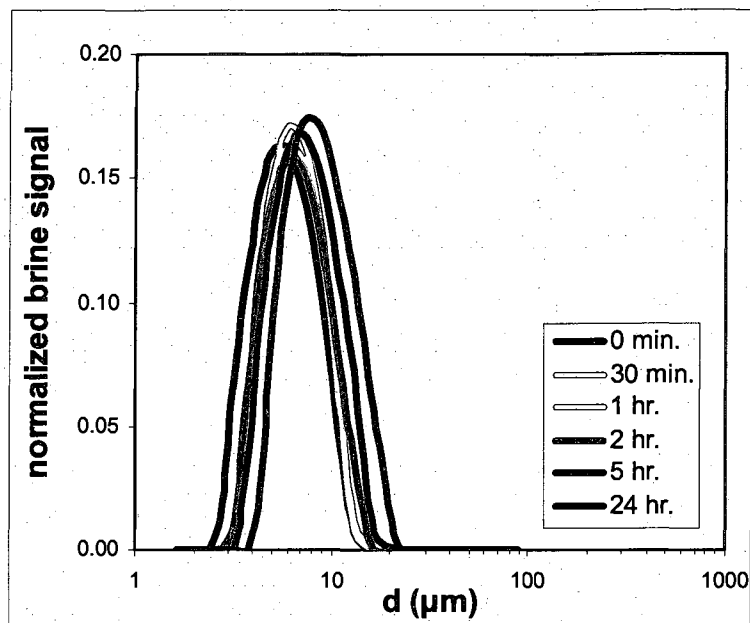


**Figure 5.24:** Brine-in-crude-oil-C drop size distributions with 10 minutes of low mixing  $Re$  and applied shear after emulsification.

The mixing conditions for 1 minute of mixing with applied shear are given in Table 5.10.

**Table 5.10:** Brine-in-crude-oil-C mixing conditions with 1 minute of low mixing  $Re$  and applied shear after emulsification.

sample #	$Re$	$N$ (rpm)	$P$ (W)	$E$ (kJ)
1	384	6549	85.5	5.1
2	359	6114	70.2	4.2

Even with 1 minute of low mixing, the emulsion was stable for 24 hours.



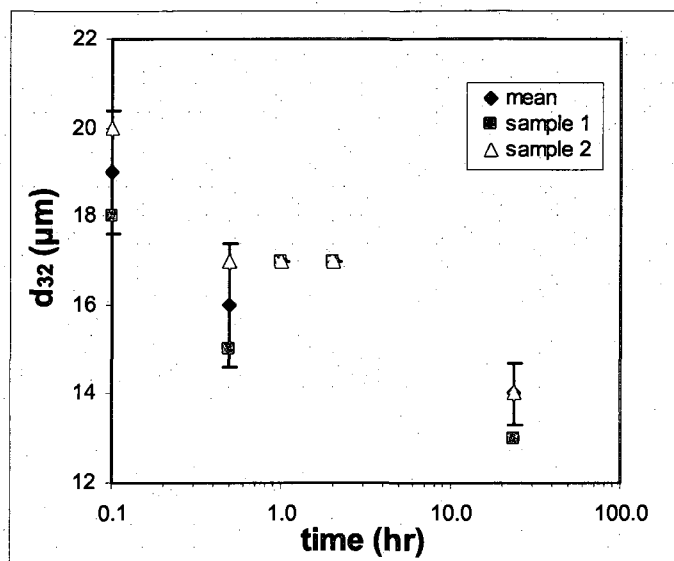


**Figure 5.25:** Brine-in-crude-oil-C Sauter diameters with 1 minute of low mixing  $Re$  and applied shear after emulsification.

The drop size distributions for one of the samples are given below.

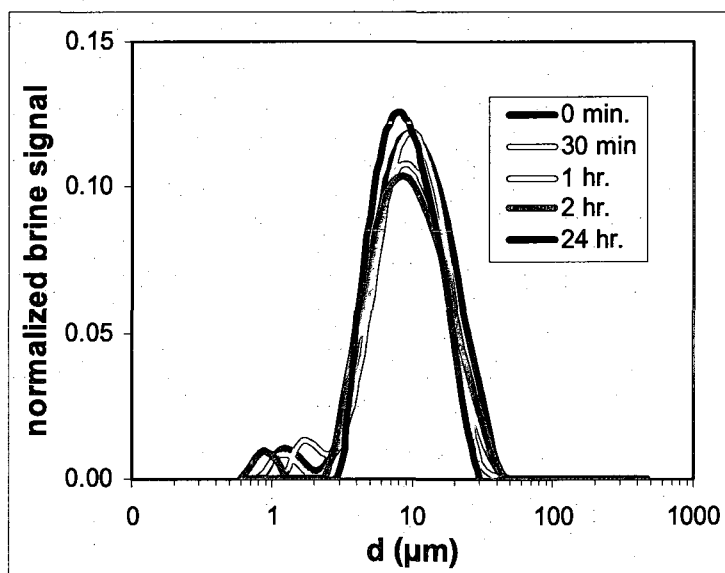
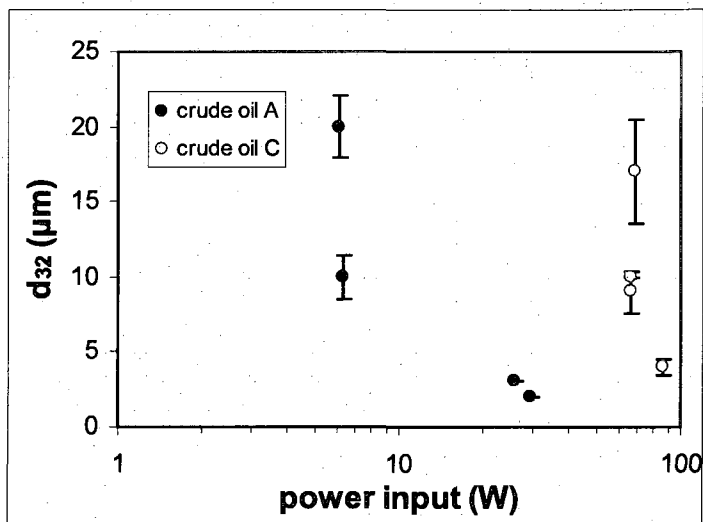


**Figure 5.26:** Brine-in-crude-oil-C drop size distributions with 1 minute of low mixing  $Re$  and applied shear after emulsification.

Using low Reynolds numbers of mixing in the brine-in-crude-oil-C emulsions with applied shear after emulsification produced emulsions that resisted coalescence throughout the duration of the experiments. The drop size distributions were not significantly affected by the application of mild shear after emulsification.

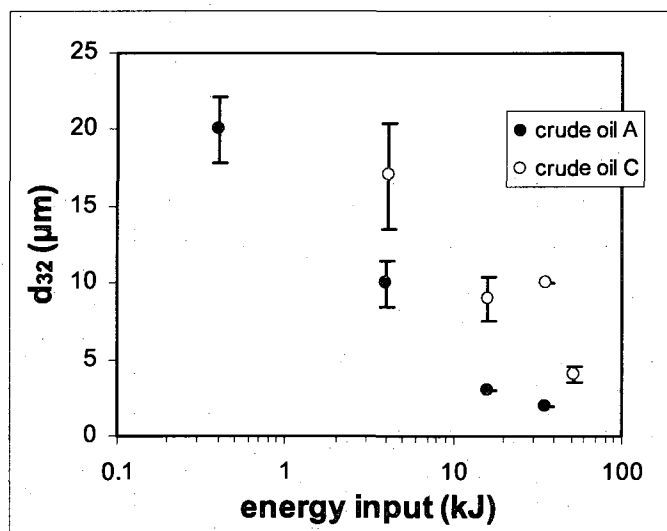
### 5.3.7 Effects of power and energy input

Figure 5.27 compares the effect of power input on the resulting mean diameter for each crude oil.



**Figure 5.27:** Average Sauter diameter as a function of power input.

More power was required for the brine-in-crude-oil-C emulsions to produce similar sized drops as those found in the brine-in-crude-oil-A emulsions. Multiplying the power input by the mixing time results in the energy required to form the emulsions.



**Figure 5.28:** Average Sauter diameter as a function of energy input.

### 5.3.8 Comparison to published correlations

The literature contains empirical predictions for drop size as a function of flow conditions for emulsions formed with Rushton turbines in turbulent flow.<sup>92-94, 96</sup>

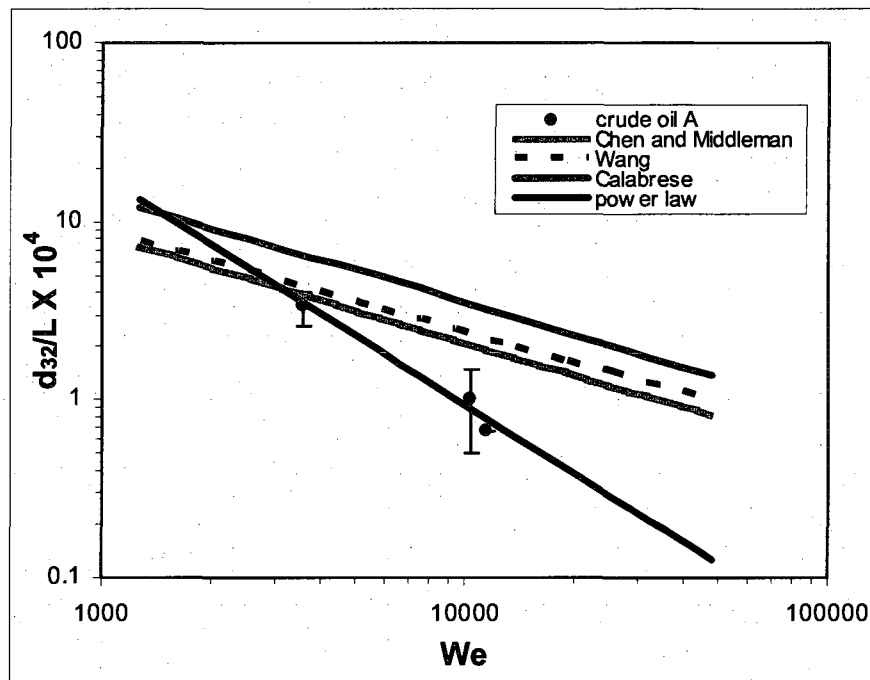


**Figure 5.29:** Comparison of experimental Sauter mean diameters for the crude oil A emulsions with correlations by Chen and Middleman,<sup>96</sup> Wang,<sup>94</sup> and Calabrese.<sup>93</sup>

The correlations by Chen and Middleman and Wang were developed for dilute systems in the absence of surfactant in turbulent flow formed by Rushton turbines in baffled tanks.

The correlation developed by Wang accounts for the viscosity of the dispersed phase.

The correlation developed by Calabrese accounts for the dispersed phase fraction, and it was developed for Rushton turbines in baffled tanks. However, it does not account for the presence of surfactant. The power law correlation was obtained by regressing the data with dependence on  $We$  as shown in Equation 5.12.

$$\frac{d_{32}}{L} = 12.4 We^{-1.28} \quad (5.12)$$

The deviation of the experimental data from the correlations at high Weber numbers could be caused by the inability of the correlations to account for dynamic interfacial tension effects that could lead to smaller drop sizes than predicted.

The volume weighted mean diameters of the crude oil A emulsions formed at high mixing speeds with the Rushton turbine were compared to the mean diameters of the crude oil A emulsions formed in Taylor-Couette flow as discussed in Chapter 4.

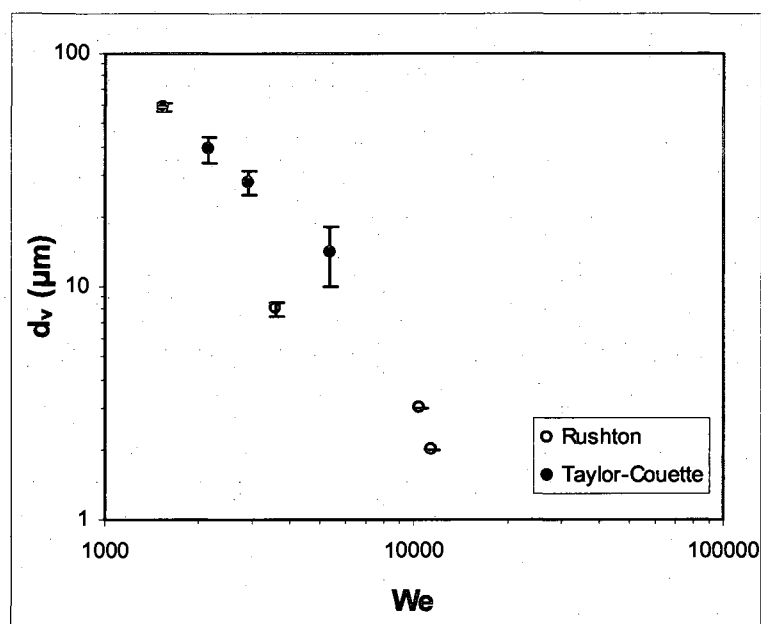


**Figure 5.30:** Comparison of mean drop sizes for brine-in-crude-oil-A emulsions formed with the Rushton turbine and Taylor-Couette flow.

Despite the different emulsification techniques and drop size measurement techniques, the mean diameters share similar dependence on  $We$ .

## 5.4 Conclusions

The drop size distributions of brine droplets in brine-in-crude-oil emulsions are sensitive to an assortment of parameters including mixing time, power input, crude oil viscosity, and interfacial properties.<sup>5</sup> These parameters not only affect emulsion formation, they also affect the transient stability of the emulsions. In this study, the mixing time, power input, and applied shear after emulsification were manipulated in order to observe their effects on the transient drop size distributions in brine-in-crude-oil emulsions.

The brine-in-crude-oil-A emulsions were stable at high values of  $Re$  ( $\sim 3000$ ) and ten minutes of mixing. With one minute of mixing, the emulsions were observed to be unstable 24 hours after formation. Applied shear after emulsification slightly reduced the drop size and reduced coalescence of the emulsions formed with 1 minute of mixing.

At low values of  $Re$  ( $\sim 400$ ), the brine-in-crude-oil-A emulsions displayed coalescence immediately after mixing, and applied shear after emulsification had no effect on the stability of the emulsions. At the same Reynolds number range of mixing ( $300 - 420$ ), the brine-in-crude-oil-C emulsions produced measurable drop sizes and resisted coalescence for the duration of the experiments. Application of shear after emulsification to the brine-in-crude-oil-C emulsions had little effect on the drop size distributions.

Significantly more power was required to produce stable emulsions in crude oil C than in crude oil A. The correlations developed by Wang, Chen and Middleman, and Calabrese over-predict the Sauter mean diameters. The mean diameters of the crude oil A emulsions formed with the Rushton turbine share similar dependence on  $We$  as those formed using Taylor-Couette flow.

## 5.5 Notation

$a, b$	empirical constants
$C$	constant
$d_i$	diameter of the $i^{\text{th}}$ bin ( $\mu\text{m}$ )
$d_{\text{max}}$	max. stable diameter ( $\mu\text{m}$ )
$d_v$	volume weighted mean diameter ( $\mu\text{m}$ )
$d_{32}$	Sauter diameter ( $\mu\text{m}$ )
$E$	energy input (kJ)
$f_i$	amplitude of the $i^{\text{th}}$ bin (a.u.)
$g$	gravitational constant ( $\text{m}^2/\text{s}$ )
$L$	impeller diameter (m)
$N$	rotational speed of impeller (rpm)
$N_p$	power number
$P$	power input (W)
$Re$	Reynolds number
$T_2$	transverse relaxation (ms)
$T_{2,\text{bulk}}$	bulk transverse relaxation (ms)
$T_{2,\text{DP},i}$	transverse relaxation of the dispersed phase of the $i^{\text{th}}$ bin (ms)
$T_{2,\text{lm}}$	log mean of transverse relaxation distribution (ms)
$V_i$	dimensionless viscosity group
$We$	Weber number
$\varepsilon$	energy dissipation rate (J/s)
$\sigma$	interfacial tension (mN/m)
$\rho$	surface relaxivity ( $\mu\text{m}/\text{s}$ )
$\rho_{CP}$	continuous phase density (g/mL)
$\rho_{DP}$	dispersed phase density (g/mL)
$\gamma$	rotational speed ( $\text{s}^{-1}$ )
$\mu_{CP}$	continuous phase viscosity ( $\text{Ns}/\text{m}^2$ )
$\mu_{DP}$	dispersed phase viscosity ( $\text{Ns}/\text{m}^2$ )
$\phi$	dispersed phase volume fraction

## **Chapter 6: Nuclear Magnetic Resonance Analysis of Gas Hydrate Formation in Water-in-Oil Emulsions**

### **6.1 Introduction**

Gas hydrates are clathrate compounds in which water is the host molecule and gas, such as methane, is the guest molecule.<sup>10</sup> The application to the oil and gas industry was made popular by Hammerschmidt in 1934.<sup>34</sup> Since that time, a significant amount of work has been performed to investigate the thermodynamic formation of gas hydrates in bulk systems.<sup>10</sup> However, water is typically dispersed in crude oil production environments, so the effect of the dispersed water must be considered.

Gas hydrate formation in water-in-crude-oil emulsions is a significant problem in the oil and gas industry.<sup>10, 98</sup> Knowledge about the morphology of the water drops before, during, and after hydrate formation will lead to improved mitigation of hydrate related problems. It has been shown in the literature that stable water-in-oil emulsions can potentially promote the successful transportation of gas hydrates.<sup>7, 12, 28</sup> Therefore, knowing the drop size distribution leads to a better understanding of the tendencies of the system to form plugs or transportable slurries. The drop size distribution also provides information regarding the exact hydrate morphology.

Traditional measurement techniques of drop size distributions and hydrate formation in water-in-crude-oil emulsions are difficult because of the pressure, temperature, and optical constraints. However, nuclear magnetic resonance (NMR) is a useful method to investigate these complicated systems because the measurements can be performed at high pressures, low temperatures, and they are not constrained by the optical properties of the sample.<sup>4</sup> In addition, gas hydrate formation in emulsified

systems can be directly measured using NMR.<sup>38</sup> Hence, one of the objectives of this chapter is to investigate, with the aid of NMR techniques, the relationship between drop size distributions and gas hydrate formation in two water-in-crude oil and two water-in-model oil emulsions. Another goal of this chapter is to elucidate probable morphology of gas hydrate particles that are formed in these emulsions as supported by the NMR data.

## **6.2 Experimental methods**

### **6.2.1 NMR techniques**

The Carr-Purcell-Meiboom-Gill (CPMG),<sup>43, 44</sup> pulsed field gradient with diffusion editing (PFG-DE),<sup>40, 46-48</sup> and rapid acquisition with relaxation enhancement (RARE)<sup>49, 65, 99</sup> were used to investigate the emulsion samples before and during hydrate formation in this work. The NMR pulse sequences for each technique and the details of each technique are provided in Chapter 2.

The CPMG technique was used to measure the  $T_2$  distributions of the samples. The correlation time of solid water is much greater than that of liquid water. Consequently, the transverse relaxation time of solid water is significantly reduced, and the solid water does not contribute to the overall  $T_2$  distribution when using the 2 MHz instrument described in this work. Therefore, the amount of liquid water converted to solid hydrate can be directly measured using the  $T_2$  distributions. The PFG-DE technique was used to measure the drop size distributions. The masking technique developed by Flaum<sup>46</sup> was used to determine the sensitivity of the parameters used in the PFG-DE measurements. The RARE technique was implemented to measure the one-dimensional spatial distribution of components in the system.<sup>49, 65</sup>



### 6.2.2 Fluid properties

Two crude oils and two model oils were investigated in this work. These are the same crude and model oils described in Chapter 4. The dispersed phase of the emulsions was distilled water. Ultra high purity methane with purity equal to 99.97% (Matheson Tri-Gas) was used in this work.

### 6.2.3 Sample preparation

The water-in-crude-oil emulsions were stabilized by the naturally occurring surfactants in the crude oils. The water-in-model-oil emulsions were stabilized using a commercially available nonionic surfactant (Span80, Sigma-Aldrich). This oil soluble surfactant was added to the model oils with concentration equal to 4 vol.% with respect to the volume of the model oils. For all experiments, this equated to the addition of 1.3 mL of Span80 to the model oil phase. This concentration was used because it provided sufficient emulsion stability over the duration of the experiments. The surfactant was dissolved in the model oils before the addition of distilled water. For all experiments, 8 mL distilled water was emulsified with 32 mL oil, thereby yielding a dispersed phase fraction equal to 0.2.

The emulsions considered in this work were prepared using a Taylor-Couette flow device. The rotating, inner cylinder was composed of Torlon with radius equal to 19.1 mm. The stationary, outer cylinder was composed of glass with radius equal to 21.6 mm. The fluids were sheared by this device for 10 minutes in each experiment. After emulsification, the emulsions were immediately transferred to a PEEK pressure vessel (Temco). The height of the cylindrical sample chamber is 4 cm and the radius is 1.5 cm.

Prior to this work, a suitable experimental setup was not available to perform these measurements on the 2 MHz spectrometer. Figure 6.1 shows a schematic of the experimental setup that was constructed for this work.

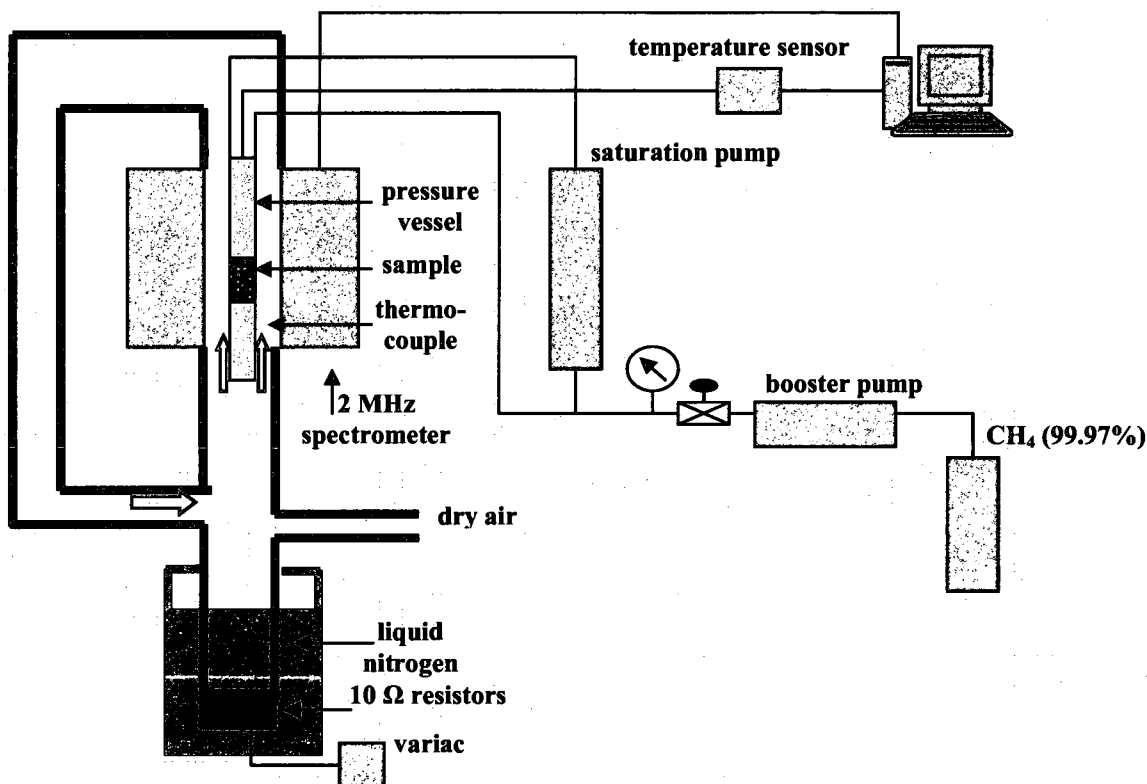


**Figure 6.1:** Schematic of the experimental setup (not drawn to scale).

The emulsion was placed in a cylindrical PEEK sample chamber with radius equal to 1.5 cm and height equal to 4 cm. The samples were saturated with ultra high purity methane gas at 6.2 MPa throughout the duration of the experiments except during measurements. Saturation was accomplished by bubbling methane gas through the emulsion sample at constant pressure. The samples were super-cooled by passing nitrogen gas in the annular region between the outside of the pressure vessel and the spectrometer probe wall. At milder temperatures, dry air was passed over the pressure vessel to control the sample temperature.

The temperatures of the samples were monitored using a fluoroptic temperature sensor (Lumasense) with precision equal to 0.1 K. Temperature measurements were performed using a bulk distilled water sample to test the homogeneity of temperature in the cylindrical sample chamber. The measurements were performed both in the center of the sample chamber and the wall of the sample chamber at different heights within the sample chamber. The wall is 1.5 cm away from the center. After the temperature in the system equilibrated, there existed a 0.8 K temperature gradient within the sample chamber in the vertical direction from the bottom of the sample chamber to the top. Figure 6.2 illustrates the deviation of temperature in the vertical direction in the pressure vessel.

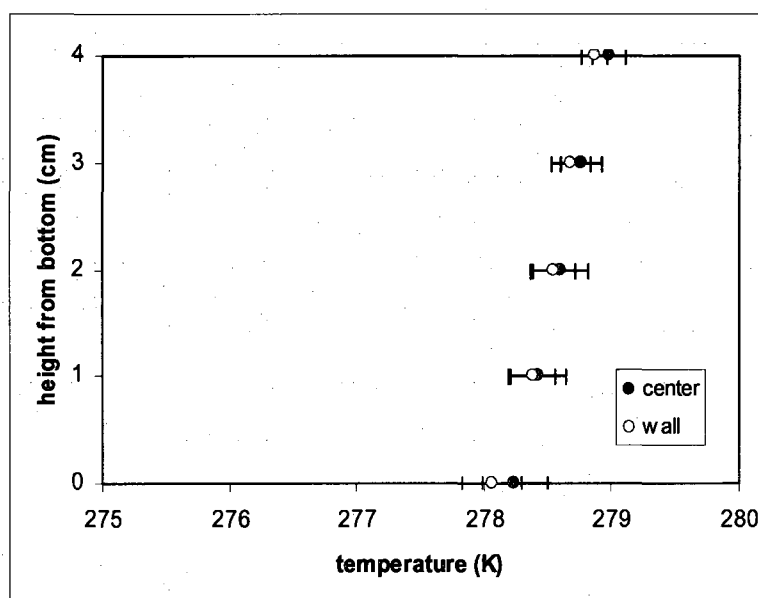


**Figure 6.2:** Deviation of temperature in the pressure vessel.

For all experiments, the temperature was measured in the center of the sample, so the overall precision of the temperature measurements is 0.5 K.

A typical experiment consisted of lowering the sample temperature to 277.2 K, over which time CPMG measurements were performed at different temperatures. The

sample temperature was then held at 277.2 K for at least twelve hours during which time the drop size distribution was measured. Because of time constraints, only one parameter set was used to perform the PFG-DE measurement, and those parameters are given in Table 6.1.

**Table 6.1:** Experimental parameters used for the PFG-DE measurements.

$\Delta$ (ms)	$\delta$ (ms)	gradient (G/cm)
508	39	1 – 40

The sample was then lowered to 231.2 K. The sample was then heated to 277.2 K, and the drop size distribution was measured. Several CPMG measurements were performed at intermediate temperatures between 277.2 K and the hydrate equilibrium temperature (281.7 K at 6.2 MPa).<sup>10</sup> Finally, the sample was heated above the hydrate equilibrium temperature and CPMG measurements were performed.

## **6.3 Results and discussion**

### **6.3.1 Water-in-crude-oil-A emulsion**

The water-in-crude-oil-A emulsion was formed by emulsifying the fluids in the Taylor-Couette cell using an inner cylinder rotational speed equal to 3,000 rpm for 10 minutes. The emulsion was subjected to a cooling/heating cycle in the range 303.2 K – 234.2 K with the pressure held constant at 6.2 MPa. Based on Stern et al.<sup>100</sup> and Fouconnier et al.,<sup>98</sup> it was expected that hydrate would form while passing through the ice melting point during the warming stage. Therefore, the fractional conversion of liquid water to solid hydrate was directly measured at 277.2 K which is above the ice melting point but below the hydrate dissociation temperature. The temperature of the sample was measured throughout the duration of the experiment.

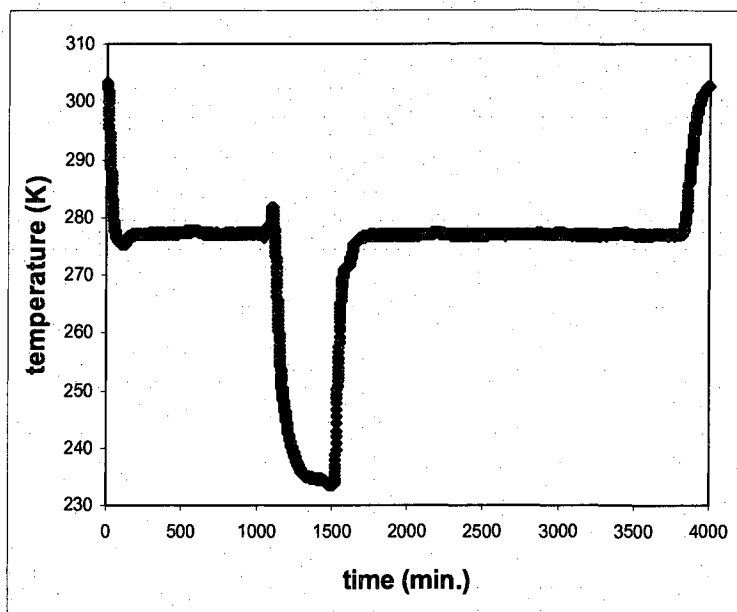


**Figure 6.3:** Temperature of the water-in-crude-oil-A emulsion.

Figure 6.4 shows a comparison between the  $T_2$  distribution of the emulsion before (cooling) and during (warming) methane hydrate formation.

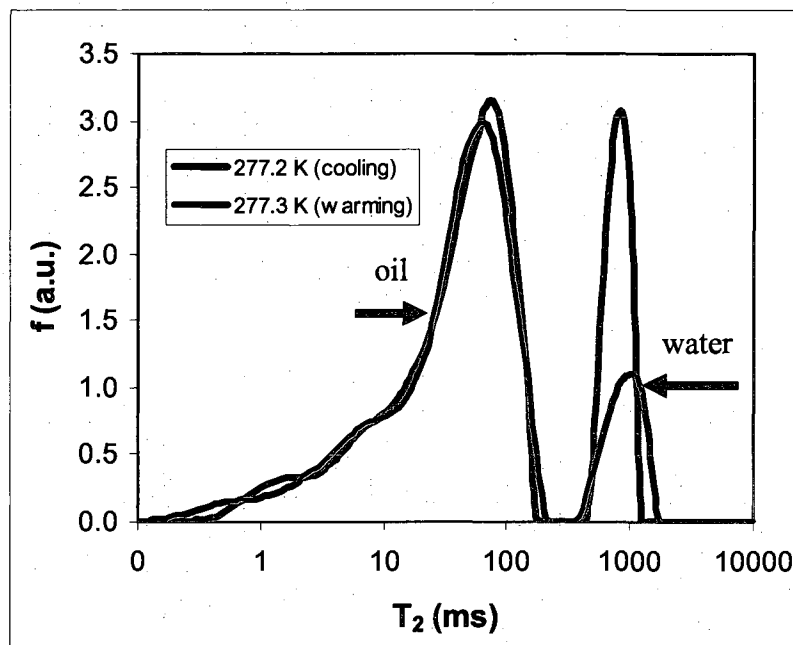


**Figure 6.4:** Comparison of  $T_2$  distributions of water-in-crude-oil-A emulsion during the cooling and warming stages. Note the decreased amplitude of the water distribution during the warming stage which indicates the presence of methane hydrate.

The water and oil peaks are clearly separable; therefore, the amount of liquid water at each temperature is calculated by summing the amplitude of the water peak. Thus, the fractional conversion of liquid water to solid hydrate is obtained by Equation 6.1.

$$x = 1 - \frac{\sum f_{\text{water, warming}}}{\sum f_{\text{water, cooling}}} \quad (6.1)$$

The fractional conversion of liquid water to methane hydrate is given by  $x$ , and  $f$  is the amplitude of the water signal obtained from the CPMG measurement with arbitrary units (a.u.).

The liquid water fraction, presented in Figure 6.5, is obtained by normalizing the magnetization of liquid water from the  $T_2$  distribution with respect to the calculated magnetization based on Curie's Law.<sup>53</sup>

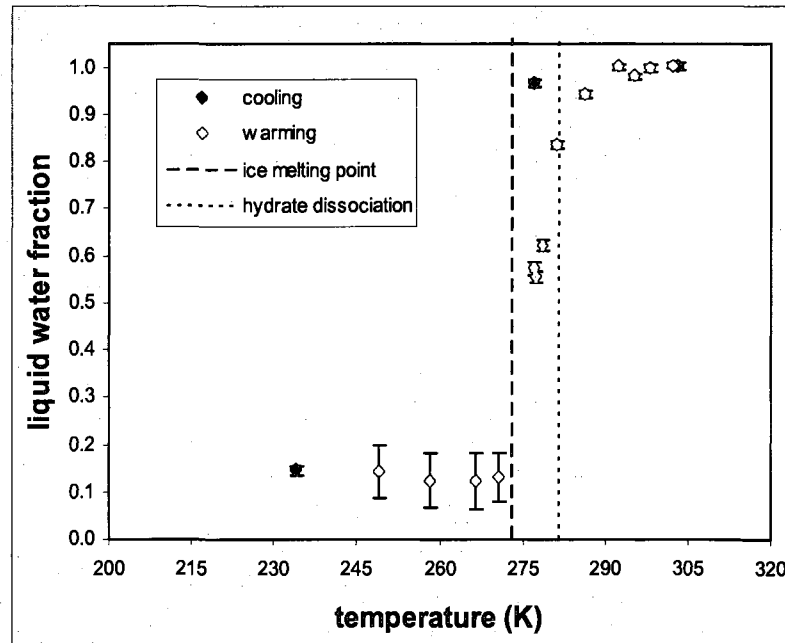


**Figure 6.5:** Liquid water fraction as a function of temperature for the water-in-crude-oil-A emulsion.

In this case, 45% of the liquid water that originally existed in the system at 277.2 K remained solid above the ice melting point, thereby indicating the presence of solid structure in the form of methane hydrate. Figure 6.6 shows the results for the control experiment without methane for a water-in-crude-oil-A emulsion.

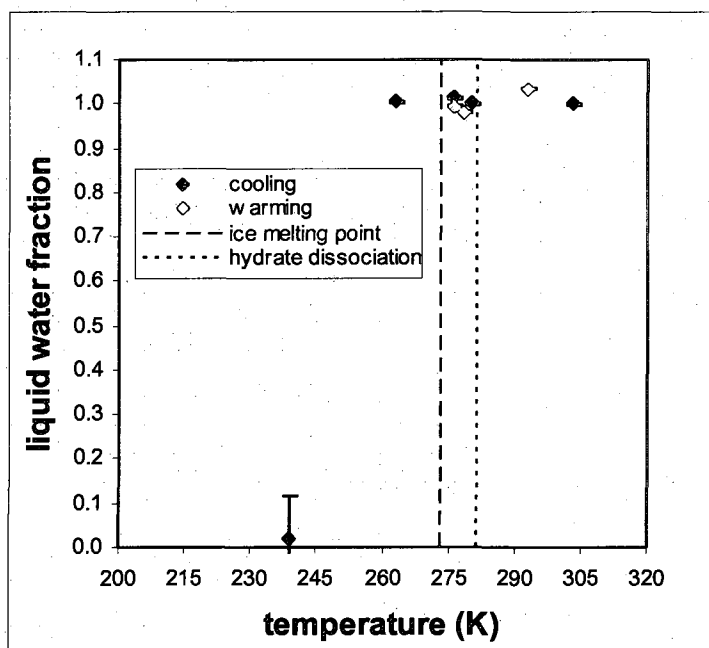


**Figure 6.6:** Control experiment without methane for a water-in-crude-oil-A emulsion.

Figure 6.6 shows the results of the control experiment using a water-in-crude-oil-A emulsion. The emulsion was prepared using an inner cylinder rotational speed equal to 3000 rpm. This experiment showed that no hydrate conversion was observed in the absence of methane.

The conversion of the liquid water to methane hydrate can also be observed using the RARE technique. For example, Figure 6.7 shows the one dimensional image taken at 277.2 K before hydrate formation.

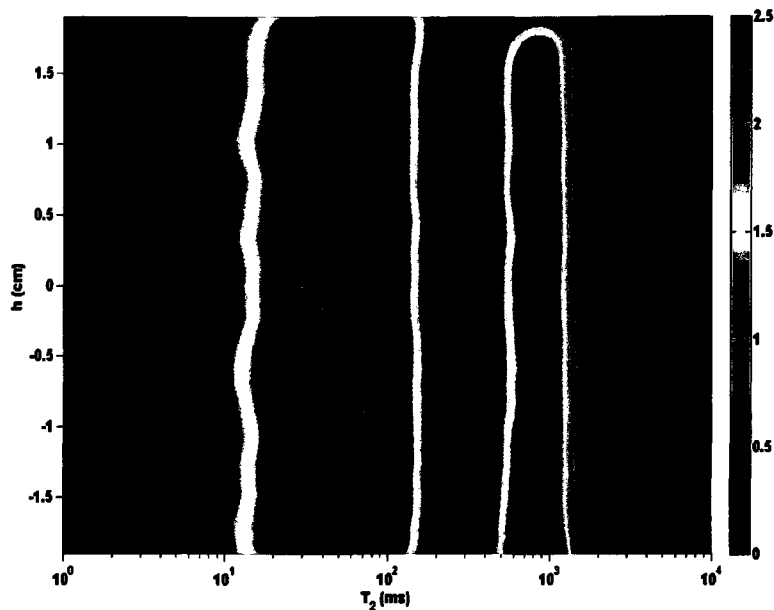


**Figure 6.7:** Vertical (one-dimensional) distribution of components in the pressure vessel for the water-in-crude-oil-A emulsion before hydrate formation (277.2 K, 6.2 MPa).

This measurement yields the spatial distribution of the components in the system. The height of the sample in centimeters is given by  $h$  and is shown on the y-axis. The center of the sample is located at  $h = 0.0$  cm. The x-axis represents  $T_2$ . Thus,  $T_2$  distributions are obtained throughout the height of the sample. The oil band is located on the left of the figure and centered at  $T_2 = 50$  ms. The water band is located on the right of the figure and centered at  $T_2 = 900$  ms. During the warming stage at 277.3 K, the intensity of the liquid water band decreased, as shown in Figure 6.8.



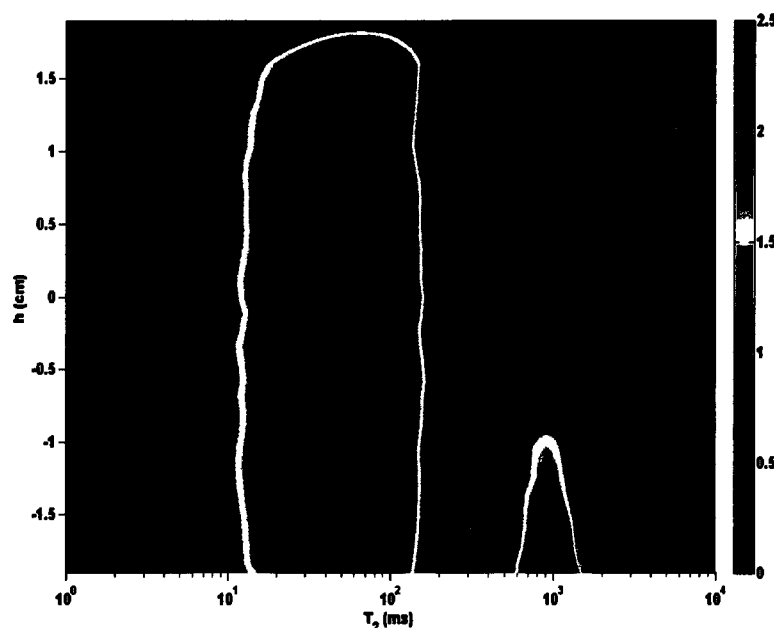


**Figure 6.8:** Vertical (one-dimensional) distribution of components in the pressure vessel for the water-in-crude-oil-A emulsion during hydrate formation (277.3 K, 6.2 MPa). Note the decrease in intensity of the water signal, thereby indicating the presence of methane hydrate.

Two mathematical models were constructed to predict the structure of the water drops during methane hydrate formation. The first model, referred to as the threshold model, assumes the complete conversion of a fraction of the water drops to methane hydrate. This model is based on an assumed sequence of events. The first assumption is that only the largest droplets will experience nucleation events which will convert them completely to ice.<sup>101, 102</sup> Upon warming, only ice will convert to hydrate, and it will convert completely to hydrate. Figure 6.9 illustrates the threshold model for a synthetic drop size distribution with mean diameter equal to 10  $\mu\text{m}$ .

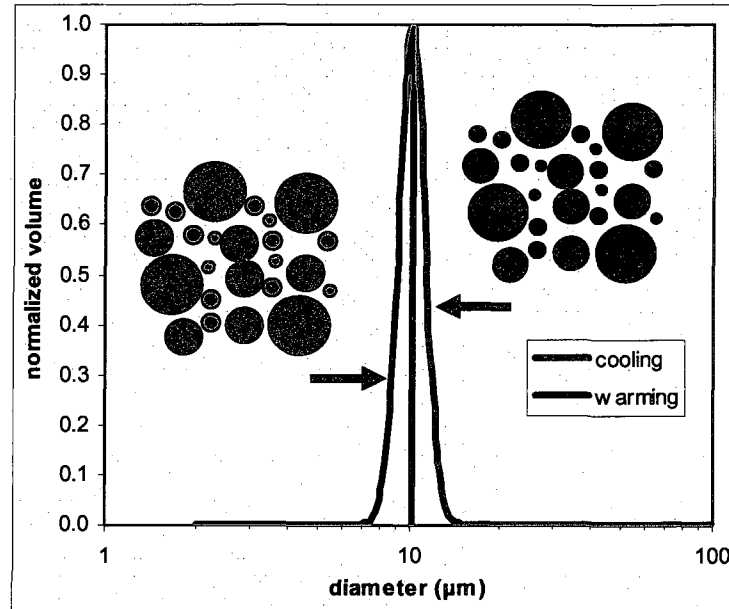


**Figure 6.9:** Illustration of the threshold model. The cooling curve is a lognormal distribution with mean diameter equal to  $10\ \mu\text{m}$ . The warming curve is generated by assuming that 45% of the liquid water volume, starting with the largest drops, completely converts to hydrate. Note that the cooling and warming curves are identical at the lower end of the distribution.

The larger hydrated drops (black) are accompanied by smaller liquid water drops (blue) that do not freeze. In this example, 45% of the total volume, starting with the largest diameter drops and continuing toward smaller diameters, were assumed to be completely frozen and subsequently converted to hydrate. The initial distribution, referred to as the cooling curve, is truncated based on the hydrate conversion. The resulting distribution is shown in Figure 6.7, denoted as the warming curve.

The second model, referred to as the shell model,<sup>10</sup> assumes that hydrate forms as shells around the exterior of the water drops. The shells are assumed to form with constant thickness as would be expected from a diffusion limited reaction. Figure 6.10 shows an example of the shell model with 45% hydrate conversion for a synthetic drop size distribution with mean diameter equal to  $10\ \mu\text{m}$ .

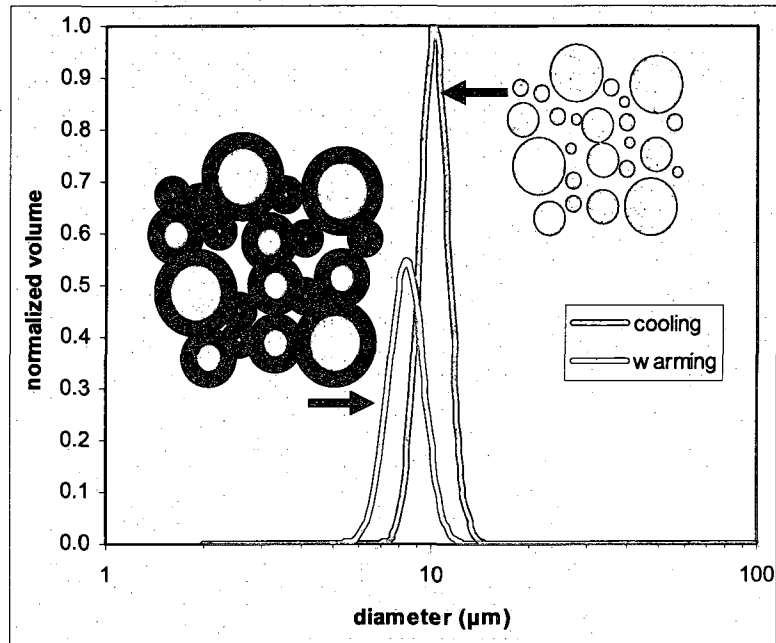


**Figure 6.10:** Illustration of the shell model. The cooling curve is a lognormal distribution with mean diameter equal to 10  $\mu\text{m}$ . The warming curve is generated by assuming that a constant thickness hydrate shell forms on the drops to yield 45% hydrate conversion.

Note that the shell model predicts a shift and decrease in amplitude of the drop size distribution as opposed to the truncation predicted by the threshold model.

The threshold model predicted that the distribution of larger drops would be truncated as a result of hydrate formation, as shown in the drop size distributions in Figure 6.11.

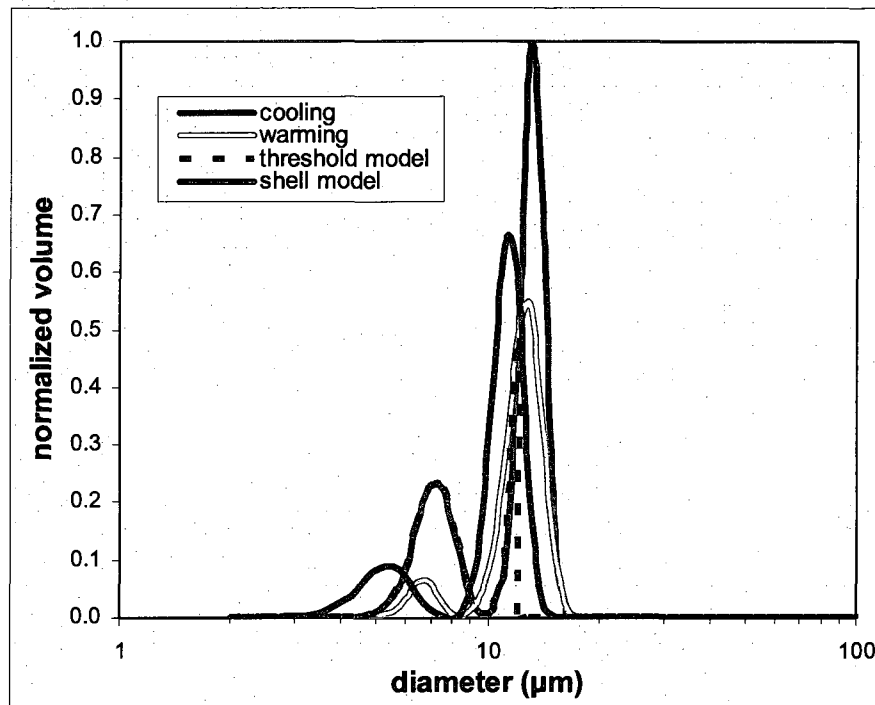


**Figure 6.11:** Comparison of the threshold and shell models to the drop size distributions of the water-in-crude-oil-A emulsion.

The truncation limit was determined according to the 45% hydrate conversion that was obtained from the CPMG measurement. Note that the threshold model follows exactly the cooling drop size distribution up until the threshold diameter. Figure 6.11 also illustrates the shell model prediction. Note that the shell model predicts a full distribution rather than the truncated distribution predicted by the threshold model. The shell model is calculated based on the fractional conversion of liquid water to solid hydrate as obtained from the CPMG technique. The volume associated with each drop size bin is adjusted by the shell thickness until the volumetric fractional conversion is equal to the conversion obtained from the CPMG technique. The shell thickness for this system was calculated to be 1  $\mu\text{m}$ . To evaluate the predictive ability of each model, the error was calculated.<sup>103</sup>

$$\varepsilon = \sum_{i=1}^n \left( f_i - \hat{f}_i \right)^2 \quad (6.2)$$

The experimental and model drop size distributions were fit to Gaussian curves to facilitate the error calculations. The amplitude of the experimental drop size distributions is  $f_i$  while the amplitude of the predicted drop size distributions is  $\hat{f}_i$ . The error for the shell model was equal to 0.48 while the threshold model resulted in an error equal to 0.56. Therefore, it was concluded that the shell model provided a better fit to the experimental drop size distribution during hydrate formation than the threshold model. The volume weighted mean diameters were calculated according to Equation 6.3.

$$d_v = \frac{\sum_{i=1}^n d_i f_i V_i}{\sum_{i=1}^n f_i V_i} \quad (6.3)$$

$V_i$  is the volume associated with each bin size of the drop size distribution, and  $f_i$  is the amplitude obtained from NMR. This formulation of the mean diameter accurately reflects the volumetric sensitivity of NMR measurements. Table 6.2 shows a summary of the experimental and model mean diameters for this emulsion.

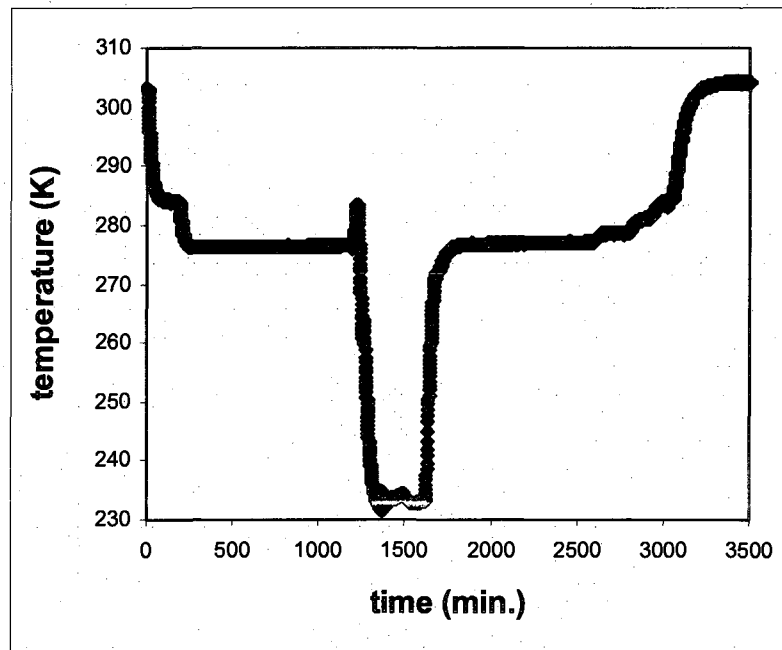
**Table 6.2:** Comparison of experimental and predicted mean diameters for the water-in-crude-oil-A emulsion.

	$d_v$ ( $\mu\text{m}$ )
<b>cooling</b>	7, 13
<b>warming</b>	7, 13
<b>shell</b>	7, 12
<b>threshold</b>	5, 11

This analysis indicates that the overall drop size distribution is critical for determining morphological features about the water droplets during methane hydrate formation.

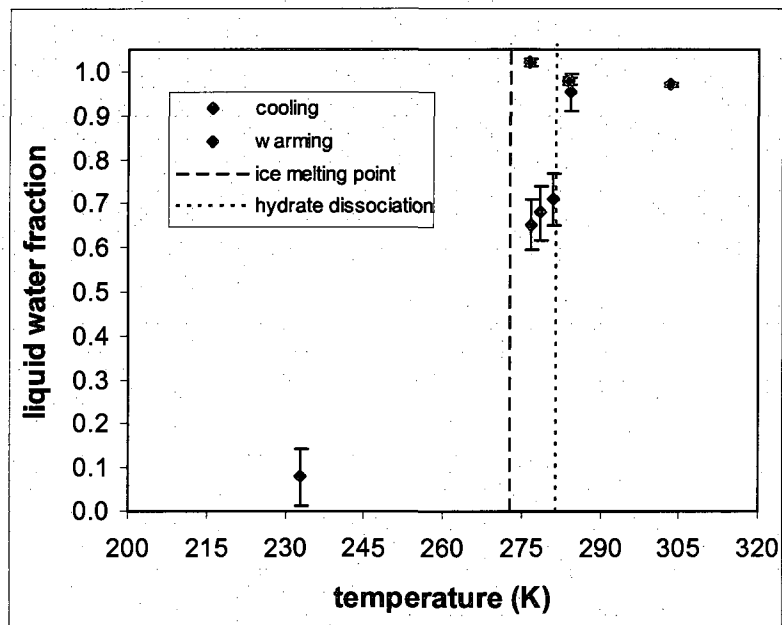
### 6.3.2 Water-in-model-oil-A emulsion

The water-in-model-oil-A emulsion was formed by emulsifying water in the model oil A using the Taylor-Couette cell with an inner cylinder rotational speed equal to 3,000 rpm for 10 minutes. The sample temperature throughout the duration of the experiment is given in Figure 6.12.



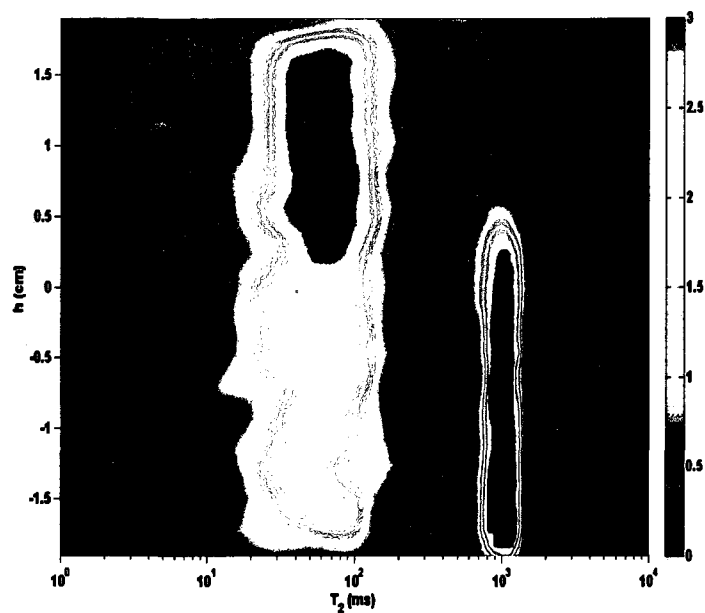
**Figure 6.12:** Sample temperature of the water-in-model-oil-A emulsion.

Figure 6.13 depicts the liquid water fraction as a function of temperature, showing that 35% hydrate conversion was achieved.



**Figure 6.13:** Liquid water fraction as a function of temperature for the water-in-model-oil-A emulsion.

To further illustrate hydrate formation, the one dimensional images before and during hydrate formation are given in Figure 6.14 and Figure 6.15.



**Figure 6.14:** Vertical (one-dimensional) distribution of components in the pressure vessel for the water-in-model-oil-A emulsion before hydrate formation (276.5 K, 6.2 MPa).

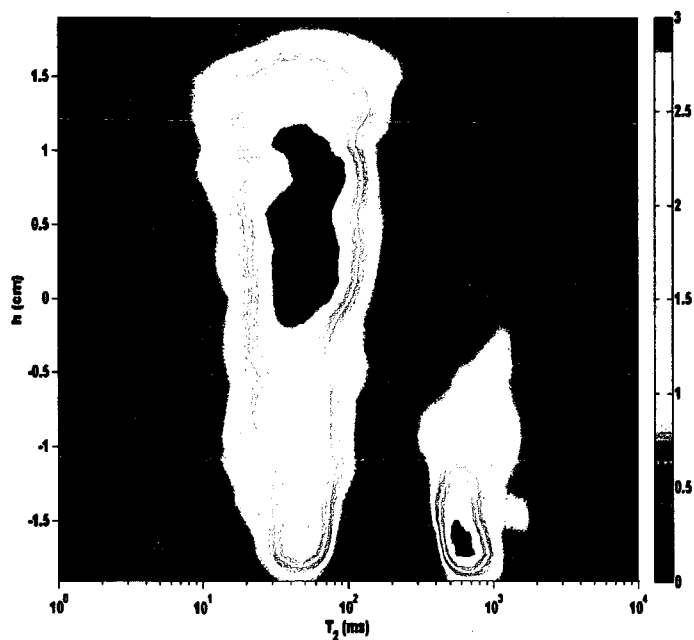


**Figure 6.15:** Vertical (one-dimensional) distribution of components in the pressure vessel for the water-in-model-oil-A emulsion during hydrate formation (277.0 K, 6.2 MPa).



Figure 6.14 was obtained at 276.5 K during the cooling stage of the experiment, while Figure 6.15 was obtained at 277.0 K during the warming stage of the experiment. Figure 6.15 shows the decrease in intensity of the water signal as well as sedimentation of the water drops.

The threshold and shell model comparisons to the experimental distributions are given in Figure 6.16.

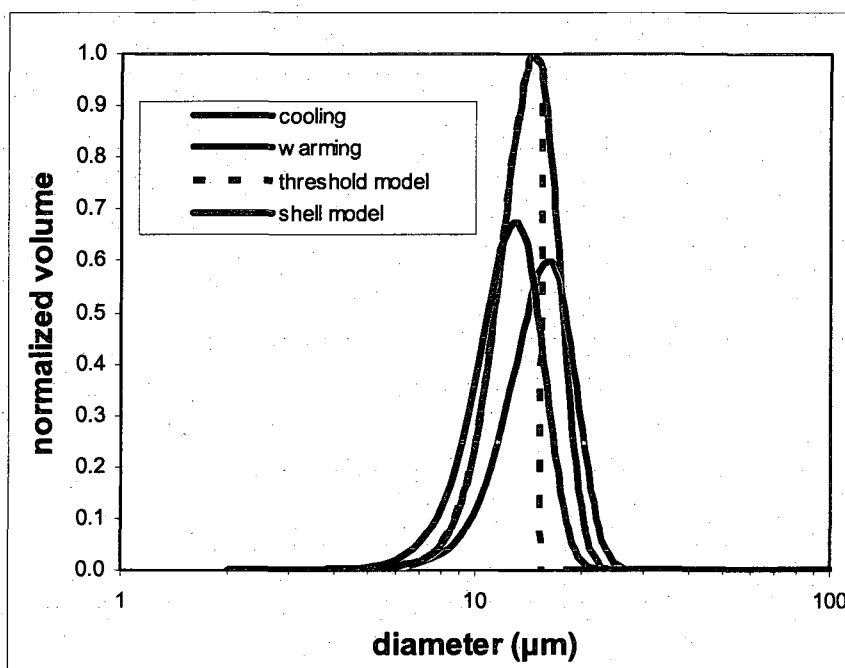


**Figure 6.16:** Comparison of the threshold and shell models to the drop size distributions of the water-in-model-oil-A emulsion.

The mean diameters for this emulsion are provided in Table 6.3.

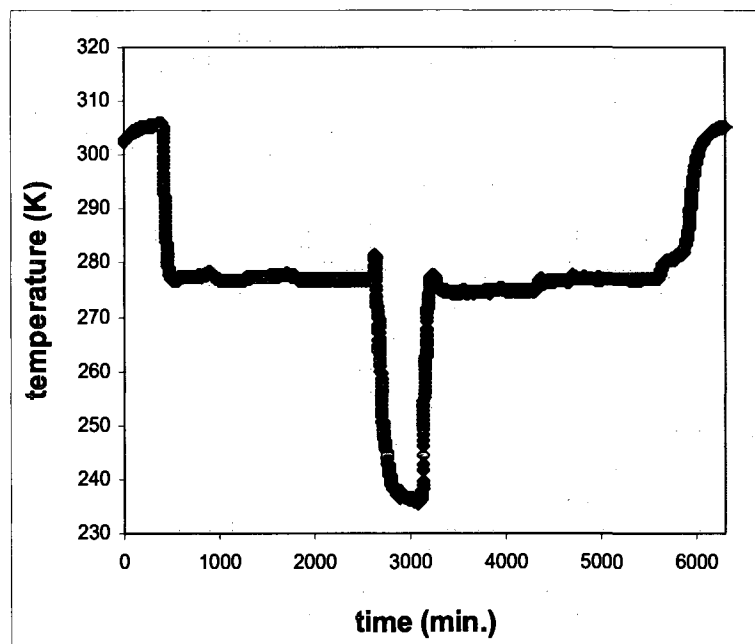
**Table 6.3:** Comparison of experimental and predicted mean diameters for the water-in-model-oil-A emulsion.

	$d_v$ (μm)
<b>cooling</b>	14
<b>warming</b>	15
<b>shell</b>	12
<b>threshold</b>	13

The threshold model predicted that the final mean diameter would be 13  $\mu\text{m}$  after truncating 35% of the volume from the largest drops. The shell model predicted that with 35% conversion, the mean diameter would be 12  $\mu\text{m}$  with a hydrate shell thickness equal to 1  $\mu\text{m}$ . The error for the shell model was 0.88 while the threshold model yielded an error equal to 1.58. Therefore, it was concluded that the shell model provides a better representation of the drop size distribution during methane hydrate formation than the threshold model.

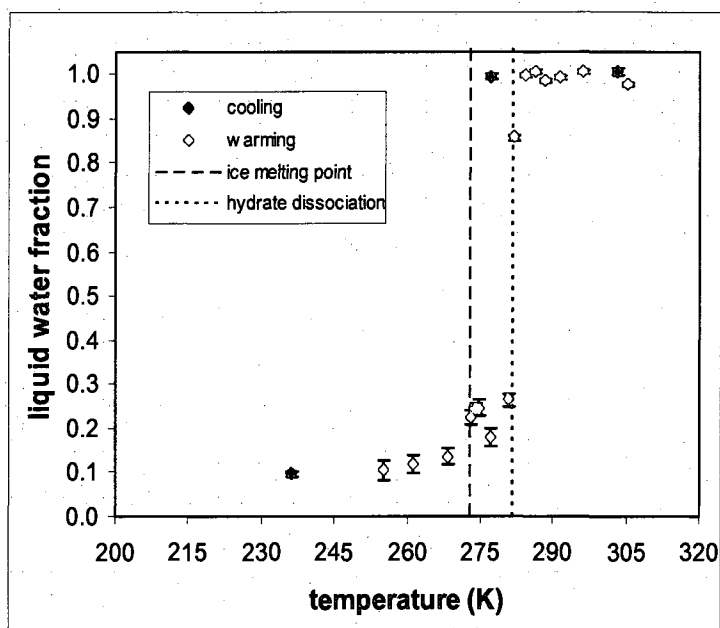
### 6.3.3 Water-in-crude-oil-C emulsion

The water-in-crude-oil-C emulsion was formed using an inner cylinder rotational speed equal to 2,000 rpm for 10 minutes in the Taylor-Couette cell. The sample temperature throughout the duration of the experiment is given in Figure 6.17.



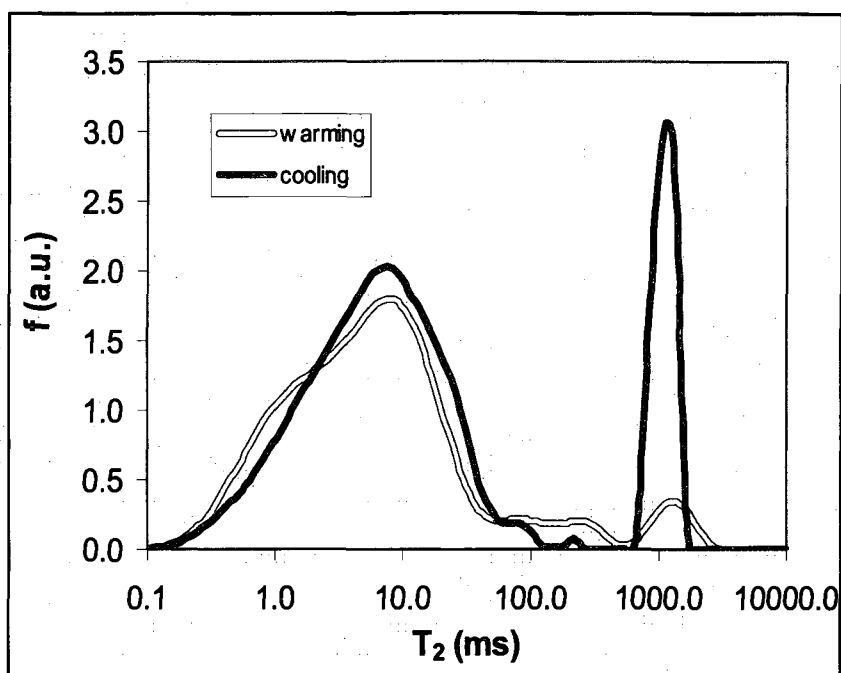
**Figure 6.17:** Sample temperature of the water-in-crude-oil-C emulsion.

Figure 6.18 shows the water fraction as a function of temperature, illustrating that 82% hydrate conversion was achieved.



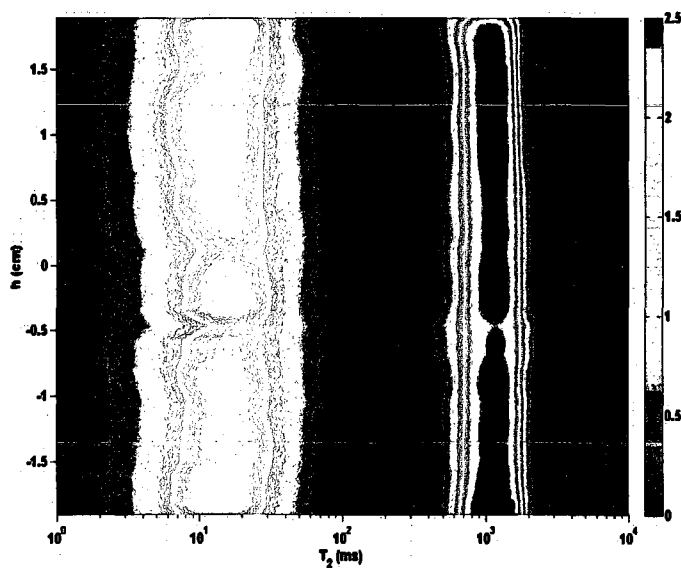
**Figure 6.18:** Liquid water fraction as a function of temperature for the water-in-crude-oil-C emulsion.

Figure 6.19 shows a comparison between the  $T_2$  distributions during cooling and warming at 277.0 K.



**Figure 6.19:** Comparison of  $T_2$  distributions during the cooling and warming stages.

The conversion of water to hydrate is further illustrated in Figure 6.20 and Figure 6.21.



**Figure 6.20:** Vertical (one-dimensional) distribution of components in the pressure vessel for the water-in-crude-oil-C emulsion before hydrate formation (277.0 K, 6.2 MPa).

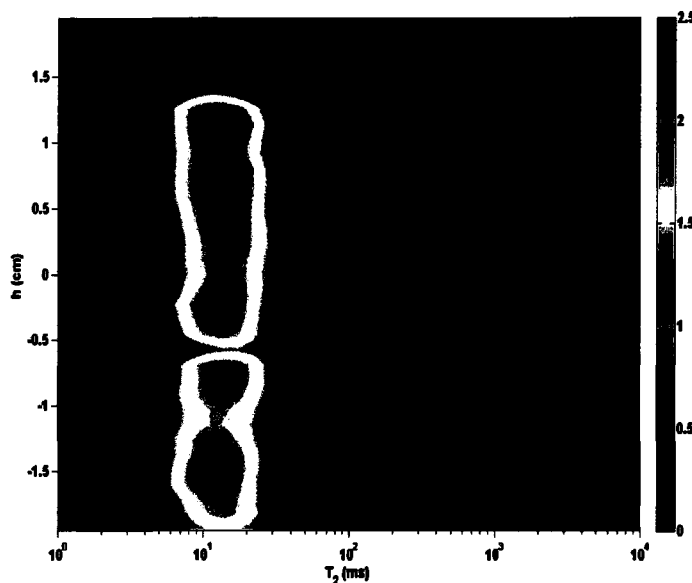


**Figure 6.21:** Vertical (one-dimensional) distribution of components in the pressure vessel for the water-in-crude-oil-C emulsion during the warming stage (277.0 K, 6.2 MPa).

At the same temperature (277.0 K), the liquid water intensity decreased by 82% during hydrate formation.

With 82% of the original liquid water converted to hydrate, the signal of the remaining water was obscured by the noise and could not be unambiguously assigned to drop sizes when performing the PFG-DE measurement during the warming stage at 277.0 K. This shows that with the liquid water fraction equal to 0.04, the drop size distribution could not be resolved using the PFG-DE technique. Both the threshold and shell models were analyzed, and the comparisons are shown in Figure 6.22.

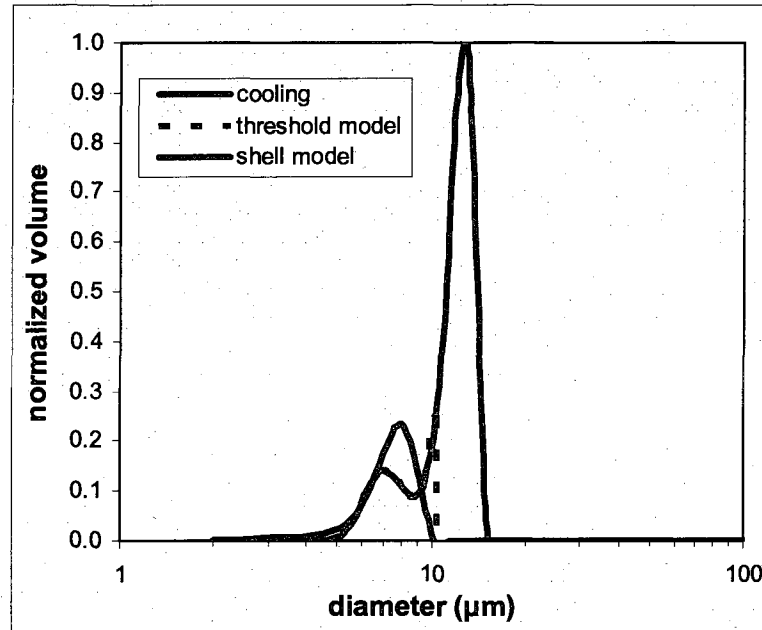


**Figure 6.22:** Comparison of the threshold and shell models to the drop size distributions of the water-in-crude-oil-C emulsion.

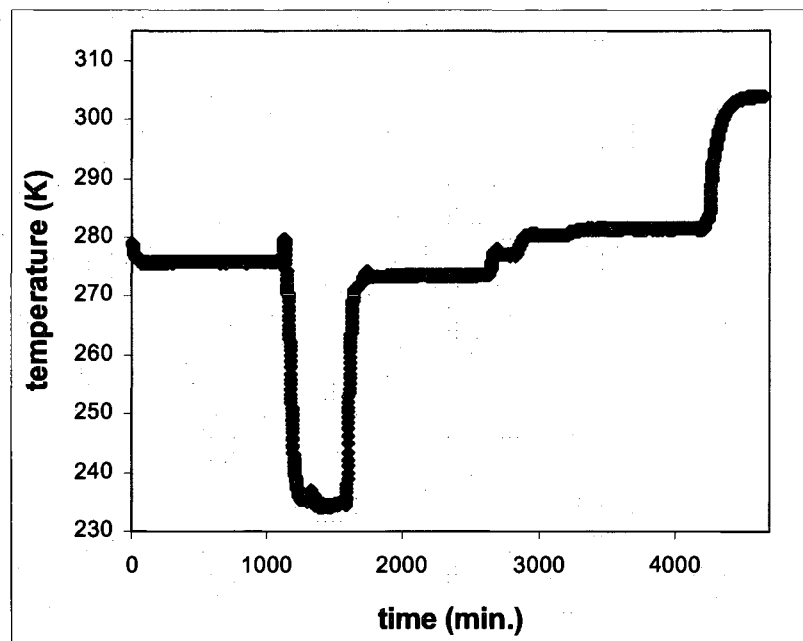
The threshold model predicted that the population of large drops would be truncated, and the population of smaller drops would have a mean diameter equal to 8  $\mu\text{m}$ . The shell model predicted the formation of a 3  $\mu\text{m}$  shell, thereby resulting in the conversion of most of the smaller diameter peak and a decrease in drop size of the larger diameter peak to a mean diameter of 9  $\mu\text{m}$ . A summary of these results is provided in Table 6.4.

**Table 6.4:** Comparison of experimental and predicted mean diameters for the water-in-crude-oil-C emulsion. In the warming cycle, the drop size distribution could not be measured due to the high noise level of the measurement.

	$d_v$ ( $\mu\text{m}$ )
<b>cooling</b>	11
<b>warming</b>	-
<b>shell</b>	7
<b>threshold</b>	8

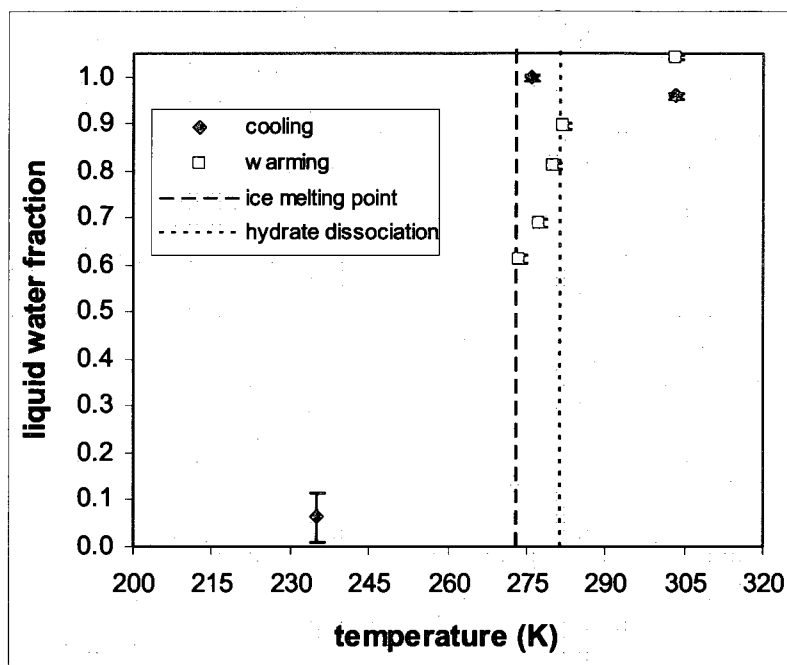
#### 6.3.4 Water-in-model-oil-B emulsion

The water-in-model-oil-B emulsion was formed using an inner cylinder rotational speed equal to 1500 rpm for 10 minutes in the Taylor-Couette cell. The addition of 4 vol. % Span80 to the model oil B resulted in an emulsion with viscosity such that the maximum inner cylinder rotational speed was 1500 rpm. The temperature throughout the duration of the experiment is given in Figure 6.23.



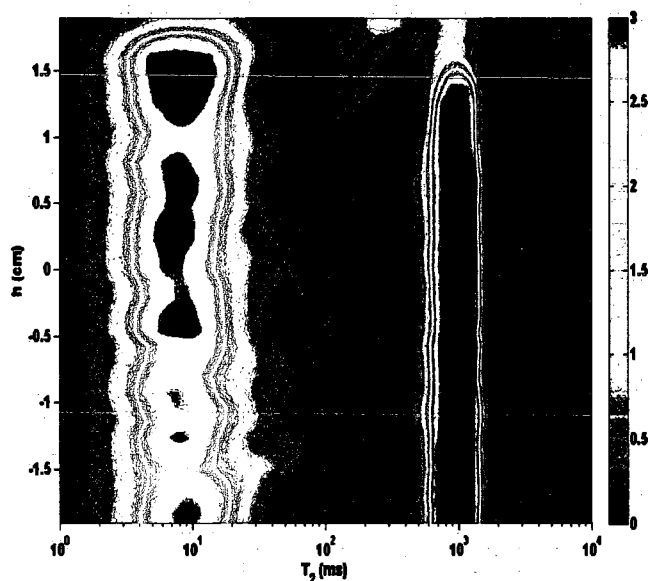
**Figure 6.23:** Sample temperature for the water-in-model-oil-B emulsion.

This system exhibited 31% hydrate conversion, as shown in Figure 6.24.



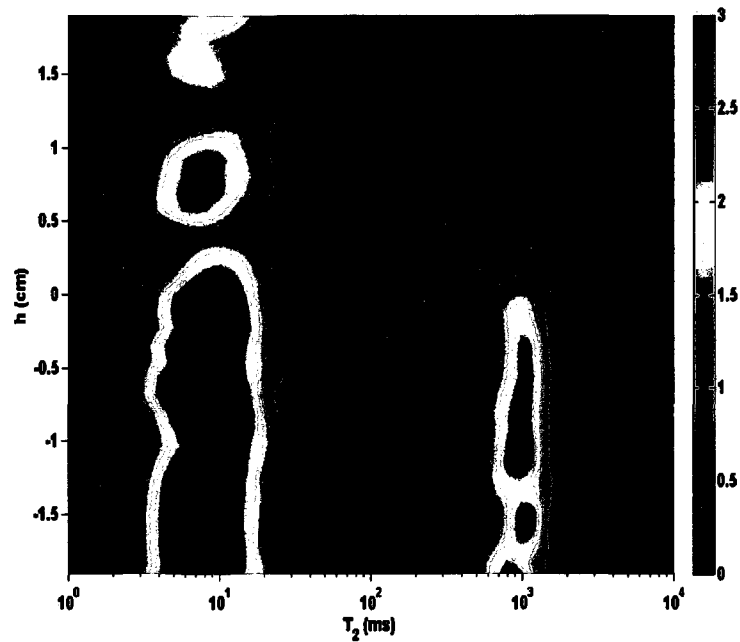
**Figure 6.24:** Liquid water fraction as a function of temperature for the water-in-model-oil-B emulsion.

Figure 6.25 and Figure 6.26 further illustrate the conversion of liquid water to hydrate.



**Figure 6.25:** Vertical (one-dimensional) distribution of components in the pressure vessel for the water-in-model-oil-B emulsion before hydrate formation (275.8 K, 6.2 MPa).





**Figure 6.26:** Vertical (one-dimensional) distribution of components in the pressure vessel for the water-in-model-oil-B emulsion during the warming stage (277.0 K, 6.2 MPa).

Figure 6.27 illustrates the experimental comparisons to the threshold and shell model predictions.

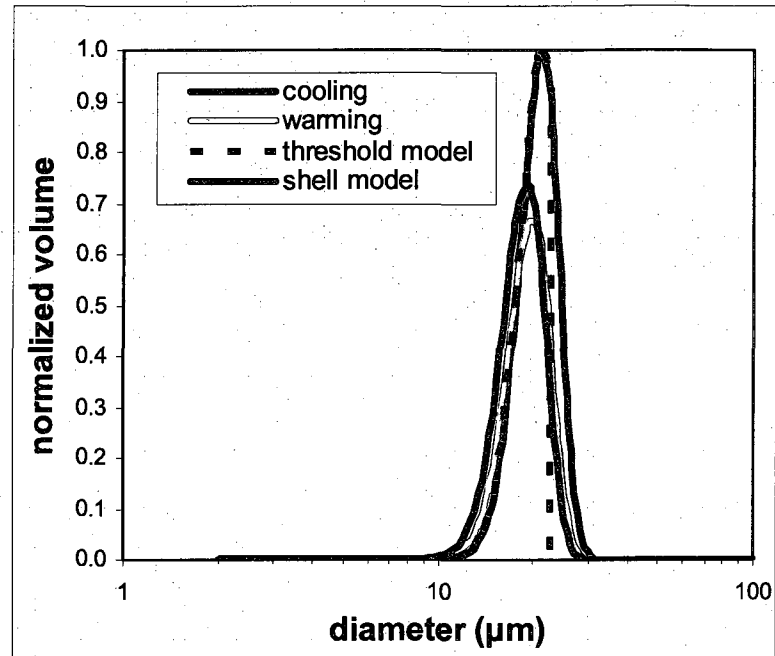


**Figure 6.27:** Comparison of the threshold and shell models to the drop size distributions of the water-in-model-oil-B emulsion.

The mean diameters are tabulated in Table 6.5.

**Table 6.5:** Comparison of experimental and predicted mean diameters for the water-in-model-oil-B emulsion.

	$d_v$ ( $\mu\text{m}$ )
<b>cooling</b>	21
<b>warming</b>	19
<b>shell</b>	19
<b>threshold</b>	20

The error for the shell model was 0.08 while the error for the threshold model was 0.44.

The shell thickness for this emulsion was determined to be 1  $\mu\text{m}$ . Compared to the threshold model, the shell model is most representative of the drop size distribution during methane hydrate formation for this system.

## 6.4 Conclusions

This chapter has shown the effectiveness of using nuclear magnetic resonance to directly measure methane hydrate formation in water-in-oil emulsions. Specifically, the drop size distributions and transverse relaxation data are combined to yield quantitative information about the relationship between drop size distributions and methane hydrate formation. The water-in-crude-oil-A, water-in-model-oil-A, and water-in-model-oil-B emulsions indicate that the shell model is more representative of methane hydrate formation than the threshold model. In addition, no hydrate formation was observed before ice formation in these systems. The hydrate equilibrium in the dispersed systems in this work is consistent with hydrate equilibrium in bulk systems.

The water-in-crude-oil-C emulsion yielded significantly higher hydrate conversion than the other emulsions, such that a drop size distribution measurement could not be performed during hydrate formation due to noise constraints. This enhanced hydrate formation in the water-in-crude-oil-B emulsion is likely due to the complex interfacial effects at the water-oil interfaces that may promote hydrate formation in the crude oil C emulsions.

## 6.5 Notation

$d_i$	diameter associated with the $i^{\text{th}}$ bin ( $\mu\text{m}$ )
$d_v$	volume weighted mean diameter ( $\mu\text{m}$ )
$f_i$	amplitude associated with the $i^{\text{th}}$ bin of either the $T_2$ or drop size distributions (a.u.)
$h$	vertical height of sample (cm)
$T_2$	transverse relaxation (ms)
$V_i$	volume associated with each drop size bin ( $\mu\text{m}^3$ )
$x$	fractional conversion
$\Delta$	gradient spacing (ms)
$\delta$	gradient duration (ms)
$\varepsilon$	error sum of squares

## **Chapter 7: Significant Contributions and Future Work**

### ***7.1 Significant Contributions***

This thesis focuses on the characterization of water-in-oil emulsions with specific application to methane hydrate formation in water-in-oil emulsions. Unique data is provided by this thesis for emulsion and methane hydrate formation in black oil emulsions. This thesis introduces a novel application of the PFG-DE NMR technique to measure polydisperse drop size distributions of water-in-oil emulsions. The PFG-DE technique agrees with the established PFG technique for unimodal emulsions. The PFG-DE technique greatly improves the characterization of multimodal drop size distributions by not assuming a form of the drop size distribution.

Data is presented for concentrated emulsion formation in the presence of surfactants in well defined Taylor-Couette shear fields. This work is important because drop size distributions are directly measured in both model and crude oils. Computational fluid dynamics simulations combined with the experimental data provide insight about the effect of flow field on emulsion formation. For the low viscosity oils, Taylor vortices lead to increased multimodal drop size distributions at high inner cylinder rotational speeds. For the more viscous oils, the flow field is simple shear for all inner cylinder rotational speeds. However, the crude oil C displays multimodal drop size distributions for all shear rates while the model oil B displays broad, unimodal drop size distributions. The drop sizes of the low viscosity oils qualitatively agree with the drop size prediction developed by Janssen.

This thesis contains transient drop size distributions for emulsions formed in complex shear fields using a Rushton turbine. These transient studies show that at the

same Reynolds number of mixing, the more viscous crude oil produces stable emulsions while the less viscous crude oil produces unstable emulsions. Significantly more power is required to produce emulsions in the more viscous crude oil than the less viscous oil. The data deviates from correlations by Chen and Middleman, Wang, and Calabrese for mean diameter as a function of Weber number in turbulent flow.

A new experimental setup was constructed that facilitates methane hydrate measurements in water-in-oil emulsions. Therefore, NMR measurements can now be performed on the 2 MHz spectrometer at high pressures and low temperatures. For the first time, the PFG-DE technique in conjunction with the CPMG technique was implemented to directly measure drop size distributions in water-in-oil emulsions during methane hydrate formation. No hydrate formation was observed before ice formation in these systems. The hydrate equilibrium in the dispersed systems in this work is consistent with hydrate equilibrium in bulk systems. For three of the four oils investigated, hydrate forms shells around the exterior of the drops with thickness approximately equal to 1  $\mu\text{m}$ .

## **7.2 Future Work**

The research fields of concentrated emulsion formation in the presence of surfactants and methane hydrate formation offer significant future challenges and opportunities. Performing emulsion and methane hydrate measurements in flowing systems represents the most important next step for flow assurance research related to emulsions and methane hydrates. NMR measurements should be performed to directly capture the dynamic properties of flowing systems including drop size and transverse relaxation. In addition, these measurements could elucidate mechanisms to explain

enhanced methane hydrate formation in oils such as crude oil B described in Chapter 6. The experimental data obtained in flowing systems could be compared to multi-phase computational fluid dynamics simulations.

Surface relaxivity is an intriguing avenue of future research that could provide insight about methane hydrate formation at the interface between water drops and oil. The PFG-DE technique effectively quantifies surface relaxivity because it measures drop size and transverse relaxation simultaneously. Surface relaxivity could elucidate molecular structuring mechanisms as hydrate forms at the water/oil interface. Surface relaxivity could also contain valuable information about interfacial properties in emulsions. Continued research should focus on quantifying this parameter and understanding its relationship to interfacial properties and methane hydrate formation.

Characterizing dynamic interfacial properties is another avenue of future research. This thesis has shown the complexities that arise during emulsion formation in crude oils. The heterogeneous nature of surfactants in crude oils leads to dynamic interfacial properties that must be further quantified to gain insight about these mechanisms.

## **Appendix A: NMR Procedures**

This appendix provides the steps needed to perform CPMG, PFG-DE, and RARE measurements on the 2 MHz Maran-SS spectrometer. The software used to perform the measurements is called RiNMR. Before any measurements are performed, the sample must be centered in the most homogeneous region of the magnetic field, and the instrument must be tuned. Additional details about each technique can be found in user manuals located with the instrument. This appendix includes post-processing instructions for each technique. This appendix also contains instructions for performing hydrate experiments using the 2 MHz spectrometer.

### ***A.1 Centering the sample***

1. Place the sample in the probe.
2. Open the RiNMR software and load RARE and click the ACQUISITION tab
3. For a 4 cm sample (4 cm is the maximum height of the most homogeneous region), use  $G1=G2=500$ ,  $SI=64$ ,  $DW=40\ \mu s$ ,  $D2=1300\ \mu s$ ,  $D3=20\ \mu s$ ,  $D4=40\ \mu s$ ,  $\tau=3000\ \mu s$ ,  $NECH=1$ ,  $RD=1\ s$ ,  $RG=20$ ,  $DS=0$ ,  $NS=1$ ,  $DEAD2=20\ \mu s$ . Consult Michael Rauschhuber's report for more information about RARE parameters.<sup>65</sup>
4. type "GS1" and adjust the height of the sample until the magnitude of the Fourier transform on the screen is centered.

### ***A.2 Tuning***

1. Open the RiNMR software and click the ACQUISITION tab.
2. load WOBBLE

3. Type "GS1" and look at the minimum of the resulting curve. Center the minimum by turning the screw located at the top of the spectrometer.
4. Press "control k" to stop the sequence (each sequence must be terminated before starting the next one).
5. load FID
6. type, ".AUTOO1" using 4 scans and appropriate RD and RG (RD = 15s for water and RG = 10 for large samples to avoid clipping). This procedure will automatically define the frequency offset, 01, for the stationary magnetic field.
7. load TRAIN90 and type GS1
8. Show the current value of P90 by typing "P90" followed by "enter."
9. Use the page-up and page-down keys to form a step-wise pattern in the response.
10. load TRAIN180 and type GS1. Perform steps 8-9, but replace P90 with P180 and make the response as close to a horizontal line as possible rather than a step wise pattern.
11. type, ".DEGAUSS" followed by "enter." Do this 3 times.

### **A.3 CPMG**

1. load CPMG
2. Input the correct values for RD, RG, SI, DW, NECH, TAU, and NS.
3. type "go."
4. After the measurement is completed, save the data using the "WR" followed by "enter" command and "EX" followed by "enter."
5. The one dimensional inversion used to obtain  $T_2$  distributions was written by T.L. Chuah.<sup>104</sup> The .DAT and .PAR should be loaded into the T2RAWDAT folder which is in the same directory as the  $T_2$  inversion. Run the  $T_2$  inversion.



## **A.4 PFG-DE**

1. Calculate the parameters for the PFG-DE measurement which include the gradient spacing,  $\Delta$ , gradient duration,  $\delta$ , and list of gradient strength values, as described in Chapter 3. Use the MatLab code provided in the “parameter selection” directory. The files that require inputs are “conditcd4.m, makedatafileb5.m, and runcomesaveme.m.”
2. Create a batch file on the Maran-SS computer that contains the file name for the gradient spacing and list of gradient strength values. Directly input the gradient duration. Also include the file name of the data file that will be produced.
3. Turn on the gradient cooling bath to prevent damage to the gradient coils and probe. Set the temperature of the bath to 28°C.
4. Open the RINMR software and select the “process” tab.
5. Set the path for the gradient values by going to “tools” and “set new value.”
6. Designate where the data and parameter files should be written by typing “WR” and “EX” while in the process mode.
7. type “bat” and select the correct batch file.
8. Place the .PAR and .DAT files in the drop size\_T2 inversion folder and run the inversion.

## **A.5 RARE**

1. load RARE
2. The parameters depend on the height of the sample and the type of fluid.<sup>65</sup> For a 4 cm sample containing water, use the following parameters:  $G1=G2=500$ ,  $SI=64$ ,  $DW=40\ \mu s$ ,  $D2=1300\ \mu s$ ,  $D3=20\ \mu s$ ,  $D4=40\ \mu s$ ,  $\tau=3000\ \mu s$ ,  $NECH=1K$ ,  $RD=15\ s$ ,  $RG=20$ ,  $DS=4$ ,  $NS=64$ ,  $DEAD2=20\ \mu s$ .

3. type "GO"
4. Save the data using the WR and EX commands.
5. Put the .RiDAT file in the "data" folder of the RARE\_mult\_exp folder. Run the RARE program in MatLab.

## ***A.6 Hydrate measurements***

1. Place the emulsion in the PEEK sample chamber.
2. Use the metal rods to guide the PEEK spacers into the PEEK sleeve.
3. Tighten the bolts at the top and bottom of the pressure vessel.
4. Run the fluoroptic temperature probe down through the center of the pressure vessel.
5. Attach the saturating pump lines such that the outlet of the saturation pump is at the bottom of the pressure vessel and the inlet is at the top.
6. Secure the plastic funnels at the top and bottom of probe.
7. Use the three all-thread pieces to center sample in probe.
8. Hook up methane to the pressure vessel and turn on saturation pump.
9. Turn on gradient cooling system.
10. Hook up either the AC unit or gaseous nitrogen to the funnel on the bottom of the probe, depending on desired temperature.

## References

1. Schramm, L. L., *Emulsions, Foams, and Suspensions*. Wiley-VCH: Weinheim, 2005.
2. Chappat, M., Some applications of emulsions. *Colloids and Surfaces A: Physicochemical and Engineering Aspects* **1994**, 91, 57-77.
3. Cao, A.; Hantz, E.; Taillandier, E., Study of emulsions of pharmaceutical interest by light scattering. *Colloids and Surfaces* **1985**, 14, 217-229.
4. Peña, A.; Hirasaki, G. J., NMR Characterization of Emulsions. In *Emulsions and Emulsion Stability*, Sjoblom, J., Ed. CRC: Boca Raton, FL, 2006; pp 283-309.
5. Schramm, L. L., *Emulsions: Fundamentals and Applications in the Petroleum Industry*. American Chemical Society: 1992.
6. Sjöblom, J.; Aske, N.; Auflem, I. H.; Brandal, O.; Havre, T. E.; Saether, O.; Westvik, A.; Johnsen, E. E.; Kallevik, H., Our current understanding of water-in-crude oil emulsions. Recent characterization techniques and high pressure performance. *Advances In Colloid And Interface Science* **2003**, 100, 399-473.
7. Hemmingsen, P. V.; Li, X.; Peytavy, J. L.; Sjöblom, J., Hydrate plugging potential of original and modified crude oils. *Journal of Dispersion Science and Technology* **2007**, 28, 371-382.
8. Dalmazzone, C., The Mechanical Generation of Emulsions. *Lubrication Science* **2005**, 17, 197-237.
9. Koh, C. A.; Westacott, R. E.; Zhang, W.; Hirachand, K.; Creek, J. L.; Soper, A. K., Mechanisms of gas hydrate formation and inhibition. *Fluid Phase Equilibria* **2002**, 194-197, 143-151.
10. Sloan, E. D., *Clathrate Hydrates of Natural Gases*. 3 ed.; CRC: New York, 2008.
11. Boxall, J.; Davies, S.; Nicholas, J.; Turner, D.; Talley, L.; Koh, C.; Sloan, E. D., Hydrate blockage potential in an oil dominated system studied using a four inch flow loop. In *Sixth International Conference on Gas Hydrates*, Vancouver, British Columbia, Canada, 2008.
12. Skodvin, T., Formation of Gas Hydrates in Stationary and Flowing W/O Emulsions. In *Encyclopedic Handbook of Emulsion Technology*, Sjoblom, J., Ed. Marcel Dekker: New York, 2001; pp 695-705.

13. Turner, D.; Talley, L., Hydrate inhibition via cold flow - no chemicals or insulation. In *Sixth International Conference on Gas Hydrates*, Vancouver, British Columbia, Canada, 2008.
14. Bancroft, W. D., The Theory of Emulsification. *Journal of Physical Chemistry* **1915**, 19, 275-309.
15. Becher, P., *Emulsions: Theory and Practice*. 3 ed.; Oxford University Press: Washington, D.C., 2001.
16. Becher, P., *Encyclopedia of Emulsion Technology*. Marcel Dekker: New York, 1983; Vol. 1.
17. Walstra, P., Principles of Emulsion Formation. *Chemical Engineering Science* **1993**, 48, 333-349.
18. Walstra, P.; Smulders, P. E. A., Modern Aspects of Emulsion Science. In Binks, B., Ed. Royal Society of Chemistry: Cambridge, UK, 1998.
19. Walstra, P., Emulsion Stability. In *Encyclopedia of Emulsion Technology*, Becher, P., Ed. 1996; Vol. 4, pp 1-62.
20. Ivanov, I. B.; Dimitrov, D. S., Thin Film Drainage. In *Thin Liquid Films: Fundamentals and Applications*, Ivanov, I. B., Ed. Marcel Dekker: New York, 1988.
21. Walstra, P., Formation of Emulsions. In *Encyclopedia of Emulsion Technology*, Becher, P., Ed. 1983; Vol. 1, p 57.
22. Heusch, R., Emulsions. A9, 297.
23. Aske, N., R. Orr, J. Sjöblom, H. Kallevik, G. Oye, Interfacial Properties of Water-Crude Oil Systems Using the Oscillating Pendant Drop Correlations to Asphaltene Solubility by Near Infrared Spectroscopy. *Journal of Dispersion Science and Technology* **2004**, 25, 263-275.
24. Lucassen-Reynders, E. H., Dynamic Interfacial Properties in Emulsification. In *Encyclopedia of Emulsion Technology*, Becher, P., Ed. 1996.
25. Tempel, M. v. d. In *The Function of Stabilizers During Emulsification*, Third International Congress on Surface-Active Agents, Verlag der Universitätsdruckerei Mainz, Germany, 1960; Verlag der Universitätsdruckerei Mainz, Germany, 1960; p 573.
26. Malot, H.; Noik, C.; Dalmazzone, C. In *Experimental Investigation on Water-in-Crude Oil Emulsion Formation Through a Model Choke Valve: Droplet Break-up and Phase Inversion*, International Conference on Multiphase Flow, San Remo, Italy, 2003; San Remo, Italy, 2003.

27. Czarnecki, J.; Moran, K., On the Stabilization Mechanism of Water-in-Oil Emulsions in Petroleum Systems. *Energy and Fuels* **2005**, 19, 2074-2079.
28. Kilpatrick, P., Asphaltene Emulsions. In *Encyclopedic Handbook of Emulsion Technology*, Sjöblom, J., Ed. Marcel Dekker: New York, 2001; pp 707-730.
29. Sjöblom, J.; Hemmingsen, P. V.; Kallevik, H., The Role of Asphaltenes in Stabilizing Water-in-Crude Oil Emulsions. In *Asphaltenes, Heavy Oils, and Petroleomics*, Mullins, O. C.; Sheu, E. Y.; Hammami, A.; Marshall, A. G., Eds. Springer: New York, New York, 2007; pp 549-587.
30. Verruto, V. J.; Kilpatrick, P. K., Preferential solvent partitioning within asphaltenic aggregates dissolved in binary solvent mixtures. *Energy and Fuels* **2007**, 21, 1217-1225.
31. McMullan, R. K.; Jeffrey, G. A., Polyhedral clathrate hydrates IX Structure of ethylene oxide hydrate. *Journal of Chemical Physics* **1965**, 42, 2725-2732.
32. Mak, C. W.; McMullan, R. K., Polyhedral clathrate hydrates X structure of the double hydrate of tetrahydrofuran and hydrogen sulfide. *Journal of Chemical Physics* **1965**, 42, 2732-2737.
33. Ripmeester, J. A.; Tse, J. S.; Ratcliffe, C. I.; Powell, B. M., A new clathrate hydrate structure. *Nature* **1987**, 325, 135-136.
34. Hammerschmidt, E. G., Formation of Gas Hydrates in Natural Gas Transmission Lines. *Industrial and Engineering Chemistry* **1934**, 2, 851-855.
35. Turner, D. Clathrate Hydrate Formation in Water-in-Oil Dispersions. Colorado School of Mines, Golden, CO, 2005.
36. Bishnoi, P. R.; Dholabhai, P. D., Equilibrium conditions for hydrate formation for a ternary methane, propane, and carbon dioxide, and a natural gas mixture in the presence of electrolytes and methanol. *Fluid Phase Equilibria* **1999**, 158-160, 821-827.
37. Gao, S. Formation and Dissociation Mechanisms of Clathrate Hydrates. Rice University, Houston, TX, 2006.
38. Gao, S.; House, W.; Chapman, W. G., Detecting Gas Hydrate Behavior in Crude Oil Using NMR. *Journal of Physical Chemistry B* **2006**, 110, 6549-6552.
39. Aichele, C. P.; Chapman, W. G.; Rhyne, L. D.; Subramani, H. J.; Montesi, A.; Creek, J. L.; House, W., Nuclear Magnetic Resonance Analysis of Methane Hydrate Formation in Water-in-Oil Emulsions. *Energy and Fuels* **2009**, 23, 835-841.

40. Aichele, C. P.; Flaum, M.; Jiang, T.; Hirasaki, G. J.; Chapman, W. G., Water in Oil Emulsion Droplet Size Characterization using a Pulsed Field Gradient with Diffusion Editing (PFG-DE) NMR Technique. *Journal of Colloid and Interface Science* **2007**, 315, 607-619.
41. Peña, A. Dynamic Aspects of Emulsion Stability. Rice University, Houston, 2003.
42. Stapf, S.; Han, S.-I., *NMR Imaging in Chemical Engineering*. 2006.
43. Carr, H. Y.; Purcell, E. M., Effects of Diffusion on Free Precession in Nuclear Magnetic Resonance Experiments. *Physical Review* **1954**, 94, 630-638.
44. Meiboom, S.; Gill, D., Modified Spin-echo Method for Measuring Nuclear Relaxation Times. *Rev. Sci. Instrum.* **1958**, 29, 688-691.
45. Stejskal, E. O., J.E. Tanner, Spin Diffusion Measurements: Spin Echoes in the Presence of a Time Dependent Field Gradient. *Journal of Chemical Physics* **1965**, 42, 288-292.
46. Flaum, M. Fluid and Rock Characterization Using New NMR Diffusion-Editing Pulse Sequences and Two Dimensional Diffusivity-T2 Maps. Rice University, Houston, 2006.
47. Hürlimann, M. D.; Venkataramanan, L., Quantitative Measurement of Two Dimensional Distribution Functions of Diffusion and Relaxation in Grossly Inhomogenous Fields. *Journal of Magnetic Resonance* **2002**, 157, 31-42.
48. Venkataramanan, L.; Song, Y. Q.; Hürlimann, M. D., *IEEE Transactions on Signal Processing* **2002**, 50, 1017-1026.
49. Hennig, J.; Nauerth, A.; Friedburg, H., RARE Imaging: A Fast Imaging Method for Clinical MR. *Magnetic Resonance in Medicine* **1986**, 3, 823-833.
50. Hore, P. J., *Nuclear Magnetic Resonance*. Oxford University Press: New York, 1995.
51. Coates, G. R., Lizhi Xiao, Manfred G. Prammer, *NMR Logging: Principles and Applications*. Halliburton Energy Services: Houston, 1999.
52. Fukushima, E.; Roeder, S. B. W., *Experimental Pulse NMR: A Nuts and Bolts Approach*. Perseus: Cambridge, 1981.
53. Cowan, B., *Nuclear Magnetic Resonance and Relaxation*. Cambridge University Press: Cambridge, United Kingdom, 1997.

54. Tikhonov, A. N.; Arsenin, V. Y., *Solution of Ill-Posed Problems*. Winston & Sons: Washington, D.C., 1977.
55. Dunn, K. J.; LaTorraca, G. A.; Warner, J. L.; Bergman, D. J., On the Calculation and Interpretation of NMR Relaxation Times Distribution. In *69th Annual Technical Conference and Exhibition*, New Orleans, LA, 1994; pp 45-54.
56. Huang, C. C. Estimation of Rock Properties by NMR Relaxation Methods. Rice University, Houston, 1997.
57. Brownstein, K. R.; Tarr, C. E., Importance of Classical Diffusion in NMR Studies of Water in Biological Cells. *Physical Review A* **1978**, 19, 2446-2453.
58. Garasanin, T.; Cosgrove, T., NMR Self-diffusion studies on PDMS oil-in-water emulsion. *Langmuir* **2002**, 18, 10298-10304.
59. Murday, J. S., R.M. Cotts, Self-Diffusion Coefficient of Liquid Lithium. *Journal of Chemical Physics* **1968**, 48, 4938-4945.
60. Neuman, C. H., Spin Echo of Spins Diffusing in a Bounded Medium. *Journal of Chemical Physics* **1974**, 60, 4508-4511.
61. Packer, K. J.; Rees, C., Pulsed NMR Studies of Restricted Diffusion I. Droplet Size Distributions in Emulsions. *Journal Of Colloid And Interface Science* **1972**, 40, 206-218.
62. Casella, G.; Berger, R. L., *Statistical Inference*. Duxbury: Pacific Grove, CA, 2002.
63. Orr, C., Emulsion Droplet Size Data. In *Encyclopedia of Emulsion Technology*, Becher, P., Ed. 1983; Vol. 1, pp 369-404.
64. Callaghan, P. T., *Principles of Nuclear Magnetic Resonance Microscopy*. Oxford University Press: New York, 1991.
65. Rauschhuber, M., NMR 1-D Profiling. In Rice University: Houston, 2007.
66. Pena, A.; Hirasaki, G. J., Enhanced Characterization of Oilfield Emulsions via NMR Diffusion and Transverse Relaxation Experiments. *Advances In Colloid And Interface Science* **2003**, 105, 103-150.
67. Rosen, M. J., *Surfactants and Interfacial Phenomena*. Wiley: New York, New York, 1989.
68. Rallison, J. M., The Deformation of Small Viscous Drops and Bubbles in Shear Flows. *Annual Review of Fluid Mechanics* **1984**, 16, 45-66.

69. Stone, H. A., Dynamics of Drop Deformation and Breakup in Viscous Fluids. *Annual Review of Fluid Mechanics* **1994**, 26, 65-102.
70. Zhao, X., Drop breakup in dilute newtonian emulsions in simple shear flow: New drop breakup mechanisms. *Journal of Rheology* **2007**, 51, 367-392.
71. Guido, S.; Villone, M., Three-dimensional Shape of a Drop Under Simple Shear Flow. *Journal of Rheology* **1997**, 42, (2), 395-415.
72. Taylor, G. I., The Viscosity of a Fluid Containing Small Drops of Another Fluid. *Proceedings of the Royal Society of London* **1932**, 138, (834), 41-48.
73. Taylor, G. I., The Formation of Emulsions in Definable Fields of Flow. *Proceedings of the Royal Society of London* **1934**, 146, (858), 501-523.
74. Taylor, G. I. In *Conical Free Surfaces and Fluid Interfaces*, Proc. Int. Congr. Appl. Mech., Munich, 1964; Munich, 1964; pp 790-796.
75. Zhao, X. Drop Breakup in Dilute Newtonian Emulsions Under Steady Shear. Rice University, Houston, 2003.
76. Rumscheidt, F. D.; Mason, S. G., Particle Motions in Sheared Suspensions XII. Deformation and Burst of Fluid Drops in Shear and Hyperbolic Flow. *Journal of Colloid Science* **1961**, 16, 238-261.
77. Torza, S.; Cox, R. G.; Mason, S. G., Particle Motions in Sheared Suspensions XXVII Transient and Steady Deformation and Burst of Liquid Drops. *Journal Of Colloid And Interface Science* **1972**, 38, (2), 395-411.
78. Grace, H. P., Dispersion Phenomena in High Viscosity Immiscible Fluid Systems and Application of Static Mixers as Dispersion Devices in Such Systems. *Chemical Engineering Communications* **1982**, 14, 225-277.
79. Hinch, E. J.; Acrivos, A., Steady Long Slender Droplets in Two-Dimensional Straining Motion. *Journal of Fluid Mechanics* **1979**, 91, 401-414.
80. Barthes-Biesel, D.; Acrivos, A., Deformation and Burst of a Liquid Droplet Freely Suspended in a Linear Shear Field. *Journal of Fluid Mechanics* **1973**, 61, 1-21.
81. Hinch, E. J., A. Acrivos, Long Slender Drops in a Simple Shear Flow. *Journal of Fluid Mechanics* **1980**, 98, 305-328.
82. Buckley, J.; Creek, J.; Wang, J.; Fan, T., SARA analysis. In New Mexico Tech, 2008.



83. McLean, J. D.; Kilpatrick, P. K., Effects of Asphaltene Solvency on Stability of Water-in-Crude-Oil Emulsions. *Journal of Colloid and Interface Science* **1997**, 189, 242-253.
84. Bird, R. B.; Stewart, W. E.; Lightfoot, E. N., *Transport Phenomena*. 2nd ed.; John Wiley and Sons: New York, 2002.
85. Kataoka, K., Taylor Vortices and Instabilities in Circular Couette Flows. In *Encyclopedia of Fluid Mechanics*, Gulf Publishing Company: Houston, TX, 1986; Vol. 1.
86. Taylor, G. I., *Phil. Trans. Roy. Soc. London* **1923**, A223-289.
87. Krieger, I. M.; Dougherty, T. J., A mechanism for non-Newtonian flow in suspensions of rigid spheres. *Journal of Rheology* **1959**, 3, (1), 137-152.
88. Janssen, J. M. H. Dynamics of Liquid-Liquid Mixing. University of Technology, Eindhoven, The Netherlands, Eindhoven, 1993.
89. Angle, C. W.; Hamza, H. A.; Dabros, T., Size distributions and stability of toluene diluted heavy oil emulsions. *AIChE Journal* **2006**, 52, (3), 1257-1266.
90. Rushton, J. H.; Costich, E. W.; Everett, H. J., Power Characteristics of Mixing Impellers: Part I. *Chemical Engineering Progress* **1950**, 46, (8), 395.
91. Rushton, J. H.; Costich, E. W.; Everett, H. J., Power Characteristics of Mixing Impellers: Part II. *Chemical Engineering Progress* **1950**, 46, (9), 467.
92. Calabrese, R. V.; Chang, T. P. K.; Dang, P. T., Drop Breakup in Turbulent Stirred-Tank Contactors Part I: Effect of Dispersed-Phase Viscosity. *AIChE Journal* **1986**, 32, (4), 657-666.
93. Calabrese, R. V.; Wang, C. Y.; Bryner, N. P., Drop Breakup in Turbulent Stirred-Tank Contactors Part III: Correlations for Mean Size and Drop Size Distribution. *AIChE Journal* **1986**, 32, (4), 677-681.
94. Wang, C. Y.; Calabrese, R. V., Drop Breakup in Turbulent Stirred-Tank Contactors Part II: Relative Influence of Viscosity and Interfacial Tension. *AIChE Journal* **1986**, 32, (4), 667-676.
95. Hinze, J. O., Fundamentals of the Hydrodynamic Mechanism of Splitting in Dispersion Processes. *AIChE Journal* **1955**, 1, (3), 289-295.
96. Chen, H. T.; Middleman, S., Drop Size Distribution in Agitated Liquid-Liquid Systems. *AIChE Journal* **1967**, 13, (5), 989-995.

97. Nandi, A.; Mehra, A.; Khakhar, D. V., Suppression of coalescence in surfactant stabilized emulsions in shear flow. *Physical Review Letters* **1999**, 83, (12), 2461-2464.
98. Fouconnier, B.; Komunjer, L.; Ollivon, M.; Lesieur, P.; Keller, G.; Clausse, D., Study of CC13F hydrate formation and dissociation in W/O emulsion by differential scanning calorimetry and X-ray diffraction. *Fluid Phase Equilibria* **2006**, 250, 76-82.
99. Bernstein, M. A.; King, K. F.; Zhou, X. J., *Handbook of MRI Pulse Sequences*. Elsevier Academic Press: San Diego, CA, 2004.
100. Stern, L. A.; Kirby, S. H.; Durham, W. B., Polycrystalline methane hydrate: synthesis from superheated ice, and low temperature mechanical properties. *Energy and Fuels* **1998**, 12, 201-211.
101. Carte, A. E., The Freezing of Water Droplets. *Proc. Phys. Soc. B* **1956**, 69, (10), 1028-1037.
102. Clausse, D.; Gomez, F.; Dalmazzone, C.; Noik, C., A method for the characterization of emulsions, thermogravimetry: Application to water-in-crude oil emulsion. *Journal of Colloid and Interface Science* **2005**, 287, 694-703.
103. Kutner, M. H.; Nachtsheim, C. J.; Neter, J.; Li, W., *Applied Linear Statistical Models*. McGraw-Hill: New York, New York, 2005.
104. Chuah, T.-L. Estimation of Relaxation Time Distribution for NMR CPMG Measurements. Rice University, Houston, 1996.